Martyn P. Nash · Poul M.F. Nielsen
Adam Wittek · Karol Miller
Grand R. Joldes *Editors*

Computational Biomechanics for Medicine

Personalisation, Validation and Therapy

Springer

Computational Biomechanics for Medicine

Martyn P. Nash • Poul M.F. Nielsen • Adam Wittek
Karol Miller • Grand R. Joldes
Editors

Computational Biomechanics for Medicine

Personalisation, Validation and Therapy

Springer

Editors
Martyn P. Nash
Auckland Bioengineering Institute
University of Auckland
Auckland, New Zealand

Poul M.F. Nielsen
Auckland Bioengineering Institute
University of Auckland
Auckland, New Zealand

Adam Wittek
Intelligent Systems for Medicine Laboratory
Department of Mechanical Engineering
The University of Western Australia
Perth, WA, Australia

Karol Miller
Intelligent Systems for Medicine Laboratory
Department of Mechanical Engineering
The University of Western Australia
Perth, WA, Australia

Grand R. Joldes
Intelligent Systems for Medicine Laboratory
Department of Mechanical Engineering
The University of Western Australia
Perth, WA, Australia

ISBN 978-3-030-15922-1 ISBN 978-3-030-15923-8 (eBook)
https://doi.org/10.1007/978-3-030-15923-8

© Springer Nature Switzerland AG 2020
This work is subject to copyright. All rights are reserved by the Publisher, whether the whole or part of the material is concerned, specifically the rights of translation, reprinting, reuse of illustrations, recitation, broadcasting, reproduction on microfilms or in any other physical way, and transmission or information storage and retrieval, electronic adaptation, computer software, or by similar or dissimilar methodology now known or hereafter developed.
The use of general descriptive names, registered names, trademarks, service marks, etc. in this publication does not imply, even in the absence of a specific statement, that such names are exempt from the relevant protective laws and regulations and therefore free for general use.
The publisher, the authors, and the editors are safe to assume that the advice and information in this book are believed to be true and accurate at the date of publication. Neither the publisher nor the authors or the editors give a warranty, express or implied, with respect to the material contained herein or for any errors or omissions that may have been made. The publisher remains neutral with regard to jurisdictional claims in published maps and institutional affiliations.

This Springer imprint is published by the registered company Springer Nature Switzerland AG.
The registered company address is: Gewerbestrasse 11, 6330 Cham, Switzerland

Preface

Medical and biological sciences are experiencing a transformative era with rapid growth in the quantity and quality of biomedical data that is available in the clinical, laboratory, and community settings. Computational biomechanics offers a rational basis for amalgamating this wealth of diverse data in order to provide diagnostic, therapeutic, and physiological information to physicians, patients, and researchers that would not otherwise be available. Model-based approaches to integrate information are being used to inform a wide range of clinical and research applications, such as medical image analysis, surgical training and planning, image-guided intervention, detection and prognosis of disease, implant and prosthesis design, injury assessment and prevention, and rehabilitation biomechanics. However, there is still a great deal to learn, achieve, develop, and validate before personalised biomechanics modelling technology can be seamlessly and universally integrated across medical practice.

Since 2010, annual volumes of the *Computational Biomechanics for Medicine* book series have provided a forum for specialists in biomechanics to describe their latest results and discuss applications of their techniques to computer-integrated medicine. This tenth volume in the series comprises the recent developments in tissue biomechanics, fluid biomechanics, and associated numerical methods, from researchers throughout the world. Topics discussed include:

- pelvic floor mechanics and injury
- musculo-skeletal mechanics
- brain impact mechanics
- needle insertion
- cerebral blood flow and angiography modelling

The *Computational Biomechanics for Medicine* book series not only provides the community with a snapshot of the latest state of the art, but when patient-specific modelling and computational biomechanics have become a mainstay of personalised healthcare, this series also serves as a record of the key challenges, solutions, and developments in this field.

Martyn P. Nash
Poul M. F. Nielsen
Adam Wittek
Karol Miller
Grand R. Joldes

Contents

Biomechanical Simulation of Vaginal Childbirth: The Colors of the Pelvic Floor Muscles

Dulce A. Oliveira, Maria Elisabete T. Silva, Maria Vila Pouca, Marco P. L. Parente, Teresa Mascarenhas, and Renato M. Natal Jorge

Abstract Childbirth-related trauma is a recurrent and widespread topic due to the disorders it can trigger, such as urinary and/or anal incontinence, and pelvic organ prolapse, affecting women at various levels. Pelvic floor dysfunction often results from weakening or direct damage to the pelvic floor muscles (PFM) or connective tissue, and vaginal delivery is considered the primary risk factor. Elucidating the normal labor mechanisms and the impact of vaginal delivery in PFM can lead to the development of preventive and therapeutic strategies to minimize the most common injuries. By providing some understanding of the function of the pelvic floor during childbirth, the existing biomechanical models attempt to respond to this problem. These models have been used to estimate the mechanical changes on PFM during delivery, to analyze fetal descent, the effect of the fetal head molding, and delivery techniques that potentially contribute to facilitating labor and reducing the risk of muscle injury.

Biomechanical models of childbirth should be sufficiently well-informed and functional for personalized planning of birth and obstetric interventions. Some challenges to be addressed with a focus on customization will be discussed including the in vivo acquisition of individual-specific pelvic floor mechanical properties.

Keywords Computational biomechanics · Physics-based computational model · Vaginal delivery · Pelvic floor muscles

---

D. A. Oliveira · M. E. T. Silva · M. V. Pouca · M. P. L. Parente · R. M. Natal Jorge (✉)
INEGI, LAETA, Faculty of Engineering, University of Porto, Porto, Portugal
e-mail: rnatal@fe.up.pt

T. Mascarenhas
Department of Gynecology and Obstetrics, São João Hospital Center –EPE, Faculty of Medicine, University of Porto, Porto, Portugal

M. P. Nash et al. (eds.), *Computational Biomechanics for Medicine*,
https://doi.org/10.1007/978-3-030-15923-8_1

1 Introduction

Pregnancy and childbirth are very complex processes, and sometimes with harmful consequences for the woman and/or the newborn. During pregnancy, the pelvic floor function (sphincteric—regulating storage and evacuation of urine and stool; support and stability of the pelvic organs, and sexual) may be compromised due to the effect of hormonal changes and increased intra-abdominal pressure. In vaginal delivery, the deformations to which the pelvic floor muscles (PFM) are subjected, which may even exceed the physiological limits, can lead to muscle ruptures which in turn lead to pelvic floor disorders [1]. In fact, vaginal delivery is the most implicated epidemiological risk factor for the development of pelvic floor dysfunction (PFD). Dysfunction of the pelvic floor complex can result in a wide range of symptoms including urinary incontinence (UI), fecal incontinence (FI), and pelvic organ prolapse (POP). According to the International Urogynecological Association (IUGA)/International Continence Society (ICS) terminology, UI is the complaint of any involuntary leakage of urine, FI is the complaint of involuntary loss of feces, and POP is the descent of one or more of the anterior vaginal wall, posterior vaginal wall, the uterus (cervix) or the apex of the vagina [2].

Due to its high prevalence, PFD represents a major public health problem, considerably decreasing women's quality of life [3, 4]. The number of women affected with PFD is forecast to widen to 43.8 million in 2050, representing an increase of more than 50% compared to 2010 (Fig. 1) [3]. Consequently, it is expected that the number of women undergoing surgery for PFD correction continues to increase, with a reoperation rate of 30%, and with an increasingly shorter time interval between repeated procedures [5].

According to De Souza et al. [6], about 54% of women have physiological or normal vaginal delivery, 21% undergo an instrumental delivery, and the remaining 25% give birth by cesarean section. Vaginal delivery is a perfect time to apply preventive strategies. Avoiding damage during vaginal delivery may prevent PFD from developing. Therefore, elucidating the pregnancy mechanisms and the impact of vaginal delivery on the PFM using pelvic floor biomechanics can lead to the development of preventive and therapeutic strategies to minimize the most common injuries.

2 Mechanism of Normal Labor

Labor is defined as regular uterine contractions that lead to progressive effacement and dilation of the cervix, resulting in delivery of the fetus, amniotic fluid, placenta, and membranes via expulsion through the vagina. The evolution of the vaginal delivery is dictated by the complex interaction between three essential factors, the uterine activity (the power—triple descending gradient), the maternal pelvis (the passage), and the fetus (the passenger). Computational models have become

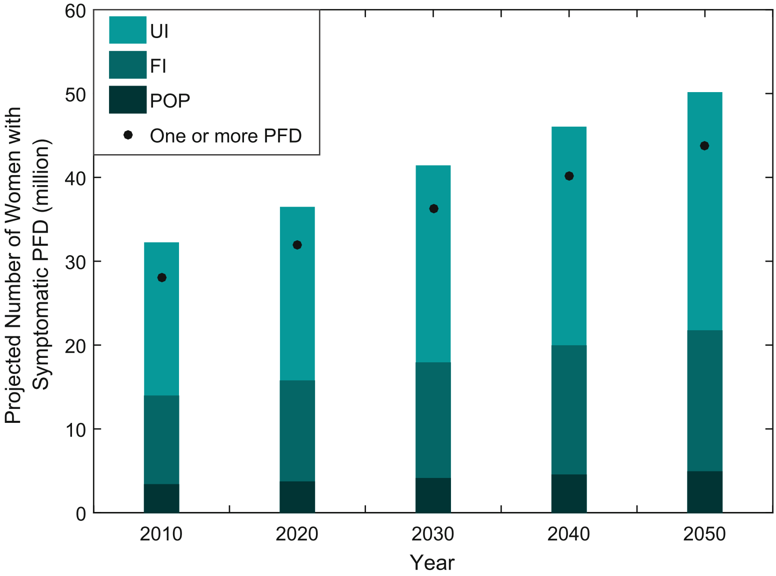

Fig. 1 Projected number of women for symptomatic PFD, 2010–2050

Fig. 2 Sagittal view of a computational model of a pregnant female

an interesting alternative to elucidate the labor mechanisms, allowing to evaluate the influence of individual features (Fig. 2). Uterine activity is characterized by the frequency, duration, and intensity of the contractions, and resting tone. The contractions start with an intensity of 1–2 kPa, increasing to 7 kPa as the cervix approaches full dilation, reaching 10–20 kPa with maternal pushing effort [7]. A successful vaginal delivery is dependent on an adequate pattern of uterine contractions.

Regarding the passage, the pelvis has three important diameters: the pelvic inlet, diagonal conjugate, and pelvic outlet (Fig. 3). The pelvic inlet has a wide transverse diameter of approximately 13 cm. It is the distance from the sacral promontory to the

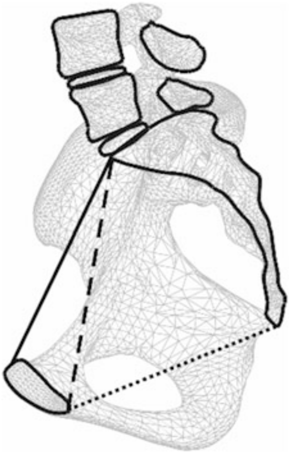

Fig. 3 Pelvic diameters: pelvic inlet—solid line, diagonal conjugate—dashed line, and pelvic outlet—dotted line

upper border of the pubic symphysis. The diagonal conjugate is the most easily and commonly assessed. It is measured from the lower border of the pubic symphysis to sacral promontory (around 11.5 cm). The pelvic outlet has a wide anterior–posterior diameter and is defined by the distance between the inferior aspect of the pubic symphysis to the coccyx. Laterally, the pelvic outlet is defined by the interspinous diameter which is the most limiting transverse diameter.

The pelvic inlet and outlet define the distance and the series of important maneuvers through which the fetus must pass while descending through the pelvis. Different pelvic shapes can restrain the position and the cardinal movements of the fetus [8]. Cardinal movements are described sequentially, although labor and delivery occur continuously. Moreover, not all fetuses follow the same pattern, as it is dependent on the presenting part. At the onset of labor, the position of the fetus in relation to the birth canal is critical to the route of delivery. The most common situation is with the fetus in a longitudinal lie with a cephalic presentation and a well-flexed attitude, described as a vertex presentation (smallest diameter presented—the suboccipitobregmatic diameter). A computational finite element model used to analyze the influence of fetal head flexion during vaginal delivery (represented by θ in the Fig. 4) suggested that a well-flexed attitude may facilitate birth, make uterine contractions more effective, and protect the pelvic floor [9]. The seven cardinal movements are then engagement, descent, flexion, internal rotation, extension, restitution and external rotation, and expulsion, and can be reproduced using computational simulation.

The fetal head is the hardest part to deliver. However, since the fetal skull is composed of sutures and fontanelles (Fig. 5), which has material properties softer than the surrounding skull bones, changes in shape are possible as the head passes through the pelvis and is subjected to constriction by external compressive forces (molding). The skull sutures and fontanelles allow the parietal and occipital bones

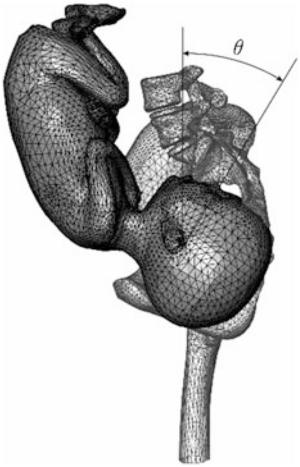

Fig. 4 Fetal head flexion determined by angle θ

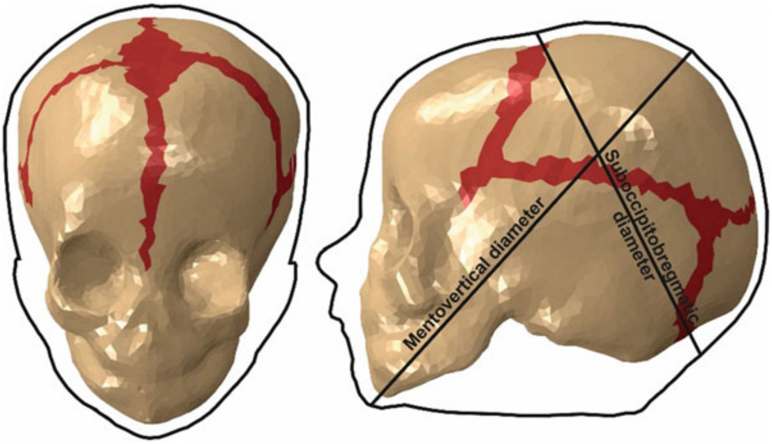

Fig. 5 Fetal skull with the sutures and fontanelles in red. Fetal head contour with two diameters represented: suboccipitobregmatic and mentovertical

to be pressed and displaced, resulting in a shortened suboccipitobregmatic diameter and an elongated mentovertical diameter, already reproduced by computational simulations [10]. The degree to which the head is capable of molding may make the difference between spontaneous delivery versus operative delivery. A malposition of the head can also lead to labor and delivery complications by obstructing fetal passage through the birth canal. A presentation with a mentovertical diameter (brow presentation) can be difficult or impossible to be delivered vaginally, because the diameter of the presenting part may be too large to safely fit through the pelvis [11].

3 Biomechanical Childbirth Simulation

Computational simulations of childbirth aim to illustrate the whole progression of labor, and to act as an adjuvant tool in the clinical setting for specific cases that may result in complicated labor, predicted by the computational model. Modeling takes into account the geometry of the structures and their mechanical properties. In biomechanics, engineering simulation tools based on the finite element method (FEM) are regularly used. However, the results of the simulations are strongly dependent on the material model chosen and the material parameters defined. Inaccurate choices lead to imprecise simulation results.

3.1 Constitutive Models

Constitutive laws are applied to reproduce the biomechanical behavior of the pelvic structures, taking into account the fundamentals of their inner structure. Most of the pelvic soft structures are assumed to be hyperelastic (describing nonlinear material behavior and large shape changes) and often incompressible materials (maintaining volume constant under pressure). Also, as some structures, for example, the pelvic striated skeletal muscles, are embedded in a connective tissue matrix, their features have to be set, as, for instance, their anisotropic and isotropic behavior, respectively. Isotropy is the property of being directionally independent, as opposed to anisotropy, which means heterogeneity in all directions.

3.1.1 Isotropic Constitutive Models: Simulating the Passive Behavior

The hyperelastic models (Neo-Hookean, Mooney–Rivlin, and Yeoh) are mainly used to simulate the passive mechanical behavior for two main reasons. Firstly, because they are simple models (with few parameters to optimize) that employ a nonlinear relationship between stress and strain to describe incompressible hyperelastic materials, and also because they seem to be able to describe the biomechanical behavior of the PFM during simulation of Valsalva maneuver and defecation and vaginal delivery [12–14].

The Neo-Hookean (Eq. 1), Mooney–Rivlin (Eq. 2), and Yeoh (Eq. 3) constitutive models are characterized by:

$$W = c_1 (I_1 - 3) \tag{1}$$

$$W = c_1 (I_1 - 3) + c_2 (I_2 - 3) \tag{2}$$

$$W = c_1 (I_1 - 3) + c_2(I_2 - 3)^2 + c_3(I_3 - 3)^3 \tag{3}$$

where W is the strain energy function and c_1, c_2, and c_3 are the material parameters to be determined and have dimensions of stress; and I_1, I_2, and I_3 are the principal strain invariants (Eq. 4) of the right Cauchy-Green tensor [12]. For the case uniaxial stretching, the principal strain invariants are represented as follows:

$$\begin{aligned} I_1 &= \lambda^2 + \tfrac{2}{\lambda} \\ I_2 &= 2\lambda + \tfrac{1}{\lambda^2} \\ I_3 &= 1 \end{aligned} \tag{4}$$

where λ is the maximum principal stretch.

In the case of uniaxial stretching, the Cauchy stress σ, a function of the invariants (Eq. 5), can be described by the following equation [12]:

$$\sigma = 2\left(\lambda^2 - \frac{1}{\lambda}\right)\left(\frac{\partial W}{\partial I_1} + \frac{1}{\lambda}\frac{\partial W}{\partial I_2}\right) \tag{5}$$

3.1.2 Anisotropic Constitutive Models: Simulating the Passive and Active Behavior of the Muscle

Additionally, a quasi-incompressible transversely isotropic hyperelastic model is used to characterize more realistically the PFM behavior—composed by a solid extracellular matrix, collagen, and muscle fibers with a preferred orientation, proposed by Martins et al. [15]. This hyperelastic model was used by other authors to simulate the PFM contraction, comparing the numerical displacements with data from dynamic sagittal MR images [16, 17], and to study the biomechanical behavior of the PFM during vaginal delivery [18, 19].

For the constitutive model used, the strain energy per unit volume of the reference configuration can be written using the following equation:

$$U = U_I\left(\overline{I}_1^C\right) + U_f\left(\overline{\lambda}_{f,\alpha}\right) + U_J(J) \tag{6}$$

where U_I is the strain energy related with deformation of the isotropic matrix embedding the muscle fibers, defined as:

$$U_I = c\left\{\exp\left[b\left(\overline{I}_1^C - 3\right)\right] - 1\right\} \tag{7}$$

and U_f is the strain energy related with each muscle fiber, considering a passive elastic part, U_{PE}, and an active part, U_{SE}, due to contraction. The function $f_{\mathrm{SE}}(\lambda^M, \alpha)$ ensures that the muscle produces no energy for values of $0.5 \geq \lambda^M \geq 1.5$, and allows to control the level of activation by the internal variable $\alpha \in [0, 1]$.

$$U_f = \overbrace{A\left\{\exp\left[a\left(\overline{\lambda}_f - 1\right)^2\right] - 1\right\}}^{U_{\mathrm{PE}}} + \overbrace{T_0^M \int_1^{\overline{\lambda}_f} f_{\mathrm{SE}}\left(\lambda^M, \alpha\right) d\lambda^M}^{U_{\mathrm{SE}}} \tag{8}$$
$$f_{\mathrm{SE}} = \alpha \begin{cases} 1 - 4\left(\lambda^M - 1\right)^2, & \text{for } 0.5 < \lambda^M < 1.5 \\ 0, & \text{otherwise} \end{cases}$$

U_J is the term of the strain energy associated with the volume change,

$$U_J = \frac{1}{D}(J - 1)^2. \tag{9}$$

In these definitions, c, b, A, a, D, and T_0^M are constants, $\overline{I}_1^C$ is the first invariant of the right Cauchy-Green strain tensor, $\mathbf{C}$, with the volume change eliminated, i.e.,

$$\overline{I}_1^C = \operatorname{tr} \overline{\mathbf{C}} = \operatorname{tr}\left(\overline{\mathbf{F}}^T \overline{\mathbf{F}}\right) = J^{-\frac{2}{3}} \operatorname{tr} \mathbf{C} \tag{10}$$

$$\overline{\lambda}_f = \sqrt{\mathbf{N}^T \overline{\mathbf{C}} \mathbf{N}} = \sqrt{\overline{\mathbf{C}} : (\mathbf{N} \otimes \mathbf{N})} \tag{11}$$

It represents the fiber stretch ratio in the direction $\mathbf{N}$ of the undeformed fiber and $\otimes$ denotes the tensor product. In Eq. (10), $\overline{\mathbf{F}}$ is the deformation gradient with the volume change eliminated and J the volume change.

Based on the constitutive equations governing the material response at a continuum level the stress tensor and the associated material tangent, $\mathbf{H}$, must be provided for numerical calculations. However, to implement the constitutive model in the software Abaqus it is mandatory to define the spatial tangent tensor, $\mathbf{h}$. In particular, the Cauchy stress tensor and the tangent stiffness matrix using the Jaumann rate of Cauchy stress are given by [20]

$$\boldsymbol{\sigma} = \frac{1}{J} \mathbf{F} \mathbf{S} \mathbf{F}^T \tag{12}$$

$$\mathbf{h}_{ijkl} = J\left(\mathbf{H}_{IJKL} + \boldsymbol{\sigma}_{ij} \delta_{kl}\right) \tag{13}$$

In Eq. (12), $\mathbf{S}$ is the second Piola-Kirchhoff stress tensor given by

$$\mathbf{S} = \frac{\partial U}{\partial \mathbf{E}} \tag{14}$$

where $\mathbf{E}$ is the Green-Lagrange strain tensor.

3.2 *In Vivo Characterization*

The female pelvic floor is a soft tissue support structure associated with different disorders. These affect the quality of life of many women and can be related with changes in the biomechanical properties of muscles, ligaments, and fascia [21]. In this sense, the biomechanical analysis of the pelvic floor tissues is important to understand different PFD. Decreased tissue elasticity often causes inability to maintain the normal position of the pelvic organs and *levator hiatus* closure, so such analysis will also improve clinical outcomes by better understanding the effect of changes in tissue elasticity. PFD may result from changes in the biomechanical properties of the supportive structures that occur from weakness or impairment of muscles or ligaments, or alterations in the stiffness of the pelvic fascia associated with the risk factors—age, hormonal changes, childbirth, among others [21].

Previous experimental in vitro studies have been addressed to evaluate biomechanical properties of the pelvic ligaments, vaginal tissue, and *levator ani* (LA) muscle [22–26]. To obtain these biomechanical properties, the tissue collected during surgeries or from female cadavers has been tested using different techniques: uniaxial [24] and biaxial tensile tests [27]. However, these collected tissues are frequently afflicted in clinical environment, and consequently, the comparison to in vivo healthy tissues is difficult [28], mainly due to their location. Hence, the computational models are a powerful tool to understand the behavior of the PFM, being used by several authors [1, 16, 18, 29].

Numerical simulations of the mechanical behavior of the PFM based on the FEM use in vitro biomechanical properties obtained from experimental studies with both normal and pathological specimens [30, 31]. Nonetheless, to achieve realistic simulation of the PFM, Silva et al. implemented an inverse finite element analysis (FEA) to obtain in vivo biomechanical properties of the PFM for a specific subject [32]. The methodology consisted in comparing dynamic MR images during Valsalva maneuver and contraction with the PFM behavior described by different constitutive models in order to define the material parameters that best mimicked the in vivo muscle behavior shown in those dynamic images [13, 32]. Silva et al. found lower elasticity for the PFM of incontinent women when compared to asymptomatic women [14]. Demographic or morphological characteristics did not explain the difference obtained, and may be associated with histological changes, due to the fact that women with incontinence usually present a significant reduction of type III collagen [33]. Lower elasticity in the PFM of incontinent women means greater displacements during Valsalva maneuver. Additionally, the mean values of the material properties related with stiffness were higher for the muscles of women with prolapse. This increase in stiffness is in line with other experimental works involving vaginal tissue, which showed that the elasticity module is significantly higher in the prolapsed tissue when compared with the normal tissue [24, 34]. The higher values of the material parameters for women with prolapse can be associated with differences in muscle morphology, regarding to the fact that women with POP presented thinner muscles. The thinner muscles in women with POP can have a histological response, decreasing the total collagen content and increasing the concentration of collagen type III [35].

However, it is important to consider some limitations and simplifications involved: (1) this sample is small; (2) the numerical models did not include the connective tissues (fascia and ligaments) and pelvic organs, which would be more realistic.

In this context, the determination of the in vivo biomechanical properties is essential to obtain customized computational models to simulate the vaginal delivery.

3.3 Vaginal Delivery Simulation

The biomechanical principles of childbirth are still unknown but it is recognized that the physiological changes that occur during pregnancy and childbirth have a detrimental effect on the structure and function of the muscles, nerves, and connective tissue that make up the pelvic floor complex. As such, the computational models arise with the intention of improving current knowledge, studying mechanical aspects during vaginal delivery (stress, tension, forces, and contact pressures), having the capability to isolate and evaluate the mechanical significance of a single feature. Hence, biomechanical studies are mainly focused on pelvic floor muscles, in order to predict obstetric trauma that will result in an increased risk of developing pelvic floor muscle dysfunction [36–38]. The computational models are meant to represent, from a mechanical point of view, the effects that the passage of a fetal head can induce on the muscles of the pelvic floor. Parente et al. found that during a vaginal delivery with the fetus in vertex position and occipito-anterior presentation, the maximal rate of stretching of the pelvic floor muscles exceeded by approximately 10% the largest noninjurious stretch ratio (Fig. 6) [37, 39]. They concluded that if the injury is caused by stretching of fibers that exceeds a maximum permissible value, during vaginal delivery there is a high risk for injury to the pelvic floor muscles [37]. It was also verified that if there is a malposition of the fetus during childbirth, namely an occipito-posterior presentation, the maximum rate of stretching of the pelvic floor muscles exceeds the limit of muscle resistance in more than 15% (Fig. 6) [40]. Yan et al. noticed that the region of the pelvic floor muscles most subjected to stresses are independent of the fetal head geometry, suggesting that the locations of potential avulsion injuries could be entirely dependent on the morphology of the maternal pelvis [8].

Oliveira et al. quantified the muscle damage during vaginal delivery with the fetus in vertex position and occipito-anterior presentation and concluded that, particularly during fetus head extension, the pelvic floor muscles are injured and that the *puborectalis* component of the *levator ani* muscle is the most prone to damage (Fig. 7) [41]. Immediately after delivery, the tissues are swollen and deformed, making it difficult to diagnose the degree of tear, leading to errors in determining the prevalence of obstetric lesions. These models thus become valuable tools in assisting

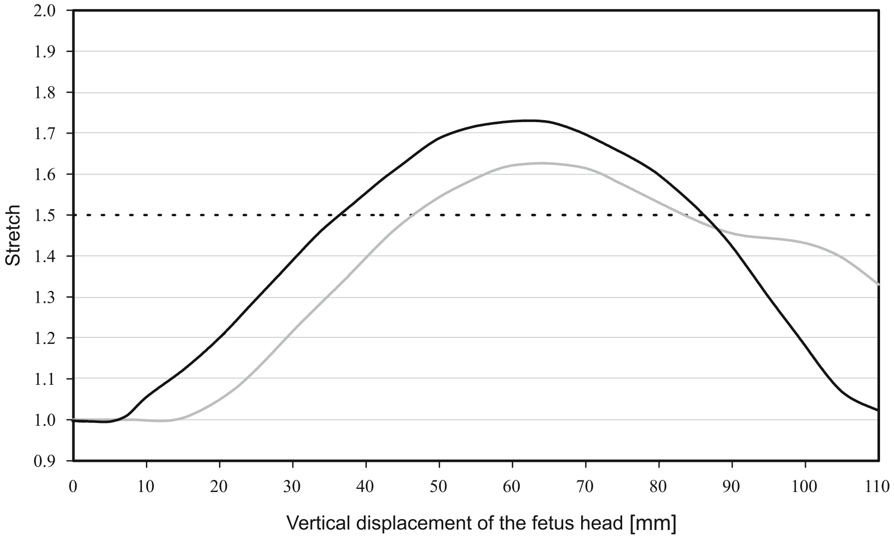

Fig. 6 Stretch values obtained during the vaginal delivery simulation with the fetus in occipito-anterior (gray line) and occipito-posterior (black line) positions. Highlighting of the stretch limit value to avoid muscle injury (dashed line)

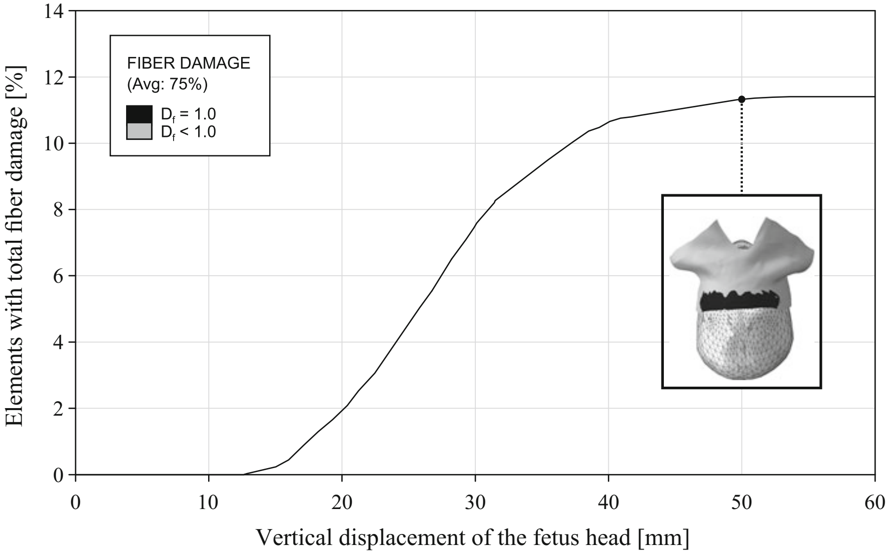

Fig. 7 Muscle damage (%) during a vaginal delivery simulation with the fetus in occipito-anterior position. Illustration of the damaged zones in the PFM, in black color, at a vertical displacement of the fetus head of 50 mm

the diagnosis of injuries. However, since the problem studied is quite complex, it is necessary to consider the limitations involved in order to properly interpret the research findings. Moreover, the impact of the computational model simplifications in the expected results should be taken into account. Yan et al. verified that the inclusion of a full pelvis provides a more complete anterior constraint to the childbirth model, resulting in noticeably variations in the fetal head motion and in higher forces required for delivery compared to a simplified model [42].

In most computational models, the viscous effects present in all biological soft tissues were disregarded, which may hinder the evaluation of the tissue behavior during labor. Vila Pouca et al. used a visco-hyperelastic constitutive model to characterize the mechanical behavior of the pelvic floor muscles to assess how the childbirth duration affects the efforts sustained by the pelvic floor [43]. They concluded that viscoelasticity increases the stiffness of the tissue, increasing strength compared to the elastic response, which justifies the higher efforts associated with precipitous labors. By including a continuum mechanics damage model, Vila Pouca et al. also found that tissue relaxation properties contribute to decrease damage levels, supporting the theory of delayed pushing applied in the second stage of labor [44].

There is a growing interest in improving computational models, taking into account, for example, the influence of the birthing positions on physiological outcomes [45]. Such computational models take pelvic joint motion into account and are able to determine pelvic kinematics under loading conditions, allowing to determine the loads applied to the female pelvis during dynamic movements that may occur during labor [46].

Such biomechanical models also allow to address the influence of common obstetric procedures, such as episiotomy. The latest Cochrane reviews do not recommend the routine use of episiotomy for vaginal delivery, irrespective of the fetal position, ensuring that the reduction in perineal/vaginal trauma is not justified by current evidence [47]. However, there is a particular group, when instrumental delivery is intended, where further research is needed. Oliveira et al. simulated vaginal deliveries with the fetus in vertex presentation and occipito-anterior position with different mediolateral episiotomies approaches, varying the length and angle of the incision [48]. According to the obtained results, they concluded that a mediolateral episiotomy has a protective effect, reducing stress on the muscles and the force necessary to delivery successfully up to 52.2% (Fig. 8). The influence of performing mediolateral episiotomies during a malposition childbirth was also addressed by Oliveira et al. [49]. They concluded that episiotomy can reduce muscle damage to values obtained during labor in normal position, making the fetal position almost irrelevant [49]. Although the results look promising for protection of PFM trauma, the model does not include the perineal body, which is the primary structure that is implicated. Therefore, further work which includes the perineal body is needed.

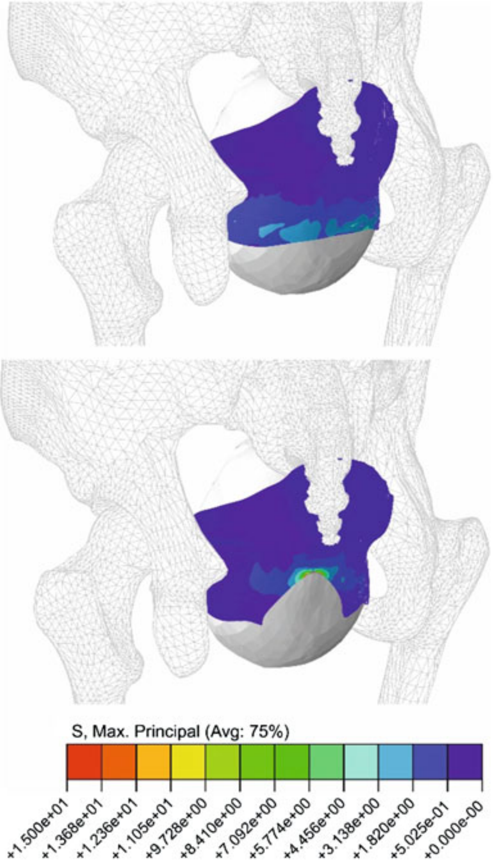

Fig. 8 Numerical simulation of the fetal descent, showing the distribution of the maximum principal stress for the PFM considering a vaginal delivery without (upper figure) and with a mediolateral episiotomy (lower figure)

4 Personalized Childbirth Models

Most of the current biomechanical models of the maternal pelvic floor and fetus system remain generic and do not provide individualized information. However, an accurate estimation of the effects of childbirth on the pelvic soft tissues implies using subject-specific biomechanical models, which will certainly improve delivery approaches. Particularly if one considers that there are significant individual differences in the anatomy of the maternal bony pelvis (size and shape), fetal head size, the mechanical properties of the pelvic floor structures, and boundary conditions. The inverse FEA will be adjusted to the ultrasound technique, replacing the magnetic resonance imaging (MRI), to obtain the in vivo biomechanical properties during vaginal delivery. Additionally, the boundary conditions will be included, according to subject-specific ultrasound technique. Patient-specific modeling has caught the attention of many relevant research groups around the world because of its potential to improve diagnosis, and optimize clinical treatment by predicting outcomes of therapies and surgical interventions. Most current medical diagnostic practices lead to rough estimates of outcomes for a particular treatment plan, and treatments and their outcomes usually find their basis in the results of clinical trials. Nonetheless, these results might not apply directly to individual patients because they are based on averages. As an alternative, patient-specific modeling can be used as a diagnostic tool to adapt treatment and optimize an individual's therapy. The patient-specific modeling workflow should involve the collection and processing of data from an individual patient and their integration into a mathematical model. The model should incorporate the mathematical representations of the patient's geometry, boundary and initial conditions, and the governing equations and parameters, with leeway for the optimization of the mechanical properties of the tissues. Regarding boundary conditions, a formulation requiring observation of tissue displacements, compliance boundary conditions, will ensure that these are individual-specific [50]. Data collected from the patient can be used for model validation; however, it should be distinct to data used for model development.

Biomechanical models in general, and of childbirth in particular, will become sufficiently well-informed and functional to enable personalized planning of surgical interventions, mainly due to the advent of clinical imaging modalities, coupled with the biostatistics, data analytics, and physics-based computational models.

5 Conclusions

As has been brought to mind throughout this chapter, the simulation of vaginal deliveries is a huge challenge. Mainly because it focuses on a region whose biomechanical research is in its infancy. There are still many issues to investigate, and many unanswered questions. Due to the advances in the field of medical imaging and in the physics-based computational models, it is expected that great advances will be made in the field of pelvic floor biomechanics. In the future, therefore, biomechanical models of childbirth will be sufficiently well-informed and functional for the personalized planning of childbirth, still serving as educational tools for physicians. The evaluation of the risk for childbirth-related pelvic floor trauma is one of the main objectives of simulating vaginal childbirth, by identifying the relevant processes that are involved in structural failure, such as the stress–strain values in the insertion points of the rectal area of the *levator ani*, and in the pubic symphysis. Obstetric techniques could be improved if they are informed by biomechanical models and simulations demonstrating the effect of certain approaches on pelvic floor biomechanics. Computational models have already shown that rupture of muscle fibers leading to macroscopic trauma of the *levator ani* can be overcome by mediolateral episiotomy, which seems to reduce the amount of stress in the PFM.

Acknowledgments The authors gratefully acknowledge the support from the Portuguese Foundation of Science under grants IF/00159/2014, and the funding of project 030062 SIM4SafeBirth—A biomechanical approach to improve childbirth outcomes and NORTE-01-0145-FEDER-000022 SciTech—Science and Technology for Competitive and Sustainable Industries, cofinanced by Norte's Regional Operational Programme (NORTE2020), through European Regional Development Fund (ERDF).

References

1. Friedman S, Blomquist J, Nugent J et al (2012) Pelvic muscle strength after childbirth. Obstet Gynecol 120:1021–1028. https://doi.org/10.1097/AOG.0b013e318265de39
2. Haylen BT, de Ridder D, Freeman RM et al (2010) An international urogynecological association (IUGA)/international continence society (ICS) joint report on the terminology for female pelvic floor dysfunction. Neurourol Urodyn 29:4–20. https://doi.org/10.1002/nau.20798
3. Wu JM, Kawasaki A, Hundley AF et al (2011) Predicting the number of women who will undergo incontinence and prolapse surgery, 2010 to 2050. Am J Obstet Gynecol 205:1–5. https://doi.org/10.1016/j.ajog.2011.03.046
4. Kiyosaki K, Ackerman L, Histed S et al (2012) Patient understanding of pelvic floor disorders: what women want to know. Female Pelvic Med Reconstr Surg 18:137–142. https://doi.org/10.1097/SPV.0b013e318254f09c. Patient
5. Wu MP, Wu CJ, Weng SF (2015) The choice of reoperation after primary surgeries for uterine prolapse: a nationwide study. Gynecol Minim Invasive Ther 4:120–125. https://doi.org/10.1016/j.gmit.2015.02.002
6. De Souza A, Dwyer P, Charity M et al (2015) The effects of mode delivery on postpartum sexual function: a prospective study. BJOG Int J Obstet Gynaecol 122:1410–1418. https://doi.org/10.1111/1471-0528.13331
7. Rempen A, Kraus M (1991) Pressures on the fetal head during normal labor. J Perinat Med 19:199–206. https://doi.org/10.1515/jpme.1991.19.3.199
8. Yan X, Kruger J, Nielsen P, Nash M (2015) Effects of fetal head shape variation on the second stage of labour. J Biomech 48(9):1593–1599. https://doi.org/10.1016/j.jbiomech.2015.02.0629
9. Parente MP, Natal Jorge RM, Mascarenhas T et al (2010) Computational modeling approach to study the effects of fetal head flexion during vaginal delivery. Am J Obstet Gynecol 203:217.e1–217.e6. https://doi.org/10.1016/j.ajog.2010.03.038
10. Silva MET, Oliveira D, Roza TH et al (2015) Study on the influence of the fetus head molding on the biomechanical behavior of the pelvic floor muscles, during vaginal delivery. J Biomech 48(9):1600–1605. https://doi.org/10.1016/j.jbiomech.2015.02.032
11. Cunningham F, Leveno K, Bloom S et al (2018) Williams obstetrics, 25th edn. McGraw-Hill Education/Medical, Pennsylvania
12. Noakes KF, Pullan AJ, Bissett IP, Cheng LK (2008) Subject specific finite elasticity simulations of the pelvic floor. J Biomech 41:3060–3065. https://doi.org/10.1016/j.jbiomech.2008.06.037
13. Silva MET, Parente MPL, Brandão S et al (2018) Characterization of the passive and active material parameters of the pubovisceralis muscle using an inverse numerical method. J Biomech 71:100–110. https://doi.org/10.1016/j.jbiomech.2018.01.033
14. Silva MET, Brandão S, Parente MPL et al (2017) Biomechanical properties of the pelvic floor muscles of continent and incontinent women using an inverse finite element analysis. Comput Methods Biomech Biomed Engin 5842:1–11. https://doi.org/10.1080/10255842.2017.130454215
15. Martins JAC, Pires EB, Salvado R, Dinis PB (1998) A numerical model of passive and active behavior of skeletal muscles. Comput Methods Appl Mech Eng 151:419–433. https://doi.org/10.1016/S0045-7825(97)00162-X
16. Roza TH, Brandão S, Oliveira D et al (2015) Football practice and urinary incontinence: relation between morphology, function and biomechanics. J Biomech 48:1587–1592. https://doi.org/10.1016/j.jbiomech.2015.03.013

17. Saleme CS, Parente MPL, Natal Jorge RM et al (2011) An approach on determining the displacements of the pelvic floor during voluntary contraction using numerical simulation and MRI. Comput Methods Biomech Biomed Engin 14:365–370. https://doi.org/10.1080/10255842.2010.482045
18. Parente MP, Natal Jorge R, Mascarenhas T et al (2009) The influence of the material properties on the biomechanical behavior of the pelvic floor muscles during vaginal delivery. J Biomech 42:1301–1306. https://doi.org/10.1016/j.jbiomech.2009.03.011
19. Parente MP, Natal Jorge R, Mascarenhas T, Silva-Filho A (2010) The influence of pelvic muscle activation during vaginal delivery. Obstet Gynecol 115:804–808. https://doi.org/10.1097/AOG.0b013e3181d534cd
20. Crisfield M (2001) Non-linear finite element analysis of solids and structures, volume 2 - advanced topics. Wiley, London
21. Abramowitch SD, Feola A, Jallah Z, Moalli PA (2009) Tissue mechanics, animal models, and pelvic organ prolapse: a review. Eur J Obstet Gynecol Reprod Biol 144:S146–S158. https://doi.org/10.1016/j.ejogrb.2009.02.022
22. Cosson M, Lambaudie E, Boukerrou M et al (2004) A biomechanical study of the strength of vaginal tissues: results on 16 post-menopausal patients presenting with genital prolapse. Eur J Obstet Gynecol Reprod Biol 112:201–205. https://doi.org/10.1016/S0301-2115(03)00333-6
23. Cosson M, Boukerrou M, Lacaze S et al (2003) A study of pelvic ligament strength. Eur J Obstet Gynecol Reprod Biol 109:80–87. https://doi.org/10.1016/S0301-2115(02)00487-6
24. Lei L, Song Y, Chen R (2007) Biomechanical properties of prolapsed vaginal tissue in pre- and postmenopausal women. Int Urogynecol J Pelvic Floor Dysfunct 18:603–607. https://doi.org/10.1007/s00192-006-0214-7
25. Rubod C, Boukerrou M, Brieu M et al (2008) Biomechanical properties of vaginal tissue: preliminary results. Int Urogynecol J Pelvic Floor Dysfunct 19:811–816
26. Martins PAL (2010) Experimental and numerical studies of soft biological tissues. PhD. Thesis. Faculty of Engineering, University of Porto, Porto
27. Janda S (2006) Biomechanics of the pelvic floor musculature. PhD. Thesis. Technische Universiteit Delft, Delft
28. Baah-Dwomoh A, McGuire J, Tan T, De Vita R (2016) Mechanical properties of female reproductive organs and supporting connective tissues: a review of the current state of knowledge. Appl Mech Rev 68:060801. https://doi.org/10.1115/1.4034442
29. Brandão FS, Parente MP, Rocha PA et al (2016) Modeling the contraction of the pelvic floor muscles. Comput Methods Biomech Biomed Engin 19:347–356. https://doi.org/10.1080/10255842.2015.1028031
30. Rivaux G, Rubod C, Dedet B et al (2013) Comparative analysis of pelvic ligaments: a biomechanics study. Int Urogynecol J 24:135–139. https://doi.org/10.1007/s00192-012-1861-5
31. Martins P, Silva-Filho AL, Fonseca AMRM et al (2013) Strength of round and uterosacral ligaments: a biomechanical study. Arch Gynecol Obstet 287:313–318. https://doi.org/10.1007/s00404-012-2564-3
32. Silva MET, Brandao S, Parente MP et al (2016) Establishing the biomechanical properties of the pelvic soft tissues through an inverse finite element analysis using magnetic resonance imaging. Proc Inst Mech Eng Part H J Eng Med 230:298–309. https://doi.org/10.1177/0954411916630571
33. Patel PD, Amrute KV, Badlani GH (2007) Pelvic organ prolapse and stress urinary incontinence: a review of etiological factors. Indian J Urol 23:135–141. https://doi.org/10.4103/0970-1591.32064
34. Jean-Charles C, Rubod C, Brieu M et al (2010) Biomechanical properties of prolapsed or non-prolapsed vaginal tissue: impact on genital prolapse surgery. Int Urogynecol J 21:1535–1538. https://doi.org/10.1007/s00192-010-1208-z
35. Kerkhof MH, Hendriks L, Brölmann H a M (2009) Changes in connective tissue in patients with pelvic organ prolapse–a review of the current literature. Int Urogynecol J Pelvic Floor Dysfunct 20:461–474. https://doi.org/10.1007/s00192-008-0737-1

36. Ashton-Miller JA, Delancey JO (2009) On the biomechanics of vaginal birth and common sequelae. Annu Rev Biomed Eng 11:163–176. https://doi.org/10.1146/annurev-bioeng-061008-12482337
37. Parente MP, Natal Jorge RM, Mascarenhas T et al (2008) Deformation of the pelvic floor muscles during a vaginal delivery. Int Urogynecol J Pelvic Floor Dysfunct 19:65–71. https://doi.org/10.1007/s00192-007-0388-7
38. Li X, Kruger J, Chung J, Nash M, Nielsen P (2008) Modelling the pelvic floor for investigating difficulties in childbirth. In: SPIE (Medical Imaging), vol 6916, p 69160V
39. Brooks S, Zerba E, Faulkner J (1995) Injury to muscle fibres after single stretches of passive and maximally stimulated muscles in mice. J Physiol 488:459–469
40. Parente MP, Natal Jorge RM, Mascarenhas T et al (2009) The influence of an occipito-posterior malposition on the biomechanical behavior of the pelvic floor. Eur J Obstet Gynecol Reprod Biol 144S:S166–S169. https://doi.org/10.1016/j.ejogrb.2009.02.033
41. Oliveira D, Parente M, Calvo B, Mascarenhas T, Natal Jorge R (2016) Numerical simulation of the damage evolution in the pelvic floor muscles during childbirth. J Biomech 49(4):594–601. https://doi.org/10.1016/j.jbiomech.2016.01.014
42. Yan X, Kruger J, Li X, Nash M, Nielsen P (2013) Modelling effect of bony pelvis on childbirth mechanics. Neurourol Urodyn 32(6):531–532
43. Vila Pouca M, Ferreira J, Oliveira D, Parente M, Natal Jorge R (2018) Viscous effects in pelvic floor muscles during childbirth: a numerical study. Int J Numer Methods Biomed Eng 34(3):e2927. https://doi.org/10.1002/cnm.2927
44. Vila Pouca M, Ferreira J, Oliveira D, Parente M, Mascarenhas T, Natal Jorge R (2018) On the effect of labour durations using an anisotropic visco-hyperelastic-damage approach to simulate vaginal deliveries. J Mech Behav Biomed Mater 88:120–126. https://doi.org/10.1016/j.jmbbm.2018.08.011
45. Hemmerich A, Diesbourg T, Dumas G (2018) Development and validation of a computational model for understanding the effects of an upright birthing position on the female pelvis. J Biomech 77:99–106. https://doi.org/10.1016/j.jbiomech.2018.06.013
46. Hemmerich A, Diesbourg T, Dumas G (2018) Determining loads acting on the pelvis in upright and recumbent birthing positions: a case study. Clin Biomech 57:10–18. https://doi.org/10.1016/j.clinbiomech.2018.05.011
47. Jiang H, Qian X, Carroli G, Garner P (2017) Selective versus routine use of episiotomy for vaginal birth. Cochrane Database Syst Rev (2):CD000081. https://doi.org/10.1002/14651858.CD000081.pub3
48. Oliveira D, Parente M, Calvo B, Mascarenhas T, Natal Jorge R (2016) A biomechanical analysis on the impact of episiotomy during childbirth. Biomech Model Mechanobiol 15(6):1523–1534. https://doi.org/10.1007/s10237-016-0781-6
49. Oliveira D, Parente M, Calvo B, Mascarenhas T, Natal Jorge R (2017) The management of episiotomy technique and its effect on pelvic floor muscles during a malposition childbirth. Comput Methods Biomech Biomed Engin 20(11):1249–1259. https://doi.org/10.1080/10255842.2017.1349762
50. Ozkan E, Goksel O (2015) Compliance boundary conditions for simulating deformations in a limited target region. In: 2015 37th Annual International Conference of the IEEE Engineering in Medicine and Biology Society (EMBC), pp 929–932. https://doi.org/10.1109/EMBC.2015.7318515

Patient-Specific Modeling of Pelvic System from MRI for Numerical Simulation: Validation Using a Physical Model

Zhifan Jiang, Olivier Mayeur, Laurent Patrouix, Delphine Cirette, Jean-François Witz, Julien Dumont, and Mathias Brieu

Abstract Numerical simulation is useful to help understand the behavior of pelvic system, and eventually to assist the diagnostic and surgery. Patient-specific simulation is expected to optimize the treatment of patients. Despite the requirement of mechanical properties and loading, patient-specific simulation requires first 3D geometry adapted to patient. Manual 3D reconstruction of the patient-specific anatomy is time-consuming and introduces uncertainties. In this paper, we propose an efficient computer-assisted approach to modeling 3D geometries well suited to MRI data. A well-controlled physical model is also proposed, and manufactured, to estimate uncertainties of the presented method.

Keywords 3D geometric modeling · Physical model · Pelvic system · Magnetic resonance imaging

1 Introduction

Female pelvic floor disorders are of critical importance, especially to aged women. For example, more than 60% of women over the age of 60 are affected by genital prolapse [1, 2]. The study of physiology and pathology is directly relevant to understand the pelvic mobility [3, 4]. It has been a challenging issue to find

---

Z. Jiang (✉) · D. Cirette
Univ. Lille, CNRS, Centrale Lille, FRE 2016 - LaMcube - Laboratoire de mécanique multiphysique multiéchelle, Lille, France

SATT Nord, Lille, France

O. Mayeur · L. Patrouix · J.-F. Witz · M. Brieu
Univ. Lille, CNRS, Centrale Lille, FRE 2016 - LaMcube - Laboratoire de mécanique multiphysique multiéchelle, Lille, France

J. Dumont
Neuroradiology Department, Univ. Lille, Inserm, CHU Lille, U1171 - Degenerative and Vascular Cognitive Disorders, Lille, France

M. P. Nash et al. (eds.), *Computational Biomechanics for Medicine*,
https://doi.org/10.1007/978-3-030-15923-8_2

appropriate diagnoses and cures for these pathologies. Currently, in the clinical routines, the diagnoses through MRI (magnetic resonance image) observations rely on physician-dependent interpretation and lead to a scientific challenge to develop techniques for the computer-assisted diagnoses.

During the past decade, the biomedical and computer science communities have been working intensively on the use of numerical simulation to improve patient-specific diagnoses and treatments. In this context, patient-specific simulation requires a 3D geometrical model, representing appropriately the structures observed in MRI and meeting the conditions of simulation. The geometrical modeling is a key work to purpose adapted simulation with finite element method because FE results are strongly conditioned by the geometries [5]. Due to the inter-individual variability and complexity of the anatomy, the reconstruction of a biofidelic geometry, compatible with FE analysis, is a time-consuming job for each patient. This method is not suitable for medical applications in a clinical routine. Our objective is to propose a method to help generate efficiently a consistent 3D geometric model, readily usable for simulation.

The classic way to generate a patient-specific geometric model is first to separate the target organs from image data (segmentation). Then the algorithm, well known as Marching cubes [6, 7] allows to generate iso-surfaces from the separated volume. A multitude of techniques has been developed to optimize the segmentation, from region growing, mathematical morphology, to probabilistic models [8]. However, a parametric CAD (computer-aided design) model will be a better support for adaptive remeshing and defining a simulation problem. Thus, these voxel-based approaches require a step of surfaces reconstruction. They are not suitable to patient-specific simulation due to the necessary post-processing.

There exist other techniques classified in deformable model approach. The idea is to match a well-defined geometry to image data by optimizing its related parameters. Such idea was firstly introduced in [9], an explicit parametric model was deformed by “forces” based on image gray level. This method was later improved by many researches to reduce artifacts, due to bad initialization and noise in images [10–11]. Recently, the virtual image correlation technique has been proposed to fit adaptive and flexible 2D models in images [12–15]. Thus, the final model is smooth and does not depend on image resolution.

The model-to-image fitting approach is consistent with our objectives. However, the pelvic system represents a complex 3D model with multiple structures and surfaces. Moreover, the images in our possession respect clinical protocols, which contain generally unwanted effects for automatic detection algorithms. Instead of a fully automatic method, a well-designed method that can be controlled by user is more feasible in this situation. For example, existing works have introduced a method to create thick surfaces of pelvic organs, based on pre-segmentations [16].

In this paper, we would like to introduce an integrated approach of geometrical modeling from image data. This work focuses on the following major contributions. Firstly, an efficient reconstruction of 3D geometry from MRI that is suitable for simulation. For this purpose, a well-defined generic CAD model is deformed to fit patient-specific MR images. Secondly, it has been a common issue that patient-specific modeling has many uncontrollable uncertainties due to image information and processing. To deal with this issue, we create a physical model of pelvic system with MRI compatible materials. This completely controllable device will be used to validate the methodology and further studies based on numerical simulation.

2 Materials and Methods

2.1 Initial Generic CAD Model

The first step of our study is to generate a 3D model of the pelvic cavity using CAD tools. The anatomical information is obtained from different sources such as anatomical charts, MRI data, cadaver, and previous works [5, 17, 18]. MRI examinations are performed on several patients presenting a normal gynecologic function without noticeable medical history (institutional ethical approval CEROG OBS 2012-05-01 R1). All the anatomical structures were reconstructed manually by image processing and segmentation techniques under 3D Slicer software [19]. The segmentation was carried out by radiologists and physicians specialized in gynecology and obstetrics, whose skills allow a better delimitation of anatomical structures. In order to obtain an accurate geometry of sustainable structures and to overcome the difficulty in observing any of them on MR images, a 3D laser scanner was also used on a post-mortem human subject (PMHS) to acquire the connective tissues: fascia and ligaments. The step-by-step dissection of the pelvic cavity allows us to identify with a better resolution than MRI the geometry of the muscles (levator ani muscle) and ligaments (cardinal, paravaginal, and utero-sacral). All the sources of data (3D scanner and MRI-based reconstruction) enabled to generate an initial generic and representative 3D model, by taking into account the principal structures of the pelvis in the physiological condition.

As the models retrieved from MRI and 3D scanner are represented by a cloud of points and triangular meshes, they are then converted to CAD representation, which consists in a geometrical definition using parametric continuous surfaces (Fig. 1a). The CAD representation enables a better description of the geometry, by removing the imperfections caused by the reconstruction, and makes the geometry usable for 3D printing or other numerical analyses such as FE simulation. A method is developed to merge the different sources to create an anatomical description of the pelvis. Each part has been fused to obtain the best resolution and to establish a generic 3D anatomical model. The geometry of organs is represented by the average geometry of four patients. The pelvic bones are the most complex part to model with CAD software. We used the reconstruction of a single patient to simplify this work. The data of this patient are selected because the morphological dimensions seem ordinary. The vulva and the pelvic floor are obtained directly from the 3D scanner acquisition. These geometries were merged in the same reference system to define our model. The operations were carried out using CATIA software (Dassault Systèmes).

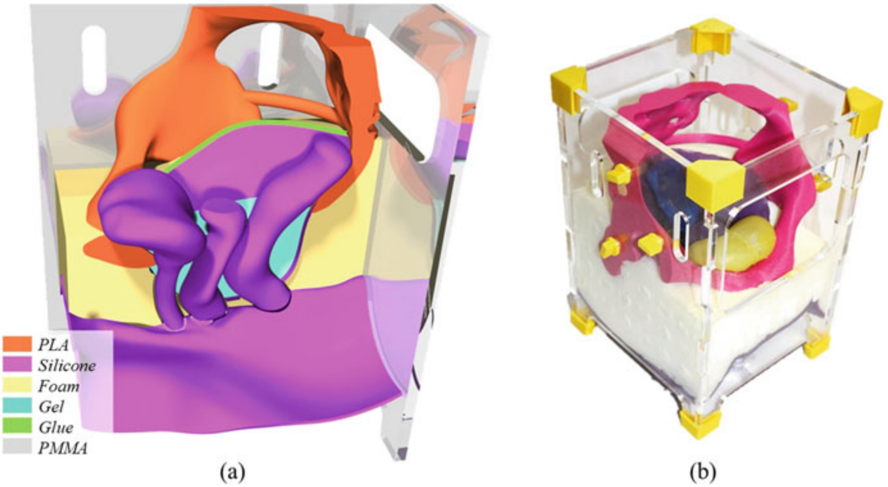

Fig. 1 (**a**) Initial generic CAD model, illustrated with a mapping of the different constitutive material, (**b**) Illustration of the physical model

2.2 *Physical Model*

The initial generic CAD model was used then to develop the physical model. At this stage, it is a surface model without thickness. To make it physical, we considered constant thicknesses of the organs, in agreement with the literature and the results of dissections [20, 21]. A particular attention was paid to the definition of the organs, so that they represent a real-life geometry.

In order to create the physical mannequin of the pelvic system, we used rapid prototyping techniques. We chose to use casting process of various silicone rubbers. Rapid prototyping techniques with a 3D printer (Zortrax M200®) were used to create the molds. The main constraint that we imposed was to create a compatible device (no ferromagnetic materials) with medical imaging techniques and observable on the MR images (Fig. 1b). We considered the bone structures as rigid parts that can be printed directly in 3D with ABS (acrylonitrile butadiene styrene) material. Since the organs (bladder, rectum, and vagina) are thin and hollow parts, we used cores to manufacture the cavity. To achieve complex geometries, some of these cores employ water-soluble support structures to facilitate the demolding. The most illustrative case is the bladder cavity where the extraction hole of the core is the urethra, too thin to allow optimum demolding.

However, an error between the physical model and the initial CAD one is induced during manufacture. In order to quantify the error and validate our process, we perform 3D scans on molds and all the silicone parts. The scans allow us to perform a deviation analysis by evaluating the minimum distance between each scanned point and the CAD model. Almost 500 points were evaluated for the smaller parts (cores, organs), and 5000 for the others (molds, vulva, pelvic floor). The observed results revealed an average deviation of 0.19 mm on all molds, muscles, and organs, scanned using the 3D laser. This deviation is small with regard to the manufactured volume under this protocol. It is partially due to the precision of the 3D scanner device (about 0.1 mm). The main deviation is due to the 3D printer with a precision of 0.2 mm. We decided to consider this error as negligible with regard to the accuracy of the MRI and the operator-dependent operations.

2.3 Geometry Reconstruction from Image Data

As mentioned in Introduction, the geometry reconstruction is a critical step to provide 3D models specific to patient, which should be consistent with the anatomy of organs or structures observable in image data and be readily usable for numerical simulation. The solution to deal with these issues consists in deforming the initial generic CAD model to find the best correlation with image data. The deformed geometry remains a well-defined CAD model. Hence, the post-processing, such as meshing, will be fully automatic and the quality of geometry will be ensured.

The geometrical morphing relies on several characteristic points on the images, corresponding to the degrees of freedom, which are manually selected by a user. At this stage, the technique can be considered as a computer-assisted method, based on well parameterized geometric models. The following schema (Fig. 2) recapitulates the main parts of this work, which will be presented in the next sections.

Firstly, the aforementioned physical model is observed with MRI. This step is carried out by the same MRI technique as the protocol conventionally used during

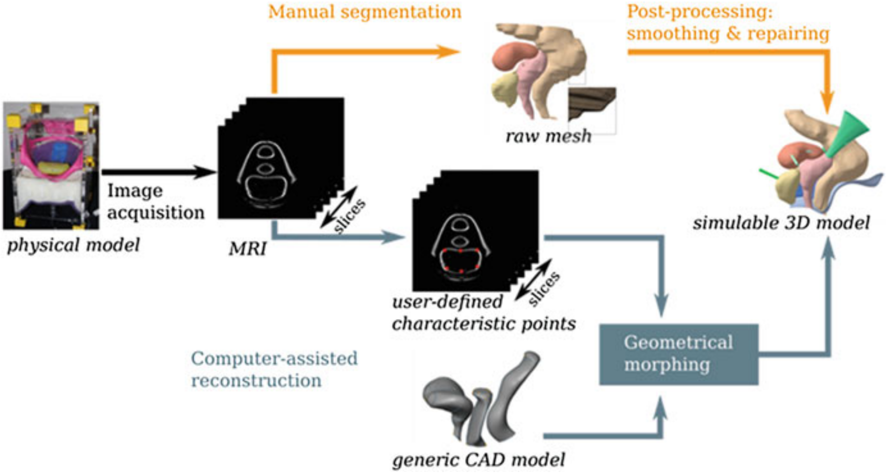

Fig. 2 Description of the main parts of geometry reconstruction from image data (manual reconstruction in orange and computer-assisted reconstruction in blue)

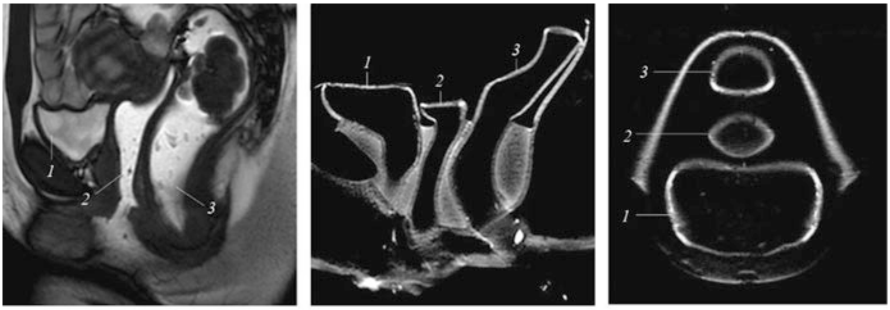

(a) (b) (c)

Fig. 3 Static MRI with 1. Bladder, 2. vagina and 3. rectum—(**a**) MRI of a second patient on sagittal plane, (**b**) MRI of the physical model on sagittal plane, (**c**) MRI of the physical model on axial plane

clinical examination: 3-Tesla MRI through 3 sequences of 2D images on the axial, coronal, and sagittal planes. This approach leads to constraints on the accuracy of the pixel size (pixel size at 0.7 mm and 3.5 mm between slices), but it was chosen deliberately to ensure the clinical adequacy. This protocol provides information comparable to MRI on real patients (Fig. 3).

As shown in Fig. 2, on these data, we applied the geometry reconstruction with two different procedures:

- *Manual reconstruction*: Geometry is generated from a manual segmentation, which is performed by surgeons in the same way as the anatomical model generation. The results are obtained using 3D Slicer software [19] and correspond to a raw triangular mesh. The analysis will be made with a comparison between points and initial CAD model.
- *Computer-assisted reconstruction*: The second approach, based on morphing algorithm of a generic CAD model, is then proposed. Using a generic CAD model to reconstruct the specific geometry allows us to have directly a simulable CAD model. A comparison will also be performed between two CAD models, the initial and deformed ones.

2.4 Reduced CAD Model and Geometrical Morphing

Mathematically, the generic CAD model is defined by using multi-patch NURBS surfaces [22]. Each patch is defined by a bidirectional net of control points in 3D space: $\{p_{i,j} \vee (i,j) \in \{0, \ldots, n\} \times \{0, \ldots, m\}\}$. Thus, in its parametric form, the coordinates of a point on the surface are given by an explicit function of parameters (u, v):

$$S\left(u,v\right)=\sum_{i=0}^{n}\sum_{j=0}^{m}N_{i,j}\left(u,v\right)p_{i,j},\forall\left(u,v\right)\in\left[\min,\max\right]^{2},$$

where $N_{i,j}$ are rational B − spline basis functions and [min , max] is the range of parameter values (more details can be found in [22]). Thus, by combining multiplepatches, we can obtain the boundary of a solid, closed or not. In our case, it is the bladder, vagina, and rectum.

Among the factors in the above equation, it is a natural and direct way to modify the shape by moving the associated control points, i.e., deforming the control net. CAD modelers have different implementation of NURBS, but they use commonly a considerable number of control points, for example, the vagina in our generic model (created using CATIA) requires several hundred control points for a single patch and about 3000 control points for the whole surface. Hence, it is not evident to obtain a suitable morphing by positioning directly control points. Moreover, the continuity between patches should also be ensured. To circumvent the complexity of the surface geometry, other degrees of freedom in a reduced space need to be considered.

Initially being a mathematical approximation and smoothing tool [23, 24], the RBF (radial basis functions) technique has been widely used in problems concerning shape deformation. For example, it is used to deform mesh [25] or to optimize the computation of deformation subjected to physical law [26]. The idea is to create a mapping $M : x \in R^3 \rightarrow x' \in R^3$, to describe the shape deformation, which is corresponding to an interpolation based on a certain number of characteristic points $\{c_k \in R^3\}$. The interpolation is computed using a kernel function $\varphi : R \rightarrow R$.

Generally, to obtain a smooth shape deformation, the thin plate spline is used:

$$\varphi(r)=r^2\ln(r).$$

(In [27], a study on the choices of RBF kernel function was discussed.) By grouping all these elements, the mapping is given by the following formula:

$$M(x)=\sum_{k=0}^{N_c}w_k\varphi\left(\|x-c_k\|\right),$$

where $\left\{w_k \in R^3\right\}$ are the weights associated with the characteristic points.The variables w in the mapping can be computed by imposing the constraints : $M\left(c_k\right)=c'_k\forall k=0,\ldots,N_c$, where $\left\{c'_k\right\}$ are the deformed positions of characteristic points.

In our application, a geometric model has much fewer characteristic points than control points, and they can be placed freely (not necessarily on a regular grid or on a convex hull). Thanks to the low number and the flexibility, the displacements of these points (their deformed positions) are defined by user, who selects points on image data. The computation of mapping M determines the deformed position of control net $\{p_{i,j}\}$, and the latter gives finally the deformation of the surface.

Moreover, new characteristic points can be added by user during the morphing. For all these reasons, the RBF technique is suitable for a seamless consistent geometry reconstruction.

3 Results

3.1 Comparison Between Manual Procedure and Initial CAD Model

We analyzed the deviation between manual MRI reconstructions (MRIm) of our mannequin and the initial CAD model (Table 1). MRI geometry is compared with reconstruction of the internal and external surfaces. The deviation analysis shows significant deviations about 1.34 mm (STD 1 mm) when we take into account the three organs. The deviation was evaluated through 4000 points, uniformly distributed on the two geometries (Fig. 4).

Table 1 Comparison of deviation between manual and semi-auto REC

	External surface				Internal surface			
	CAD vs MRIm		CAD vs MRIca		CAD vs MRIm		CAD vs MRIca	
	Mean	STD	Mean	STD	Mean	STD	Mean	STD
Vagina	1.02	0.734	–	–	1.23	1.09	0.97	0.78
Bladder	1.45	1.01	–	–	1.30	0.91	1.13	0.77
Rectum	1.43	1.12	–	–	0.98	0.89	0.86	0.65
Three organs	1.34	1.02	–	–	1.18	0.95	0.99	0.71

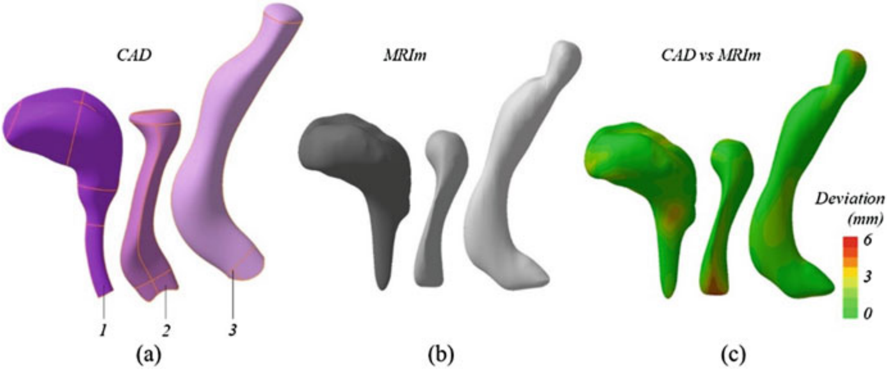

Fig. 4 (**a**) Initial CAD model of organs (1—bladder, 2—vagina, 3—rectum), (**b**) manual MRI reconstruction (segmented results) of the internal surfaces, (**c**) deviation between CAD model and computer-assisted MRI reconstruction

The rectum and bladder have larger deviations. The first reason is that the upper part of the rectum is not maintained contrary to vagina and thus is deformed by the gravity field during MRI acquisition. Similarly, the upper part of the bladder is also free. On these areas, the comparison with the CAD geometry shows a deviation up to 5 mm. The results are in accordance with the pixel size precision employed in clinical MRI protocol (pixel size at 0.7 mm and 3.5 mm between slice). An error about few pixels on manual selection leads us to this deviation order.

3.2 Comparison Between Computer-Assisted Reconstruction and Initial CAD Model

The same type of analysis was performed between our CAD model and the computer-assisted reconstruction (MRIca). However, the comparison is focused only on the internal surfaces. The use of axial images did not allow us to distinguish the external surface with good precision, as the contrast with the gel was not adapted (Fig. 3). The analysis presents a deviation about 0.99 mm (STD 0.71 mm) when we take into account the three organs.

The error is still in the same range of uncertainties than the manual reconstruction. If we consider the MRI resolution (pixel size and slice thickness), it is reasonable to obtain a 3D model that close (Fig. 5). At this stage, this computer-assisted method is considered partially manual. However, contrary to the raw mesh obtained by manual reconstruction (smoothed or not), the model is directly usable in simulation, and can be remeshed successfully and consistently to adapt the simulation if necessary. Most importantly, the time of creation of surface patches can be reduced. On this example, the operator used 25 points for initialization, and 91 points were added gradually to make the CAD geometry the closest to image

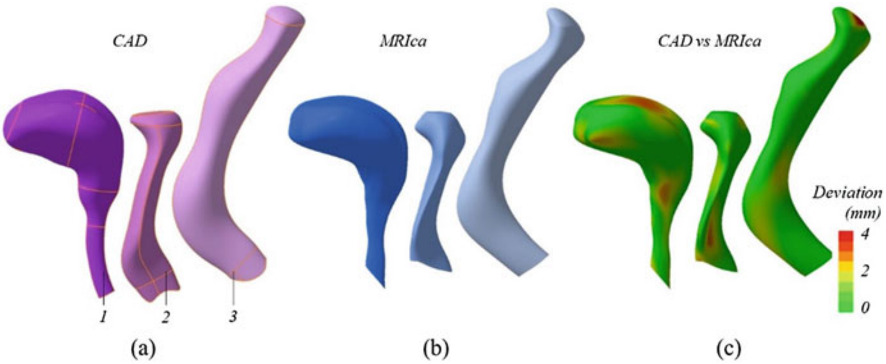

Fig. 5 (**a**) Initial CAD model of organs (1—bladder, 2—vagina, 3—rectum), (**b**) computer-assisted MRI reconstruction of the internal surface, (**c**) deviation between CAD model and manual MRI reconstruction

data, and the operation time was about 38 min. With the manual procedure for the geometry creation, an experienced operator needs 20 min to segment the three organs on MRI and 10 h to generate a surfaced model, ready to be used with FE meshing methods.

We have also developed a home-made integrated GUI (graphical user interface) which allows users to perform the geometry reconstruction. The characteristic points required by the proposed morphing can be picked easily with a 2D multi-slices view and a 3D geometry view. We have used the open source python package PyGeM [28], which implements various model reduction techniques [29], including RBF. Moreover, a procedure of refinement is also available for adding RBF characteristic points during the reconstruction.

4 Discussions

One of the advantages of this work consists in the computer-assisted approach to generating a 3D model of the organs. The manual reconstruction induces a considerable work during the contouring of the organs on many images; this means that it is very time-consuming and hardly repetitive work. The computer-assisted method allows us to avoid these main problems, commonly met in this application.

The use of a generic CAD model with geometrical morphing approach is a considerable benefit to generate a patient-specific geometry compatible with FE simulation, with a decrease of data processing time. Conventionally to succeed FE simulation, regard to the geometrical aspects on biomechanical context, the common approach involves multiple steps linked to image acquisition, segmentation of zones of interest, three-dimensional reconstruction, and consequent manual work to make these geometries compatible with the FE method. Using voxel-based segmentation is not suitable due to the incompatibility of classical 3D reconstruction from medical images with FE tools. Our method allows us to avoid doing this conventional approach by obtaining directly a surface model with a viable mesh for FE simulation. This mesh can be included in different FE solver codes in order to carry out simulations with compatible data. This perspective, which is essential to our approach, can be validated in the same methodology than previously published studies of pelvic system, related to the FE analysis of physiological and pathological mobility [18], surgery evaluation [30] or models dedicated to childbirth diagnosis [31, 32].

Even if the physical model is an interesting tool for quantifying measurement uncertainties, this tool does not represent a real patient in its complexity. Some structures were not taken into account during manufacture and morphing procedure. In patient-specific simulation, it will be necessary to include the anatomical structures of suspension. These structures are hardly detectable on conventional medical imaging, but they play a key role on organs mobility. Thus, the second major contribution consists in the possibility of deforming a more complex geometry with all these structures. Currently, the morphing method presented in this paper does not involve these structures. However, the described approach is compatible with this research field, as it is possible to morph a larger number of anatomical part. Introducing these additional parameters to our generic model will be a short-term target. Morphing an enriched model could contribute to help radiologists to simulate the anatomical structures despite missing information from MRI data.

5 Conclusion

This new method leads us to a surface model, compatible with CAD software and efficient in many research and medical applications such as FE simulation. This is a significant advance if we want to perform patient-specific analyzes. Applying this method to MRI images of real patients is not the immediate goal of this study. As the validation of the whole protocol on real patients is time and budget consuming, we decided to create a physical model and use it as an alternative validation tool at this stage of the study. The presented approach to the morphing of a generic CAD model of the pelvic organs can be applied on patient-specific MRI data in further studies. The compatibility with a clinical application leads to generate consist geometric models of the pelvic system, readily usable for FE analysis.

References

1. Samuelsson EC, Victor FT, Tibblin G, Svärdsudd KF (1999) Signs of genital prolapse in a Swedish population of women 20 to 59 years of age and possible related factors. Am J Obstet Gynecol 180(2):299–305
2. Swift SE (2000) The distribution of pelvic organ support in a population of female subjects seen for routine gynecologic health care. Am J Obstet Gynecol 183(2):277–285
3. Bump RC, Mattiasson A, Bø K, Brubaker LP, DeLancey JO, Klarskov P, Shull BL, Smith AR (1996) The standardization of terminology of female pelvic organ prolapse and pelvic floor dysfunction. Am J Obstet Gynecol 175(1):10–17
4. Dell'oro M, Collinet P, Robin G, Rubod C (2013) Multidisciplinary approach for deep endometriosis: interests and organization. Gynecol Obstet Fertil 41(1):58–64
5. Mayeur O, Witz JF, Lecomte-Grosbras P, Brieu M, Cosson M, Miller K (2016) Influence of geometry and mechanical properties on the accuracy of patient-specific simulation of women pelvic floor. Ann Biomed Eng 44:202–212
6. Lorensen WE, Cline HE (1987) Marching cubes: a high resolution 3D surface construction algorithm. In: Proceedings of the 14th annual conference on computer graphics and interactive techniques SIGGRAPH '87, pp 163–169
7. Shekhar R, Fayyad E, Yagel R, Cornhill JF (1996) Octree-based decimation of marching cubes surfaces. In: Proceedings visualization '96, pp 335–342
8. Paragios N, Chen Y, Faugeras O (2006) Handbook of mathematical models in computer vision. Springer, New York
9. Kass M, Witkin A, Terzopoulos D (1988) Snakes: active contour models. Int J Comput Vis 1(4):321–331
10. Chan TF, Vese LA (2001) Active contours without edges. IEEE Trans Image Process 10(2):266–277

11. Li B, Acton ST (2007) Active contour external force using vector field convolution for image segmentation. IEEE Trans Image Process 16(8):2096–2106
12. Semin B, Auradou H, François M (2011) Accurate measurement of curvilinear shapes by virtual image correlation. Eur Phys J Appl Phys 56(1):10701
13. Réthoré J, François M (2014) Curve and boundaries measurement using B-splines and virtual images. Opt Lasers Eng 52:145–155
14. Jiang Z, Witz JF, Lecomte-Grosbras P, Dequidt J, Duriez C, Cosson M, Cotin S, Brieu M (2015) B-spline based multi-organ detection in magnetic resonance imaging. Strain 51(3):235–247
15. Jiang Z, Witz JF, Lecomte-Grosbras P, Dequidt J, Cotin S, Rubod C, Duriez C, Brieu M (2017) Multiorgan motion tracking in dynamic magnetic resonance imaging for evaluation of pelvic system mobility and shear strain. Strain 53(2):e12224
16. Bay T, Chambelland JC, Raffin R, Daniel M, Bellemare ME (2011) Geometric modeling of pelvic organs. Conf Proc IEEE Eng Med Biol Soc 2011:4329–4332
17. Vallet A, Witz JF, Rubod C, Brieu M, Cosson M (2011) Simulation of pelvic mobility: topology optimization of ligamentous system. Comput Methods Biomech Biomed Eng 14(1):159–163
18. Mayeur O, Lamblin G, Lecomte-Grosbras P, Brieu M, Rubod C, Cosson M (2014) FE simulation for the understanding of the median cystocele prolapse occurrence. In: Bello F, Cotin S (eds) Biomedical simulation, vol 8789, pp 220–227
19. Kikinis R, Pieper SD, Vosburgh K (2014) 3D slicer: a platform for subject-specific image analysis, visualization, and clinical support. In: Jolesz FA (ed) Intraoperative imaging image-guided therapy, vol 3(19), pp 277–289
20. Kamina P (2014) Anatomie clinique: Tome 4, Organes urinaires et génitaux, pelvis, coupes du tronc, 3rd edn. Maloine, Paris
21. Delancey JO (1992) Anatomic aspects of vaginal eversion after hysterectomy. Am J Obstet Gynecol 166(6):1717–1724
22. Piegl L, Tiller W (1995) The NURBS book. Monographs in visual communication. Springer, Basel
23. Buhmann MD (2003) Radial basis functions: theory and implementations. (Cambridge monographs on applied and computational mathematics). Cambridge University Press, Cambridge
24. Wendland H (2005) Scattered data approximation. Cambridge University Press, Cambridge
25. Botsch M, Kobbelt L, Pauly M, Alliez P, Levy B (2010) Polygon mesh processing. CRC Press Taylor & Francis Group, Boca Raton
26. Manzoni A, Quarteroni A, Rozza G (2012) Model reduction techniques for fast blood flow simulation in parametrized geometries. Int J Numer Methods Biomed Eng 28(6–7):604–625
27. Mongillo M (2011) Choosing basis functions and shape parameters for radial basis function methods. SIAM Undergrad Res Online 4:2–6
28. PyGeM: Python Geometrical Morphing. Available at: https://github.com/mathLab/PyGeM
29. Tezzele M, Salmoiraghi F, Mola A, Rozza G (2017) Dimension reduction in heterogeneous parametric spaces with application to naval engineering shape design problems. arXiv preprint arXiv:1709.03298
30. Jeanditgautier E, Mayeur O, Brieu M, Lamblin G, Rubod C, Cosson M (2016) Mobility and stress analysis of different surgical simulations during a sacral colpopexy, using a biomechanical model of the pelvic system. Int Urogynecol J 27(6):951–957
31. Mayeur O, Jeanditgautier E, Witz JF, Lecomte-Grosbras P, Cosson M, Rubod C, Brieu M (2017) Evaluation of strains on levator ani muscle: damage induced during delivery for a prediction of patient risks. In: Computational biomechanics for medicine. Springer, Cham, pp 135–146
32. Lepage J, Cosson M, Mayeur O, Brieu M, Rubod C (2016) Pedagogical childbirth simulators: utility in obstetrics. Eur J Obstet Gynecol Reprod Biol 197:41–47

Numerical Analysis of the Risk of Pelvis Injuries Under Multidirectional Impact Load

Katarzyna Arkusz, Tomasz Klekiel, and Romuald Będziński

Abstract This work presents the results of a numerical analysis of the pelvic ring model subjected to multidirectional impact impulse loading. The action mechanism behind widespread pelvic fractures resulting from combined lateral, vertical, and longitudinal forces has not been sufficiently explained in the literature yet. The elaborated finite element model of the human pelvis based on CT scans contains a bi-layered structure of bone, varying stiffness of pelvic ligaments and hyperelastic behavior of cartilage. The numerical analysis was performed using a force value of 10 kN, equivalent to a velocity of 12 m/s acting in the range ±45° in each direction. The performed analysis indicates the von Mises stress is concentrated in the femur under lateral–vertical impact load, in the frontal part of the pelvic ring under vertical–lateral, and in the wings of the ilium under lateral–longitudinal impact load. The most extensive injuries to the pelvic ring were observed under vertical–longitudinal impact load, causing interruption of the pelvic continuity.

Keywords Finite element modeling · Pelvic injury · Multidirectional impact load

1 Introduction

According to data collected by the National Hospital Discharge Survey between 1990 and 2007, the population-adjusted incidence of pelvic ring fractures increased from 27.24 to 34.30 per 100,000 capita ($P < 0.001$) [1]. Due to the high mortality rate and widespread nature of pelvic fractures, the broader interests of researchers is focused on defining the mechanism of pelvic injuries, developing new surgical treatment methods as well as new protection using numerical methods.

The mechanism of pelvis fracture is well known and takes into account force type, severity, and direction as well as injury instability. The most widely used

---

K. Arkusz (✉) · T. Klekiel · R. Będziński
Division of Biomedical Engineering, Department of Mechanical Engineering, University of Zielona Gora, Zielona Gora, Poland
e-mail: k.arkusz@ibem.uz.zgora.pl

M. P. Nash et al. (eds.), *Computational Biomechanics for Medicine*,
https://doi.org/10.1007/978-3-030-15923-8_3

and recommended classification of pelvic ring fracture is the Young and Burgess classification which is a modification of the Tile classification [2]. According to this classification, the mechanisms of pelvic fracture are divided into lateral, vertical, and anterior–posterior compression.

Side impact load (specific to side-on crashes and pedestrian collisions) acting on the greater trochanter of the femur bone results in side compression of the pelvic girdle and its internal rotation. This causes an ischium fracture on the side of the impact. If distal sacroiliac ligaments stay undamaged, the internal rotation of the pelvis results in further fractures to the frontal part of the sacrum and the wing of the ilium [3, 4].

The mechanism of anterior–posterior compression of the pelvis (specific to front-impact car accidents) consists of external rotation torque on the half pelvis, resulting in open book fractures [5]. Initially, rupture of the symphysis pubis occurs and may appear in association with pubis fracture. Next, external rotation of the ilium causes posterior sacroiliac ligament tearing and vest until the posterior superior iliac spine touches the sacrum bone [6, 7].

The mechanism of shear forces applied vertically to the pelvis has been analyzed for falls from height which are largely limited to side impact [8, 9], and back falls [10]. The above-mentioned numerical analysis and overview of clinical cases [11, 12] allowed determining of the first fracture as the rupture of sacroiliac ligaments arising from the impact acting perpendicular to the pelvic floor. Further destruction includes the symphysis pubis or the pubis bone. Loss of the anterior and posterior ligament structures of the pelvic ring leads to vertical pelvic ring displacement resulting in pelvic instability and Malgaigne fracture [13]. Analysis performed by Song et al. on the strain distribution in the pelvic ring after high falls from 9 m indicates its bilateral concentration in areas consistent with Malgaigne fracture [14].

Due to the lack of experimental measurements resulting in sample availability and the possibility of crash accident imitation, numerical analysis provides the opportunity to complete the analysis of the pelvis injury mechanism [15]. The numerical analysis of pelvic fracture mechanism has been described in literature depending on low- and high-energy accidents [16], and also on the direction of impact load [17]. The above-mentioned numerical analysis and overview of clinical cases does not take into account the effect of different angles of impact direction. This has a significant influence on the multidirectional pelvic fracture mechanism through changes to stress distribution in the pelvic ring. Determination of the pelvic fracture mechanism under combined direction of impact load in each plane of motion, i.e., sagittal, horizontal, and frontal—which is the aim of this work, makes a significant contribution to the Young and Burgess classification of pelvic ring fracture.

2 Methodology

The pelvic model (LPC, Fig. 1) was developed based on computed tomography (CT) scan images of a healthy patient using an 8-row spiral CT with an accuracy of 2.5 mm (Szamotuly District Hospital, Poland). No ethical approval was necessary from the local ethical committee because only archived data were used; however, patient gave informed consent according to the principles of the Helsinki Declaration. The cortical and trabecular microstructures of the sacrum, ilium, and femur (mechanical properties are shown in Table 1) were exported to STL files using MIMICS software then further re-meshed using MeshLab software for smoothing individual surfaces. The mesh of finite elements was generated in Ansys 16.2 software as 8-node tetrahedral (56,053 elements).

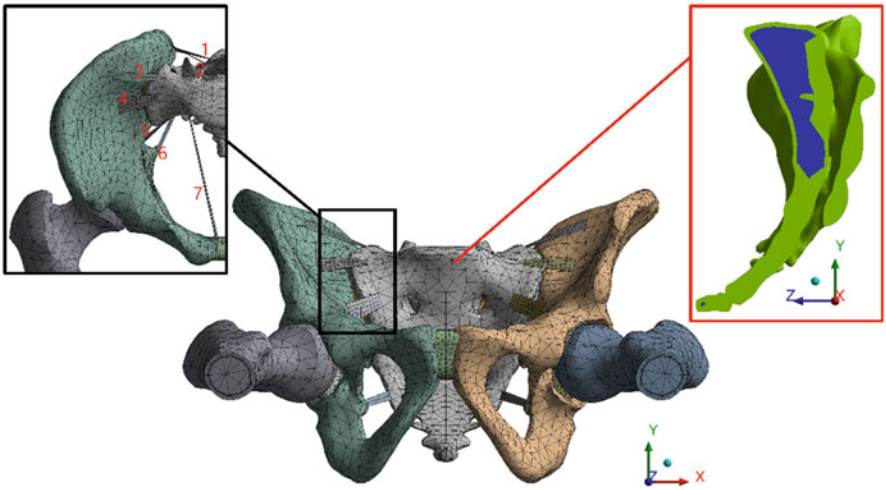

Fig. 1 FE pelvic model used to determine the extent of injuries under multidirectional load, where 1–2—posterior sacroiliac ligaments, 3–5—anterior sacroiliac ligaments, 6—sacrotuberous, 7—sacrospinous ligaments

Table 1 Material properties of the anatomical structures of the pelvic ring used in an elaborated FE model [19]

No	Name	Young's modulus (MPa)	Poisson's factor
1	Sacrum—cortical bone	18,000	0.3
2	Sacrum—trabecular bone	132	0.3
3	Pelvis—cortical bone	17,000	0.3
4	Pelvis—trabecular bone	140	0.3
5	Femur—cortical bone	17,000	0.3
6	Femur—trabecular bone	140	0.3
7	Sacroiliac joint cartilage	54	0.2
8	Symphysis pubic	54	0.2

Table 2 Material properties of ligaments responsible for stabilizing the pelvic ring [20]

Ligament name	Width s (mm)	Length L (mm)	Stiffness k (N/m)	Young's modulus E (MPa)	Area A (mm^2)	Thickness g (mm)
Anterior sacroiliac						
1	7.4	30	21,000	355	1.58	0.1582
2	10.78	31				
3	11.59	26				
4	10.23	20				
Posterior sacroiliac						
1	8.84	28	18,900	355	1.72	0.1906
2	9.38	35				
3	8.88	34				
Sacrotuberous	5.95	36	12,600	355	1.28	0.2147
Sacrospinous	10.74	106	22,500	355	6.72	0.6255

Due to the lack of experimental data, pelvic ligaments were modeled as one-dimensional line elements, acting as linear springs, where mechanical properties are shown in Table 2. The hip capsules were modeled as the part of the acetabulum and provided to prevent disconnection of the hip and femur bones. The material properties for these capsules were estimated based on the tangent modulus determined by Hewitt et al. [12]. The Young's modulus was calculated as the average stress measured from 0% to 80% of strain in the capsule. In the results, the mean value was assumed to be the same as for articular cartilage material in the acetabulum. The articular cartilages were modeled using neo-Hookean model (MU1—13.6 MPa, D1—0.3). The constitutive model (neo-Hookean) was used because of the small number of constants to optimize, which use a non-linear relationship between stress and strain to describe incompressible hyperelastic materials. The role of muscle was omitted in this research due to the short time of analysis—10 ms, in which muscle activation will not occur [18], and due to the high impact load applied to the pelvis ring.

2.1 Boundary Condition

The numerical analysis was performed using the force value 10 kN—force causing first fracture in pelvic complex [10] equivalent to velocity of 12 m/s acting in lateral (X), vertical (Y), and longitudinal (Z) direction, perpendicular to the right greater trochanter of the femur, to the right inferior pubic ramus, and to the cross-section of right femur, respectively. In order to determine the influence of different angles, the load was changed in the range ±45° in each direction. To obtain the effect of fastened seat-belts limiting pelvic movements, the model translation was only accepted in the vertical direction: at the top of the sacrum by mass value 50 kg, and at the iliac crest by seat belts modeled as a spring with stiffness 98.1 kN/mm. The analysis was performed during 10 ms.

3 Results and Discussion

The elaborated FE model of pelvic ring (Fig. 1) consisted of a significant element ignored by other authors, i.e., cortical and trabecular microarchitecture [14]; ligaments responsible for keeping the weight of the trunk and upper limbs, preventing the herniation of the sacrum between the ilium bones, providing stability and attenuate forces on the lower extremities and the spine as well as preventing the sacrum bending back [21]; joint cartilages modeled according to its anatomical shape, including the lumbosacral joint [20]. Due to the complexity of the elaborated LPC model, the possibility of application of a Hounsfield unit scale and local variations in anisotropy or microarchitecture was excluded. Despite these limitations, the validation of the LPC model proves its correctness and this study successfully demonstrated the effects of force direction on the predictions of pelvic fracture.

Validation of the elaborated LPC model was performed in previous papers through the simulation of physiological stress distribution during sitting [19] and also according to the biomechanical experiments under vertical force [13]. The validation of the LPC model was performed in three steps. Firstly, based on experimental research carried out on formalin-preserved cadaveric pelvis mounted on a BOSE Electroforce 3250-AT under vertical force loaded from 0 to 500 N on the top of the sacrum body [22]. The performed validation indicated a statistical significance (R2 = 0.975 under 500 N) for fitting the strain values obtained in the biomechanical experiment and in the LPC model under different loads. The second validation of the LPC model was performed according to the analysis of the literature on stress distribution in the pelvic ring during sitting. Zhou et al. [23] indicated the maximum stress concentration in the greater sciatic notch. Stress also occurs in the sacroiliac joint and acetabulum regions including the ischium bones. These stress concentration regions are almost identical with our results. Finally, the LPC model was also validated by the stress distribution under side and front-impact load, value 15 kN, concentrated in the greater trochanter and on the cross-section of the femur, respectively. Our obtained results are identical with research by Dawson et al. [24], Majumder et al. [25] and are in accordance with the Young and Burgess classification [2]. The performed validation allows to confirm the expected stress/strain distribution in the pelvic ring in different condition, i.e., static and dynamic, low- and high-energy load.

Many authors [8, 10, 14] have suggested that the criteria for bone failure are difficult to define and not fully explained. In the paper we chose the maximal von Mises stresses as failure criteria. This assumption was satisfactory, because the significant factor in our investigation was the relationship between bone stress state and its strength. The level of the von Mises stresses concentrated in the cortical part of the bones is a simple method for estimating risk of injury, because the stress concentration on certain parts of the bone suggests a potential injury, and the probability is proportional to the stress value.

The following critical conditions were applied to injuries to pelvic structures [26]:

- Bone:
  - Tensile strength (age 20–39 years): 125 MPa
  - Deformation causing cracking: 1.5%
- Sacroiliac cartilage:
  - Tensile strength: 25 MPa
  - Deformation resulting in a breakage: 30%

The stress distribution in the pelvic ring under lateral impact load (load acting perpendicular in the X-axis) is shown in Fig. 2. The maximum von Mises stress was accumulated in the left ischial tuberosity on the side of impact (131 MPa), causing the first fracture in the pelvic ring under side impact load (Fig. 2a). This value is consistent with the data in the literature [3, 4, 19]. Further analysis pointed to the maximum von Mises stress (101 MPa) in the left ilium. These are, however, not destructive forces, confirming the internal rotation of the pelvis and destruction of sacroiliac ligaments (elongation 14.5% exceeding the ultimate elongation 7%).

Changing the force direction by 45° in the vertical (up) translation (Fig. 2b) caused the concentration of the von Mises stress to manifest in the left femoral head (162 MPa). Changing the force direction by 45° in the vertical (down) translation (Fig. 2c) caused the concentration of the von Mises stress to manifest in the left femoral neck (154 MPa). Fractures also occurred in the left superior pubic ramus (132 MPa) and in the right inferior pubic ramus (149 MPa). Performed analysis indicates that changing the lateral impact force in the vertical direction causes the von Mises stress to concentrate in the femur, confirming the increasing incidence of hip fracture, especially in elderly people [27]. More extensive injuries were observed during down-lateral impact load.

Changing of the lateral impact load by 45° in a longitudinal translation (Fig. 2d, e) significantly increases the maximum von Mises stress concentrated in the pelvic ring. The maximum von Mises stress (373 MPa) was localized in the left inferior pubic ramus as the only fracture appearing in the case of posterior-lateral impact load (Fig. 2d). Changing the direction of impact load to an anterior-lateral translation (Fig. 2e) resulted in fractures of the left inferior pubic ramus (344 MPa), and left superior pubic ramus (172 MPa). Further transfer of von Mises stress by the sacrotuberous ligaments resulted in a right superior pubic ramus fracture. Load resulting from the posterior and lateral directions caused the concentration of stress in the front pelvic ring, preventing the stress distribution to the sacrum bone by sacroiliac ligaments and resulting in widespread fractures. The obtained results indicate that longitudinal changing of lateral impact load increases the load distribution through the pubic symphysis, which is characteristic for acetabulum impact for dynamic tests [21].

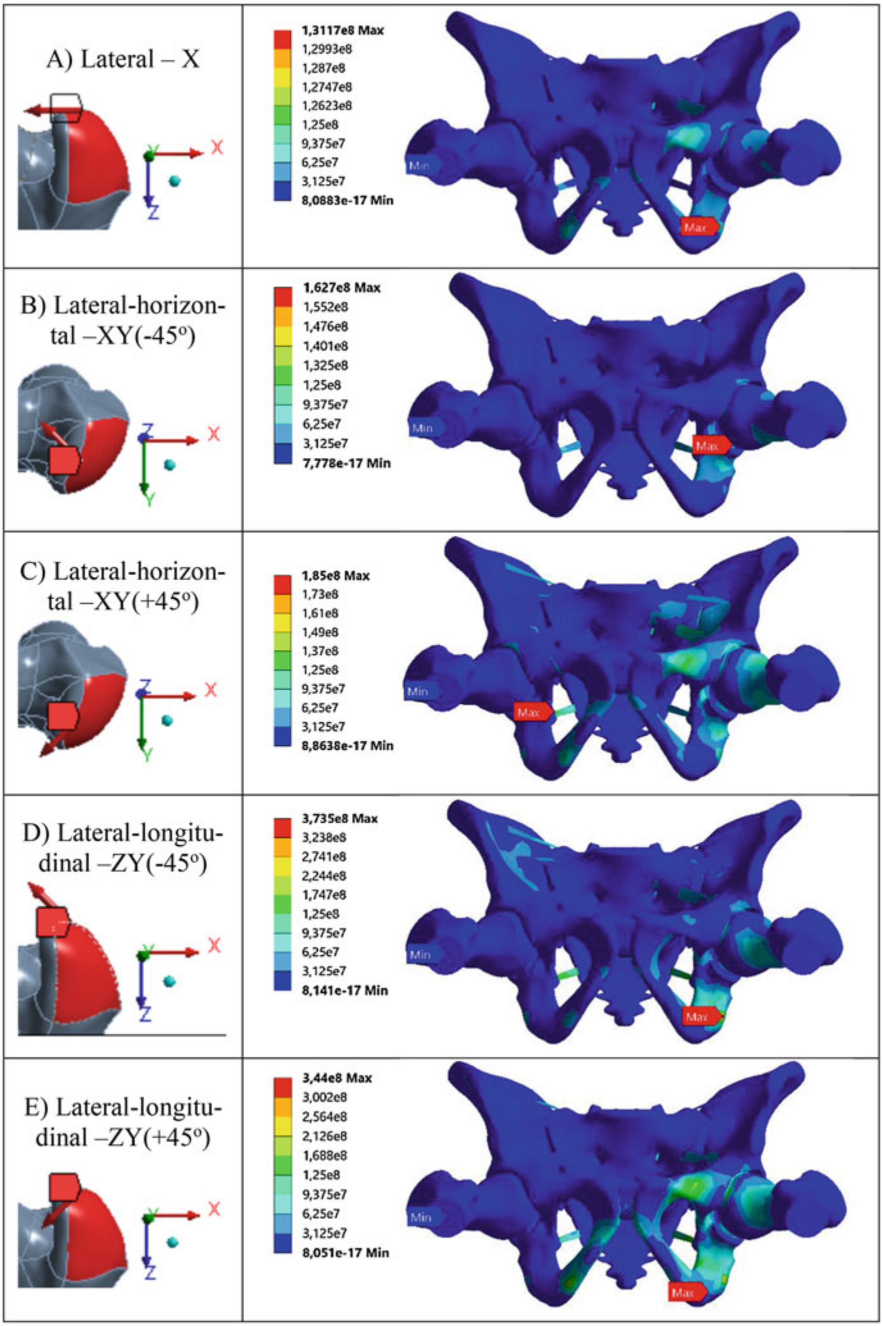

Fig. 2 Stress distribution in the pelvic–hip complex under lateral impact load acting perpendicular to the left greater trochanter of the femur and in varying direction, where the forces impact in direction: (**a**) lateral, (**b**) lateral–horizontal (vector at −45°), (**c**) lateral–horizontal (vector at +45°), (**d**) lateral–longitudinal (vector at −45°), (**e**) lateral–longitudinal (vector at +45°)

The influence of the lateral and longitudinal translation on the pelvic ring fracture under vertical impact load is shown in Fig. 3. The maximum von Mises stress was recorded in the right ischial tuberosity (391 MPa) under shearing forces (Fig. 3a). Other destructive stresses were localized in the right pubic arch (149 MPa), in the left superior pubic ramus (136 MPa), and in the right wing of the ilium (137 MPa). Interruption of the left sacroiliac and sacrotuberous ligaments was also observed.

Vertical impact load translated by 45° in a lateral direction results in von Mises stress concentration in the front part of the pelvic ring. The first fracture occurred in the left inferior ramus of the pubis in the closed area of pubic symphysis (154 MPa). Further stress concentration resulted in a fracture of the right ischial ramus. Changing the direction of impact by $+45°$ in the X-axis resulted in injuries to the left (235 MPa) and right (323 MPa) greater sciatic notches and to the left (150 MPa) and right (157 MPa) inferior pubic rami. Further analysis pointed to the maximum stress (104 MPa) being in the right ischial tuberosity. Changing the impact load direction to outside the pelvic ring resulted in stress concentration in the frontal area of the pelvic ring, while a horizontal impact load directed inwards to the pelvis caused higher homogeneous stress distribution to the wing of the ilium and sacrum.

Posterior-horizontal impact load acting on the cross-section of the right femur resulted in maximum von Mises stress concentrated in the right ischial ramus (137 MPa). An anterior-vertical impact load caused more widespread fracture of the right ischial ramus (356 MPa), right superior ramus of the pubis (229 MPa), and iliac fossa (178 MPa).

The mechanism of longitudinal compression of the pelvis indicated the first fracture in the left ischial tuberosity (375 MPa) as a result of the acting force (Fig. 4a). Further injuries included the left pubic body (175 MPa) and the right inferior pubic ramus (275 MPa). These results are consistent with analysis by Fu et al. [6] indicating pubis fracture in the area of the symphysis pubis as the first rupture in the pelvic ring. The sacroiliac ligaments were undamaged; therefore, an “open book” fracture was not reported [7].

Changing the direction of anterior load by 45° in a lateral direction towards the pelvic ring resulted in an additional fracture in the neck of the femur (277 MPa). Previously described fractures also occur in this case. An applied anterior impact load directed by 45° in an external direction caused the maximum von Mises stress concentration to manifest in the left (379 MPa) and right (226 MPa) ischial tuberosity, in the pubis (241 MPa), and also in the neck and head of the femur (270 MPa).

An anterior-vertical (down) impact load resulted in a changing concentration of maximum von Mises stress in the neck of the femur (197 MPa) and fracture of the pubic bone (168 MPa) was observed. An anterior-vertical (up) impact load caused stress distribution into the wing of the pelvic and sacrum bones. The maximum von Mises stress confirmed the fracture of the left neck of the femur (195 MPa), the left ischial tuberosity (442 MPa), and the left inferior pubic ramus (134 MPa).

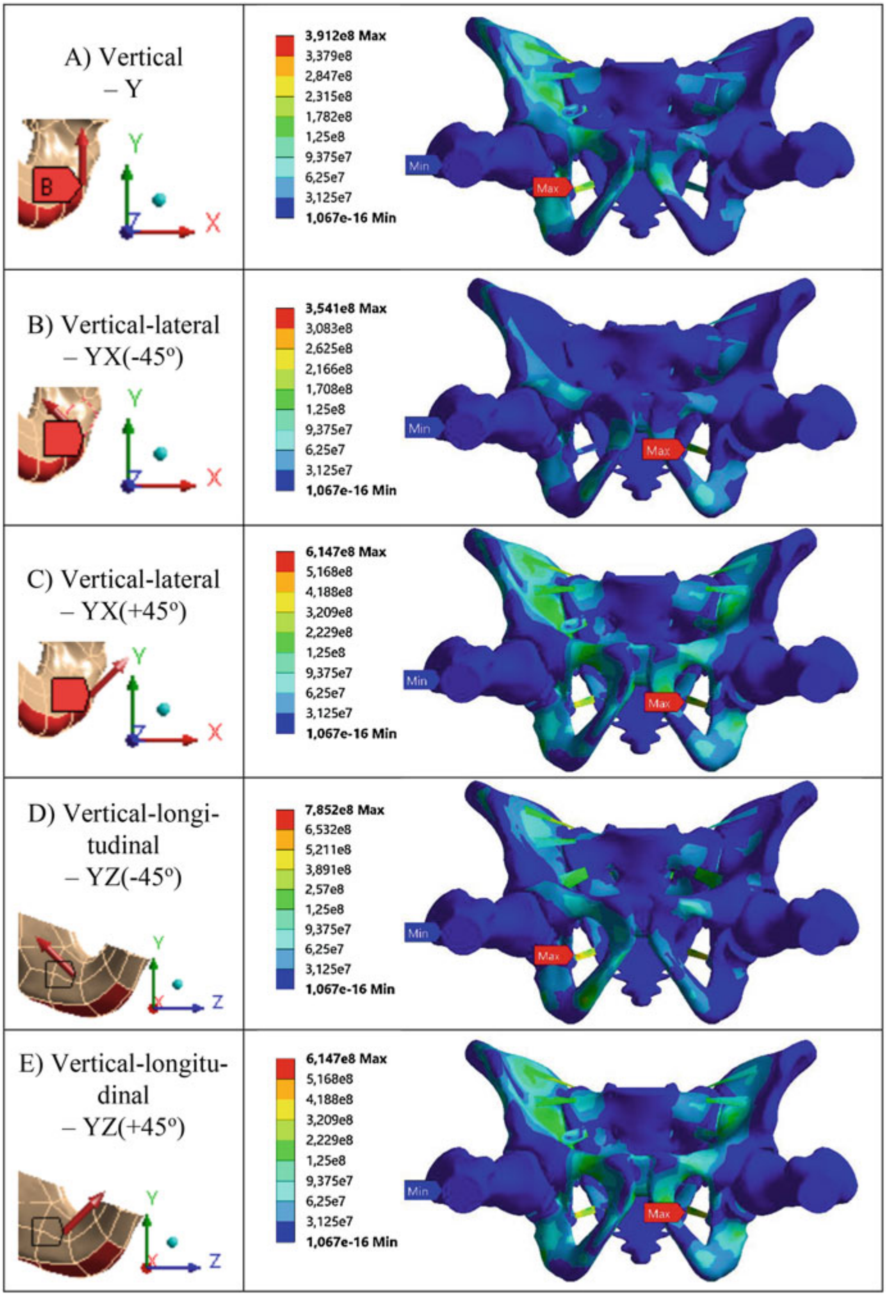

Fig. 3 Stress distribution in the pelvic ring under vertical impact load acting perpendicular to the inferior pubic rami, where the forces impact in direction: (**a**) vertical, (**b**) vertical–lateral (vector at −45°), (**c**) vertical–lateral (vector at +45°), (**d**) vertical–longitudinal (vector at −45°), (**e**) vertical–longitudinal (vector at +45°)

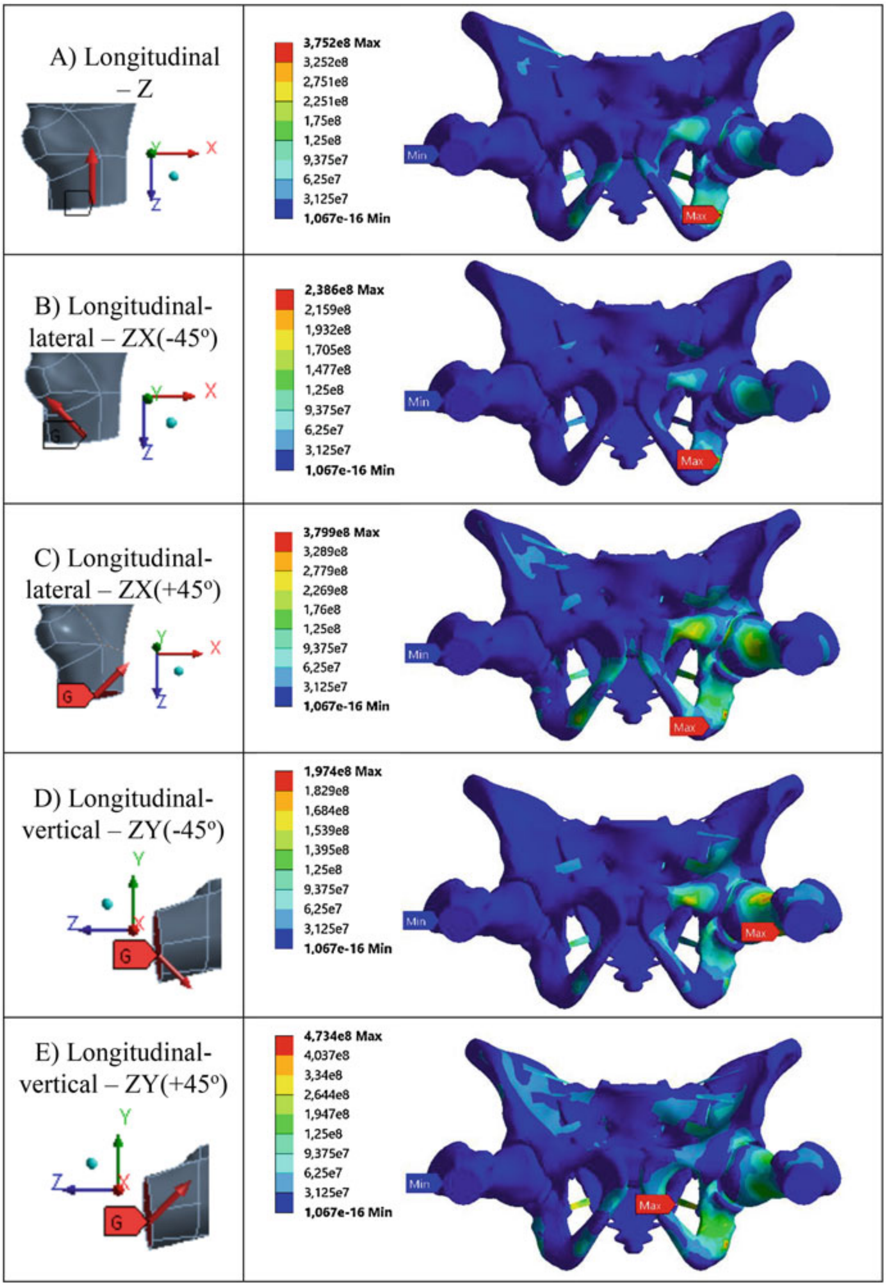

Fig. 4 Stress distribution in pelvic ring under longitudinal impact load acting perpendicular to the cross-section of right femur, where the forces impact in direction: (**a**) longitudinal, (**b**) longitudinal–lateral (vector at −45°), (**c**) longitudinal–lateral (vector at +45°), (**d**) longitudinal–vertical (vector at −45°), (**e**) longitudinal–vertical (vector at +45°)

4 Conclusions

The aim of this work was to determine the mechanism of pelvic fracture under multidirectional impact load, and the influence of impact load combined in all directions on stress distribution in the pelvic ring. Hitherto, different angles of acting force were only analyzed for a single direction. The obtained results allowed us to determine the intermediate mechanism of the pelvic ring under lateral (X), vertical (Y), and longitudinal (Z) impact loads.

Performed analysis indicates that changing the lateral impact force in a vertical direction causes the von Misses stress concentration in the femur, confirming the increasing incidence of hip fracture, especially in elderly people [27].

Multidirectional vertical–lateral impact load results in von Mises stress concentration in the frontal area of the pelvic ring. Changing the lateral impact load direction to outside the pelvic ring results in stress concentration in the front part of the pelvic ring, while a horizontal impact load directed inwards to the pelvis causes higher homogeneous stress distribution to the wing of the ilium and sacrum.

The combination of anterior impact load in lateral and vertical directions results in increasing von Mises stress transfer to the wings of the ilium and widespread damage to the ischium and pubic bones.

In conclusion, the most extensive injuries to the pelvic ring were observed under vertical–longitudinal impact load, causing major interruption of pelvic continuity.

References

1. Buller LT, Best MJ, Quinnan SM (2016) A Nationwide analysis of pelvic ring fractures: incidence and trends in treatment, length of stay, and mortality. Geriatr Orthop Surg Rehabil 7(1):9–17
2. Alton TB, Gee AO (2014) Classifications in brief: Young and Burgess classification of pelvic ring injuries. Clin Orthop Relat Res 472(8):2338–2342
3. Salzar RS, Genovese D, Bass CR, Bolton JR, Guillemot H, Damon AM, Crandall JR (2009) Load path distribution within the pelvic structure under lateral loading. Int J Crashworthiness 14(1):99–110
4. Weinlein JC, Mashru RP, Perez EA, Johnson SE (2018) Lateral compression-I pelvic ring injury: not benign to the developing Fetus. J Orthop Trauma 32(2):100–103
5. Salzar RS, Bass CR, Kent R, Millington S, Davis M, Lucas S, Rudd R, Folk B, Donnellan L, Murakami D, Kobayashi S (2006) Development of injury criteria for pelvic fracture in frontal crashes. Traffic Inj Prev 7:299–305
6. Fu CY, Hsieh CH, Wu SC et al (2013) Anterior-posterior compression pelvic fracture increases the probability of requirement of bilateral embolization. Am J Emerg Med 31(1):42–49
7. Lopez-Valdes FJ, Riley PO, Lessley DJ, Arbogast KB, Seacrist T, Balasubramanian S, Maltese M, Kent R (2014) The six degrees of freedom motion of the human head, spine, and pelvis in a frontal impact. Traffic Inj Prev 15:294–301
8. Majumder S, Roychowdhury A, Pal S (2007) Simulation of hip fracture in sideways fall using a 3D finite element model of pelvis–femur–soft tissue complex with simplified representation of whole body. Med Eng Phys 29(10):1167–1178

9. Hanger HC (2017) Low-impact flooring: does it reduce fall-related injuries? J Am Med Dir Assoc 18(7):588–591
10. Majumder S, Roychowdhury A, Pal S (2008) Effects of trochanteric soft tissue thickness and hip impact velocity on hip fracture in sideways fall through 3D finite element simulations. J Biomech 41(13):2834–2842
11. Reynolds BM, Balsano NA, Reynolds FX (1971) Falls from heights: a surgical experience of 200 consecutive cases. Ann Surg 174(2):304–308
12. Hewitt J, Guilak F, Glisson R, Vail P (2001) Regional material properties of the human hip joint capsule ligaments. J Orthop Res 19:359–364
13. Arkusz K, Klekiel T, Sławiński G, Będziński R (2019) Influence of energy absorbers on Malgaigne fracture mechanism in lumbar-pelvic system under vertical impact load. Comput Methods Biomech Biomed Eng 1025–5842:1–11
14. Song R, Liu J, Wang W, Cui M (2016) Dynamic simulation of lumbar vertebrae and pelvis in human falls. Acta Medica Mediterranea 32:593–597
15. Klekiel T, Arkusz K, Sławiński G, Będziński R (2019) Prediction of the segmental pelvic ring fractures under impact loadings during car crash. In: Arkusz K, Będziński R, Klekiel T, Piszczatowski S (eds) Biomechanics in medicine and biology. BIOMECHANICS 2018. Advances in intelligent systems and computing, vol 831. Springer, Cham
16. Soles GLS, Ferguson TA (2012) Fragility fractures of the pelvis. Curr Rev Musculoskelet Med 5(3):222–228
17. Guthrie H, Owen R, Bircher M (2010) Fractures of the pelvis. J Bone Joint Surg (Br) 92:1481–1488
18. Martel DR, Levine IC, Pretty SP, Laing AC (2018) The influence of muscle activation on impact dynamics during lateral falls on the hip. J Biomech 66:111–118
19. Arkusz K, Klekiel T, Niezgoda TM, Będziński R (2018) The influence of osteoporotic bone structures of the pelvic-hip complex on stress distribution under impact load. Acta Bioeng Biomech 20(1):29–38
20. Shi D, Wang F, Wang D, Li X, Wang Q (2014) 3-D finite element analysis of the influence of synovial condition in sacroiliac joint on the load transmission in human pelvic system. Med Eng Phys 36(6):745–753
21. Fan Y, Lei J, Zhu F, Li Z, Chen W, Liu X (2015) Biomechanical analysis of the fixation system for t-shaped acetabular fracture. Comput Math Methods Med 2015:1–10
22. Hu P, Wu T, Wang HZ, Qi XZ, Yao J, Cheng XD, Chen W, Zhang YZ (2017) Influence of different boundary conditions in finite element analysis on pelvic biomechanical load transmission. Orthop Surg 9(1):115–122
23. Zhou Y, Min L, Liu Y, Shi R, Zhang W, Zhang H, Duan H, Tu C (2013) Finite element analysis of the pelvis after modular hemipelvic endoprosthesis reconstruction. Int Orthop 37:653–658
24. Dawson JM, Khmelniker BV, Mcandrew MP (1999) Analysis of the structural behavior of the pelvis during lateral impact using the finite element method. Accid Anal Prev 31:109–119
25. Majumder S, Roychowdhury A, Pal S (2008) Three-dimensional finite element simulation of pelvic fracture during side impact with pelvis–femur–soft tissue complex. Int J Crashworthines 13:313–329
26. Dehghani F, Fathi A (2017) Challenges for Cartilage Regeneration. In: Li Q, Mai YW (eds) Biomaterials for implants and scaffolds. Springer, Berlin
27. Caracchini G, Cavalli L (2010) Severe osteoporosis: diagnosis of femoral fractures. Clin Cases Miner Bone Metab 7(2):97–101

Parametric Study of Lumbar Belts in the Case of Low Back Pain: Effect of Patients' Specific Characteristics

Rébecca Bonnaire, Woo-Suck Han, Paul Calmels, Reynald Convert, and Jérôme Molimard

Abstract *Objective*: A numerical 3D model of the human trunk was developed to study the biomechanical effects of lumbar belts used to treat low back pain.

Methods: This model was taken from the trunk radiographies of a person and simplified so as to make a parametric study by various morphological parameters of the patient, characteristic parameters of the lumbar belt and mechanical parameters of body and finally to determine the parameters influencing the effects of low back pain when wearing the lumbar belt. The loading of lumbar belt is modelled by Laplace's law. These results were compared with clinical study.

Results: All the results of this parametric study showed that the choice of belt is very important depending on the patient's morphology. Surprisingly, the therapeutic treatment is not influenced by the mechanical characteristics of the body structures except the mechanical properties of intervertebral discs.

Discussion: The numerical model can serve as a basis for more in-depth studies concerning the analysis of efficiency of lumbar belts in low back pain. In order to study the impact of the belt's architecture, the pressure applied to the trunk modelled by Laplace's law could be improved. This model could also be used as the basis for

---

R. Bonnaire
Institut Clément Ader (ICA), Université de Toulouse, CNRS, IMT Mines Albi, INSA, ISAESUPAERO, UPS, Albi, France

Campus Jarlard, Albi, France

W.-S. Han (✉) · J. Molimard
Mines Saint-Etienne, Université Jean Monnet, INSERM, UMR1059, SAINBIOSE, CIS-EMSE, Saint-Etienne, France
e-mail: han@emse.fr

P. Calmels
Laboratory of Exercise Physiology (LPE EA4338), University Hospital of Saint-Etienne, Hôpital Bellevue, Saint-Etienne, France

R. Convert
Thuasne, Saint-Etienne, France

M. P. Nash et al. (eds.), *Computational Biomechanics for Medicine*,
https://doi.org/10.1007/978-3-030-15923-8_4

a study of the impact of the belt over a period of wearing time. Indeed, the clinical study shows that movement has an important impact on the distribution of pressure applied by the belt.

Keywords Medical device · Articular contention · Lumbar belt · Low back pain · Mechanical model

1 Introduction

Low back pain is a frequent disease which induces high cost to society in developed countries. So, from prevention to disability, a lot of treatments are proposed. Low back pain is clinically described by physiopathological characteristics and its duration, from acute to chronic form [1]. One of the treatments for low back pain is the use of a lumbar orthotic device. The objectives of this device are to reduce mobility, decrease pain [2] and medication used which could induce some risks of iatrogenic complications.

The clinical efficacy of lumbar belt has been shown in the event of subacute and chronic low back pain [2]. However, a few studies exist that clearly elucidate all the mechanisms of action proposed for this orthotics. After these studies, we could conclude that lumbar orthoses:

- Limit the motion range of the trunk [3–5];
- Reduce disc stresses by increasing the abdominal pressure [6–8];
- Correct the posture by modifying lumbar lordosis [9–11];
- Have no negative impact on muscle strength [12–15];
- Have muscle-relaxing effects [16–19];
- Facilitate trunk mobility for daily living activities [2, 18].

No overall study of the mechanisms of action of lumbar belts and no study based on numerical modelling of their effects on the trunk to reduce low back pain were found through the review of the literature.

However, numerous models exist for the human trunk and, more specifically, the spine. These models can be divided into three types: detailed models, simplified models and hybrid models, i.e. containing both highly detailed zones and highly simplified zones. Numerical models have been used, for example, to compare the influence of parameters for surgical treatments or other techniques [20–22], to analyse the deformation of the spine [23–25] or the effect of carrying a load [26, 27]. One study on the mechanisms of action of rigid orthosis in the treatment of scoliosis appears to be similar to the present study and report that biomechanical analysis using computational modelling could be useful in the design of rigid orthosis [28].

In this finite element analysis (FEA), a lumbar orthosis, named lumbar belt, was studied. This orthosis is a common treatment of subacute or chronic low back pain. The main objective of this study is to evaluate the parameters that can influence the choice of lumbar belts types to treat low back pain, using a finite elements model. The studied parameters will be related to the patient's morphology, the belt and the mechanical characteristics of the human trunk.

2 Methodology

The aim is to perform a screening of the factors influencing the global mechanical effect of the belt. For this purpose, a simplified numerical model was built so as to change easily trunk geometry according to different typical patients. Unfortunately, this induces a compromise between computing time and precision on the results. The model might not render properly local effects but must be reliable on global ones. Indeed, a special attention must be done on the spine modeling, because pain is supposed to be caused from intervertebral discs. The geometry is simplified on trunk and vertebrae. Finally, the mechanical behavior is assumed to be linear and a simple Laplace law simulates the pressure applied by the belt. All these assumptions make a parametrical study possible, even if they track important limitations.

2.1 Trunk Modelling

2.1.1 Construction of Geometric Model

A simplified 3D model of the human trunk was developed for FEA. This model is built using frontal and sagittal radiographies of the trunk of one person. Using these radiographies, the following elements are measured:

- The lateral inclination of each intervertebral endplate in the sagittal plane,
- The height at their center of the thoracic and lumbar vertebrae,
- The diameter of the vertebral anterior segment at thoracic and lumbar level,
- The height at their center of the intervertebral discs in the thoracic and lumbar regions,
- The width of the trunk at the chest, below the chest, at the waist and hips in the frontal plane,
- The thickness of the trunk at the chest, below the chest, at the waist and hips in the sagittal plane.

Each vertebra is modelled as a cylinder based on the radiographs. Lumbar lordosis and thoracic kyphosis are constructed using two circle arcs obtained, thanks to the lateral inclinations of each vertebral endplate. It is assumed that the vertebra have parallel lower and upper endplates. The posterior segment of vertebra is not represented in this model since their action is assumed to be negligible for this study. The intervertebral discs are also modelled as a cylinder having two distinct parts: a central circular part corresponding to 30% of the volume representing the nucleus and a peripheral part representing the annulus [29].

The tissues composing the trunk, excluding the spinal column, are divided into three zones in order to represent the abdomen, the iliac crests and one other part including the thorax and the soft tissues in the back zone (see Fig. 1). This geometric model is simplified to easily change the trunk morphology in the simulation and

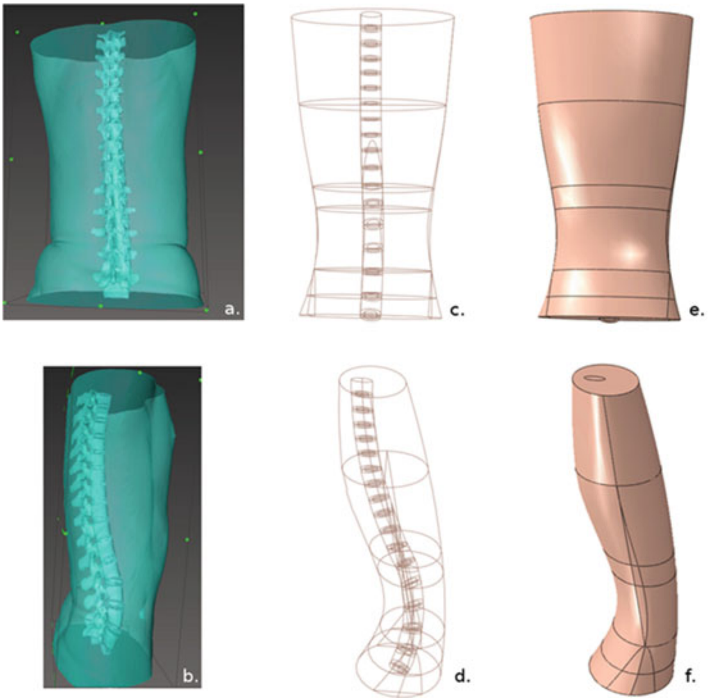

Fig. 1 Representation of modelling of trunk geometry for this study: trunk geometry before modelling (**a**) from the back (**b**) in profile; modelled trunk geometry (**c**) and (**e**) from the back, (**d**) and (**f**) in profile. Figures (**a**) and (**b**) are free of copyright from: https://www.osirix-viewer.com/resources/dicom-image-library/

realize the parametric studies. The surface of the trunk, corresponding to the skin, has different mechanical properties from the rest of the volume. This skin has a thickness of 4 mm; the value was determined by ultrasound on the trunk of two human subjects (see Fig. 2).

2.1.2 Finite Element Modelling of the Trunk

The geometry is meshed using ten-node tetrahedral second-order elements (C3D10H) using ABAQUS. Figure 3 shows a meshed model of the trunk. To determine the appropriate number of elements, a convergence study was done. This study consists in determining the mean abdominal and intradiscal pressure in the lumbar region as a function of the mean size of the elements. This study was carried out on the eight subjects chosen in this study, described in the next Sect. 2.2.

For the purpose of ensuring model simplicity, all the structures have elastic linear mechanical properties. As this study is a first approach, it would be interesting to modify this hypothesis in a future work. Mechanical properties can vary as a

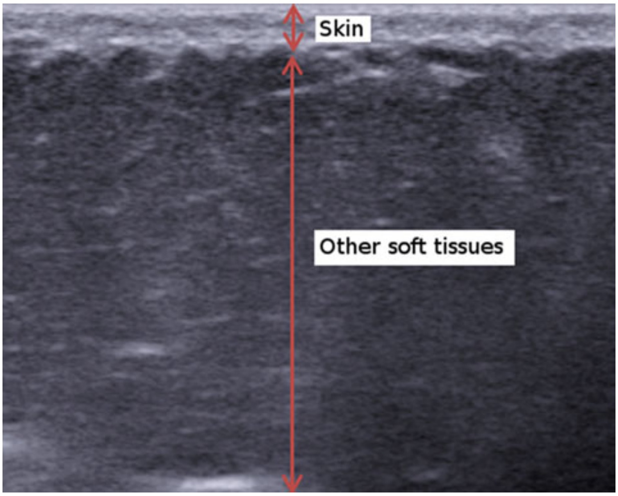

Fig. 2 Ultrasound image used to measure the thickness of the skin at the trunk. This was taken by one of co-authors on himself

function of the age and musculature of the subject modelled. They are therefore considered as design parameters during this study.

After studies on different sets of boundary conditions, these were determined in order to obtain realistic movement of the trunk under the loading of the belt. When a patient wears a belt, the pelvis can rotate slightly relative to the transverse axis. In addition, the patient tends to straighten up. It was therefore decided to block the upper plate of the trunk in translation in the transverse plane. The top of the trunk can translate in the frontal plane. The lower plate of the trunk is restricted in order to enable rotation of this plate only in the transverse axis. This restriction is obtained by embedding the two points at the intersection of the ellipse, representing the extremity of the lower plate of the trunk, and the frontal plane of the trunk. The boundary conditions are represented in Fig. 3.

2.1.3 Modelling of the Lumbar Belt

Lumbar belts are medical devices composed primarily of fabric in which four steel whales are inserted in the dorsal part and a flexible whale in the front part. They may consist of one or several layers of fabric. In this finite element model, it was opted to represent the lumbar belt globally as application of pressure to the lumbar region of the trunk. The bottom of the belt is located at the lower endplate of lumbar vertebra L4. This pressure is obtained by the following Laplace's law [30]:

$$\begin{array}{l} P = \frac{T}{R} \quad \text{if } T \text{ and } R > 0 \\ P = 0 \quad \text{if } T \text{ and } R \leq 0 \end{array} \tag{1}$$

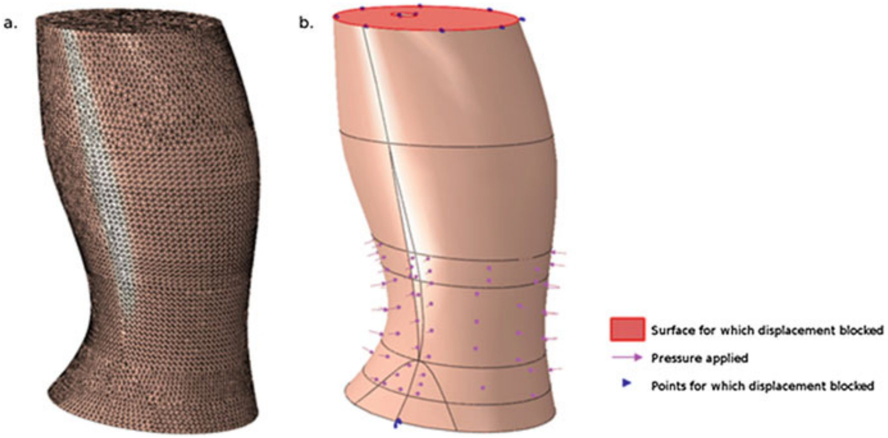

Fig. 3 Representation: (**a**) of meshing of the finite trunk element model and (**b**) of conditions at the limits

where T is the linear tension of the belt on the trunk and R the radius of curvature of the trunk at the pressure application point. The linear pressure of the lumbar belt used in this study was obtained by tensile tests on the belts [31]. This overall belt model does not enable to simulate specific actions of certain structures of the belt, such as the back stays, but provides an adequate simplified model for the purposes of this study.

2.1.4 Assessment of Belt Modelling

In parallel of this simulation, a clinical study was carried out on fifteen low back pain subjects [31]. The interface pressure between the belt and the trunk was measured using piezoresistive pressure mapping system of 32 × 12 sensors [32]. The mean pressure measured during the clinical study could therefore be compared to the pressure by Laplace's law.

2.2 Parametric Study

2.2.1 Input Parameters

To show how lumbar belt wearing influences mechanical conditions, a numerical design of experiments was built. Its input parameters are:

- The morphological parameters of the patient: height, corpulence and lumbar lordosis angle,
- The characteristic parameters of the lumbar belt: belt type and height,

Fig. 4 Examples of lumbar belts used in this study provided by Thasne®: (**a**) Lombacross Activity®, (**b**) LombaSkin®

- The mechanical properties of the structures composing the model: skin, abdomen, annulus, nucleus, bone and others soft tissues.

To vary the patient's morphological parameters, a basic geometry was constructed as described in Sect. 2.1. This geometry was obtained from radiographies of one patient, without 3D deformation of the spine. This geometry was proportionally modified in order to obtain two trunk's geometries: one corresponding to a person with the height of 1.60 m and one corresponding to a person with the height of 1.80 m. The basic geometry corresponded to a person with a small waist circumference. This basic geometry was therefore considered as "slim". The trunk thicknesses in the sagittal plane at the waist and hips levels were doubled in order to obtain the geometry of a "fat" person. The inclination angles of the lumbar vertebrae were modified to obtain subjects with a low lumbar lordosis of 33° or a high lumbar lordosis of 53°. Subjects with hypo- and hyperlordosis could therefore be modelled. Finally, eight characteristic geometries were obtained by varying the height (tall/small), stature (slim/large) and lumbar lordosis (hypo/hyper-lordosis).

Laplace's law modelled two types of lumbar belts. The first one has a single fabric thickness (LombaSkin®) and the other is more rigid having a posture-correcting strap (Lombacross Activity®) (Fig. 4). Each belt type has two different heights: 21 cm and 26 cm.

With linear elastic assumptions, we only need Young's moduli and Poisson's ratios to describe mechanical behavior of materials. Poisson's ratios, used in the model and taken from the literature [28, 33–35], are shown in Table 1. Only Young's moduli will vary in this parametric study. They are defined by continuous parameters, in contrast with the other parameters, and may vary within a range on the basis of the data in the literature [28, 33–35].

This parametric study therefore includes 11 input parameters (see Table 2).

Table 1 Poisson's ratio for the different components in the model

Model structure	Poisson's ratio
Abdomen	0.45
Annulus	0.45
Nucleus	0.48
Skin	0.2
Bone	0.3
Other soft tissues	0.45

Table 2 Morphology of the subjects modelled, characteristics of the belts studied and variation range for the mechanical properties of the structures for the parametric study

Parameters	−1	1
Subject's height (cm)	160	180
Subject's corpulence	Slim	Large
Subject's lordosis (°)	33	53
Belt type	LombaSkin®	Lombacross Activity®
Belt height (cm)	21	26
Young's modulus of the abdomen (MPa)	0.01	1
Young's modulus of the annulus (MPa)	4	14.9
Young's modulus of the nucleus (MPa)	3	8
Young's modulus of the skin (MPa)	1	5
Young's modulus of the bone (MPa)	1000	12,000
Young's modulus of the other soft tissues (MPa)	0.55	1

2.2.2 Output Parameters

The following three output parameters were observed:

- The variation in abdominal pressure, since it characterizes the direct impact of belts on the trunk,
- The variation in lordosis, characterized by measurement of the mean displacement of the lumbar vertebrae in the sagittal plane to determine the impact on the spine posture,
- The variation in intradiscal pressure in the lumbar spine.

2.2.3 Design of Experiments

The design method used is a stratified 100-experiment Latin hypercube design. It was taken since it makes possible to cover the entire study space with a relatively small number of experiments and at the same time, enabling binary or continuous input parameter analysis.

3 Results

3.1 Convergence Study

Figure 5 represents the variation in mean abdominal pressure as a function of the number of elements for the most slim and smallest patient with hypolordosis in the study by controlling the element size. Convergence is obtained for an element size of less than 15 mm, corresponding to a little over 80,000 elements in this case. Similar results were found for the other seven geometries modelled. The convergence study done with the eight used subject geometries finally shows that convergence is achieved for all the cases when the elements have a mean size of 10 mm. This mean size corresponds to models including 242,230–481,850 elements. It was therefore selected to perform the numerical design of experiments.

3.2 Assessment of Belt Modelling

In the clinical study, the mean pressure applied is 1.12 kPa or 2.03 kPa, respectively, for a single or double fabric thickness lumbar belt. In our model, the mean pressure applied to model by the belt is 1.06 kPa or 2.16 kPa, respectively, for a single or

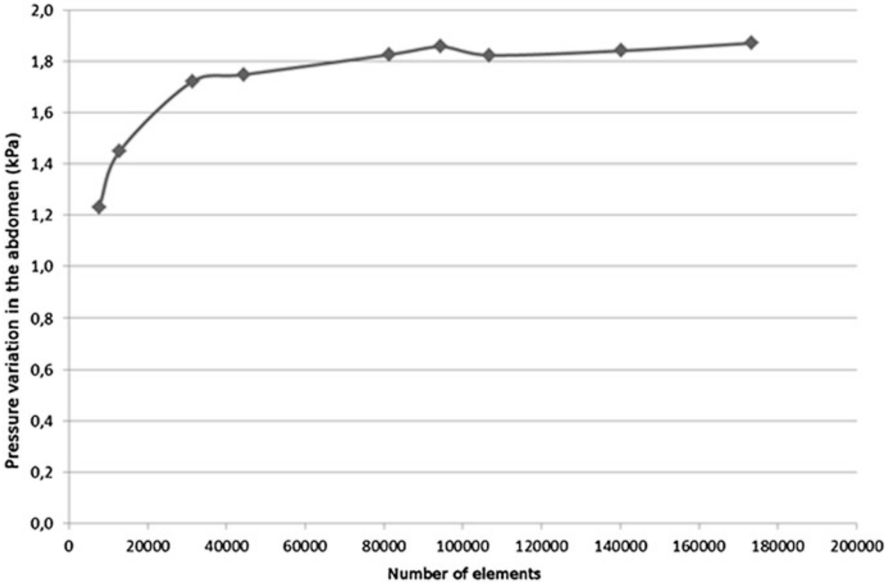

Fig. 5 Result of the convergence study: variation in mean abdominal pressure in the model as a function of the number of elements

double fabric thickness lumbar belt. The mean error is about 6% and resulting from simplified modelling of the belt by Laplace’s law. The belt model is acceptable.

3.3 Example of Detailed Results for a Modelled Subject

Figure 6 shows the pressure and displacement results for two subjects modelled in this study.

The displacements are very different between the subject’s abdomen and back. However, the displacements are symmetrical in the sagittal plane. At the iliac crests, displacements are almost zero.

The pressure inside elements is the highest at the iliac crests. This pressure is also high in the abdomen. It is negative in the lumbar region.

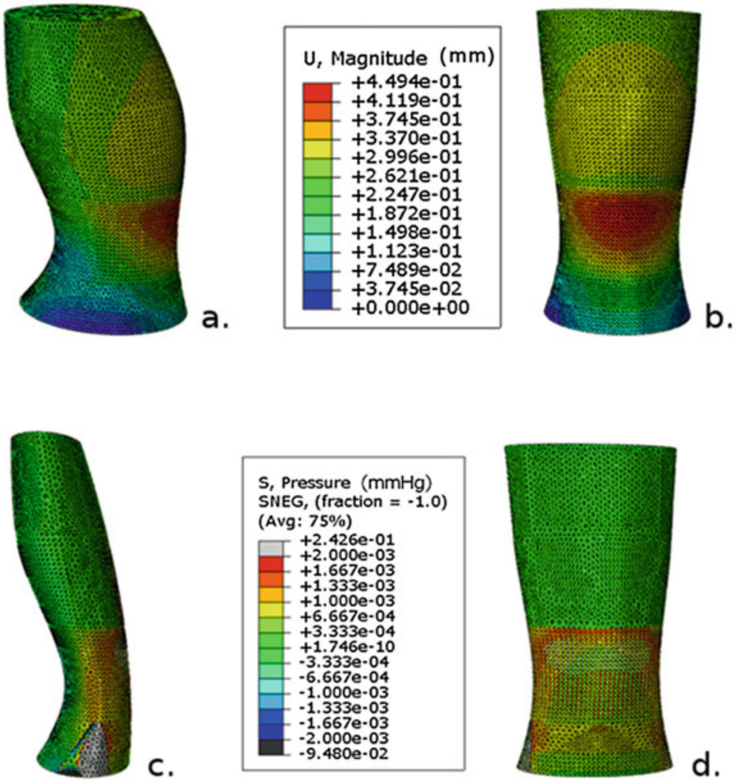

Fig. 6 Displacement result for a fat, tall subject with hyperlordosis applied by Lombacross Activity®: (**a**) in profile and (**b**) from the front, and pressure result inside element for a slim and small subject with hypolordosis: (**c**) in profile and (**d**) from the front

3.4 Parametric Study

The stratified Latin hypercube design made it possible to construct a linear model according to Eq. (2):

$$\begin{aligned} Y &= \beta_0 + \beta_s X_s + \beta_c X_c + \beta_l X_l + \beta_{\mathrm{bt}} X_{\mathrm{bt}} + \beta_h X_h + \beta_{\mathrm{pab}} X_{\mathrm{pab}} \\ &\quad + \beta_{\mathrm{pan}} X_{\mathrm{pan}} + \beta_{\mathrm{pn}} X_{\mathrm{pn}} + \beta_{\mathrm{ps}} X_{\mathrm{ps}} + \beta_{\mathrm{pb}} X_{\mathrm{pb}} + \beta_{\mathrm{ot}} X_{\mathrm{ot}} \end{aligned} \tag{2}$$

where

- $Y =$ the output variable, which may be either the variation of abdominal pressure or the variation of intradiscal pressure, or the mean displacement of the lumbar vertebrae in the sagittal plane,
- $\beta_0 =$ the mean value of the linear model,
- $\beta_i =$ the linear coefficients of the model and have an index s for the patient's height, c for the patient's corpulence, l for the patient's lordosis, bt for the belt type, h for the belt height, pab for Young's modulus of the abdomen, pan for Young's modulus of the annulus, pn for Young's modulus of the nucleus, ps for Young's modulus of the skin, pb for Young's modulus of the bone and ot for Young's modulus of the other soft tissues,
- $X =$ is the input variable with the same indices as for the β coefficients.

X is reduced in a $[-1 \; +1]$ range. The mean displacement of the vertebrae is taken to be positive when the lordosis increases. The model chosen was a linear one without interaction since the interaction parameters are weak compared to the main parameters.

Figure 7 plots the linear coefficients of the model for the variation in abdominal and intradiscal pressures and the mean displacement of the lumbar vertebrae, related to the variation in lordosis. Because of the input parameters reduction to $[-1 \; +1]$, this graphic representation of the linear model developed enables to determinate the parameters with the greatest influence. It shows that greater is the linear coefficient compared to the mean value of the output parameter, greater is the influence of the input parameter corresponding to this linear coefficient.

Hence the parameters with the greatest influence on displacement of the lumbar vertebrae are waist circumference, belt height and type, and lumbar lordosis before wearing the belt; the parameters with the least influence are the subject's height and Young's modulus of the annulus.

With respect to the variation in abdominal pressure, the parameters with the greatest influence are belt height and type as well as lumbar lordosis; the parameters with the least influence are the waist circumference and the mechanical properties of the skin and the annulus.

Finally, the parameters with the greatest influence to the variation in intradiscal pressure are the belt type, the subject's height and waist circumference, while the parameter with the least influence is Young's modulus of the skin.

A summary of the influence of input parameters on output parameters is presented in Table 3.

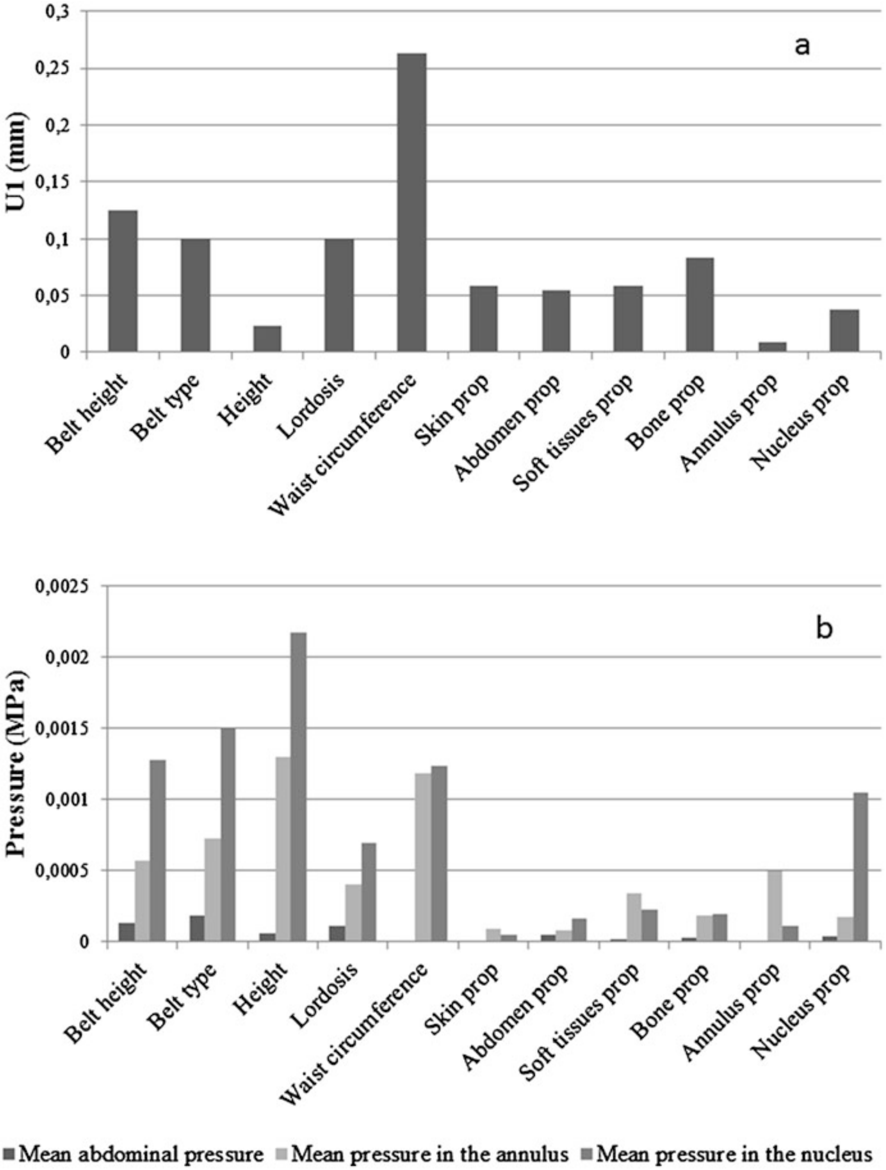

Fig. 7 Representation of the linear coefficients obtained in absolute values according to the analysis by experimental design for: (**a**) displacement of the lumbar vertebrae, (**b**) variation in abdominal and intradiscal pressures

Table 3 Influence of input parameters on output parameters

	Mean abdominal pressure	Mean intradiscal pressure	Variation in lumbar lordosis
Belt height	++	+	+
Belt type	++	++	+
Subject’s height	+	++	+
Lumbar lordosis	++	+	+
Subject’s waist circumference	−−	++	++
Mechanical properties of the skin	−−	−−	−
Mechanical properties of the abdomen	+	−	−
Mechanical properties of the soft tissues	−	+	−
Mechanical properties of the bone	−	−	−
Mechanical properties of the annulus	−−	+	−−
Mechanical properties of the nucleus	+	+	−

4 Discussion

4.1 *Trunk Model*

The developed FE trunk model is geometrically very simple but includes numerous structures, such as the abdomen, iliac crests and spine. Its main advantage lies in the fact that it enables rapid modelling of different morphologies solely from two complete radiographies of the trunk. This model can also be adapted to only simulate part of the trunk, such as the lumbar region. Another advantage of this model is a reliable calculation time, which means that it is possible to test numerous configurations in a reasonable computing time: a few hours for one configuration on a 2-core computer.

During the construction of this model, several hypotheses were made.

Firstly, deformations were assumed to be small, making it possible to model the structures using elastic linear properties. This hypothesis is confirmed since strains less than 1% for each component make it possible to stay in the linear zone of the biomechanical structures behavior.

Secondly, in order to simplify the model and not to model the posterior parts of the vertebrae present in other models [36], it was assumed that rotation of the vertebrae in the transverse axis is small on application of the pressure representing the belt wearing. The rotation of the vertebrae observed in the model is less than 5°. This rotation is small compared to the lumbar lordosis and thoracic kyphosis of the patients prior to application of pressure. This second hypothesis is also validated therefore.

Thirdly, the initial stresses in the trunk due to gravity and the presence of the head and legs are not taken into account in the model, in contrast with other models [28, 37, 38]. This hypothesis is correct since the study only concerns the pressure variation and displacement of vertebrae due to the belt wearing and not absolute pressure or deformation values.

Fourthly, it was opted to represent the action of the lumbar belt by a pressure range obtained by Laplace's law, as has already been proposed for compression socks in another study [30]. The mean pressures applied by lumbar belts obtained in a clinical study in fifteen subjects with low back pain [31] demonstrate that this simplistic model is acceptable. The difference in the interface pressure applied by the lumbar belt between simulation and clinical measurement is only 6%.

In the context of our study, the hypotheses adopted are therefore all justified. In addition, the clinical study demonstrates that the variation in trunk volume measured in humans during wear of a lumbar belt is almost identical to the variation in volume obtained in this model. This proves that, for an overall study of the mechanism of action of lumbar belts, our model is valid.

4.2 Mechanism of Action of a Lumbar Belt

Observation of the pressure and displacement variations on a patient can explain some mechanisms of therapeutic action of lumbar belts. The belt applies pressure on the skin, and greatly increases abdominal pressure. This increase leads to a slight change in lordosis and to reduce constraints on vertebrae and intervertebral structures. The variation in intradiscal pressure is low, at around 1%. This low-pressure variation is close to pressure variation obtained in other studies on rigid orthotics [39].

Pressure is the highest in the iliac crests. It can be explained by the fact that the iliac crests are highly rigid structures compared to the soft tissues of the trunk. High pressure is linked to the feeling of well-being. If the pressure applied by the belt is too high, the patient will find it more difficult to accept his/her belt [40].

The parametric study made it possible to determine some parameters influencing the variation in abdominal and intradiscal pressure and displacement of the lumbar vertebrae, related to the modification in lumbar lordosis, which can play an important role in pain relief. These three output parameters are complementary to contribute to the therapeutic effects of lumbar belts in the treatment of low back pain.

Finally, the results of this parametric study raise the following points with respect to the clinical use of lumbar belts in the treatment of low back pain:

- The choice of belt is very important;
- It is necessary to take into account the patient's morphology;
- The belt treatment is independent of mechanical properties of soft tissue, excluding the mechanical properties of intervertebral discs.

As a matter of fact, all the effects of a lumbar belt cannot be described by the model. In particular, pressure induces proprioceptive effects on the body and an active change in the posture. This approach only shows a passive effect of the belt on the trunk.

5 Conclusion

Using a simplified model of the human trunk obtained on the basis of two radiographies, a parametric study made it possible to determine some parameters influencing the efficiency of lumbar belt in the therapeutic treatment of low back pain. These parameters are the patient's morphology and the type of lumbar belt.

The numerical model used is a simple one. It can serve as a basis for more in-depth studies concerning the analysis of efficiency of lumbar belts in low back pain. In order to study the impact of the belt's architecture, modelling of the pressure applied to the trunk using Laplace's law could be improved. For example, the linear tension used in Laplace's law could vary depending on the application zone. This linear tension could be higher at the dorsal part of the trunk, to reflect the presence of the back whales. For a more precise solution, it would be possible to model the belt using a volume structure including the different existing parts, i.e. the fabrics, the back and front whales, etc. This numerical model could also be used as the basis for a study of the impact of the belt over a period of wearing time. Indeed, the clinical study shows that movement has an important impact on the distribution of pressure applied by the belt. This dynamic study would require modelling of the back muscles using volumetric structures with specific dynamic characteristics or beams.

References

1. Stucki RF, Waldburger M (2001) Approche multidisciplinaire de la lombalgie commune subaiguë et chronique: expérience suisse romande. Rev Rhum 68(2):178–184
2. Calmels P, Queneau P, Hamonet C et al (2009) Effectiveness of a lumbar belt in subacute low back pain: an open, multicentric, and randomized clinical study. Spine 34(3):215–220
3. Axelsson P, Johnsson R, Strömqvist B (1992) Effect of lumbar orthosis on intervertebral mobility. A roentgen stereophotogrammetric analysis. Spine 17(6):678–681
4. Calmels P, Fayolle-Minon I (1996) An update on orthotic devices for the lumbar spine based on a review of the literature. Rev Rhum 63(4):285–291
5. Fidler MW, Plasmans CM (1983) The effect of four types of support on the segmental mobility of the lumbosacral spine. J Bone Joint Surg 65(7):943–947
6. Andersson BJ, Ortengren R (1974) Lumbar disc pressure and myoelectric back muscle activity during sitting. 3. Studies on a wheelchair. Scand J Rehabil Med 6(3):122–127
7. McGill SM, Norman RW, Sharratt MT (1990) The effect of an abdominal belt on trunk muscle activity and intra-abdominal pressure during squat lifts. Ergonomics 33(2):147–160

8. Nachemson A, Morris JM (1964) In vivo measurements of intradiscal pressure. J Bone Joint Surg 46(5):1077–1092
9. Cholewicki J, Shah KR, McGill KC (2006) The effects of a 3-week use of lumbosacral orthoses on proprioception in the lumbar spine. J Orthop Sports Phys Ther 36(4):225–231
10. Dalichau S, Scheele K (2000) Auswirkungen elastischer lumbal-stützgurte auf den effect eines muskeltrainingsprogrammes für patienten mit chronischen rückenschmerzen. Z Orthop 138(1):8–16
11. Thoumie P, Drape JL, Aymard C et al (1998) Effects of a lumbar support on spine posture and motion assessed by electrogoniometer and continuous recording. Clin Biomech 13(1):18–26
12. Fayolle-Minon I, Calmels P (2008) Effect of wearing a lumbar orthosis on trunk muscles: study of the muscle strength after 21days of use on healthy subjects. Joint Bone Spine 75(1):58–63
13. Kawaguchi Y, Gejo R, Kanamori M et al (2002) Quantitative analysis of the effect of lumbar orthosis on trunk muscle strength and muscle activity in normal subjects. J Orthop Sci 7(4):483–489
14. Reyna JR, Leggett SH, Kenney K et al (1995) The effect of lumbar belts on isolated lumbar muscle. Strength and dynamic capacity. Spine 20(1):68–73
15. Warren LP, Appling S, Oladehin A, Griffin J et al (2001) Effect of soft lumbar support belt on abdominal oblique muscle activity in nonimpaired adults during squat lifting. J Orthop Sports Phys Ther 31(6):316–323
16. Holmström E, Moritz U (1992) Effects of lumbar belts on trunk muscle strength and endurance: a follow-up study of construction workers. J Spinal Disord 5(3):260–266
17. Million R, Nilsen KH, Jayson MI et al (1981) Evaluation of low back pain and assessment of lumbar corsets with and without back supports. Ann Rheum Dis 40(5):449–454
18. Valle-Jones JC, Walsh H, O'Hara J et al (1992) Controlled trial of a back support ('Lumbotrain') in patients with non-specific low back pain. Curr Med Res Opin 12(9):604–613
19. Willner S (1985) Effect of a rigid brace on back pain. Acta Orthop Scand 56(1):40–42
20. Carrier J, Aubin CE, Villemure I, Labelle H et al (2004) Biomechanical modelling of growth modulation following rib shortening or lengthening in adolescent idiopathic scoliosis. Med Biol Eng Comput 42(4):541–548
21. Nagasao T, Noguchi M, Miyamoto J et al (2010) Dynamic effects of the Nuss procedure on the spine in asymmetric pectus excavatum. J Thorac Cardiovasc Surg 140(6):1294–1299
22. Pankoke S, Hofmann J, Wölfel HP (2001) Determination of vibration-related spinal loads by numerical simulation. Clin Biomech 16:S45–S56
23. Huynh AM, Aubin CE, Mathieu PA et al (2007) Simulation of progressive spinal deformities in Duchenne muscular dystrophy using a biomechanical model integrating muscles and vertebral growth modulation. Clin Biomech 22(4):392–399
24. Lafortune P, Aubin CE, Boulanger H et al (2007) Biomechanical simulations of the scoliotic deformation process in the pinealectomized chicken: a preliminary study. Scoliosis 2(1):16
25. Villemure I, Aubin CE, Dansereau J et al (2004) Biomechanical simulations of the spine deformation process in adolescent idiopathic scoliosis from different pathogenesis hypotheses. Eur Spine J 13(1):83–90
26. Arjmand N, Plamondon A, Shirazi-Adl A et al (2012) Predictive equations for lumbar spine loads in load-dependent asymmetric one-and two-handed lifting activities. Clin Biomech 27(6):537–544
27. Bazrgari B, Nussbaum MA, Madigan ML et al (2011) Soft tissue wobbling affects trunk dynamic response in sudden perturbations. J Biomech 44(3):547–551
28. Clin J, Aubin CE, Labelle H (2007) Virtual prototyping of a brace design for the correction of scoliotic deformities. Med Biol Eng Comput 45(5):467–473
29. Chagnon A, Aubin CE, Villemure I (2010) Biomechanical influence of disk properties on the load transfer of healthy and degenerated disks using a poroelastic finite element model. J Biomech Eng 132:111006. https://doi.org/10.1115/1.4002550
30. Dubuis L, Avril S, Debayle J et al (2012) Patient-specific numerical model of soft tissues in the compressed leg: application to six subjects. Comput Methods Biomech Biomed Engin 15(S1):44–45

31. Bonnaire R (2015) Caractérisation mécanique des orthèses: application aux ceintures de soutien lombaire dans le cadre de la lombalgie. PhD Thesis, Ecole des Mines de Saint-Etienne, France
32. Bonnaire R, Verhaeghe M, Molimard J et al (2014) Characterization of a pressure measuring system for the evaluation of medical devices. J Eng Med 228:1264–1274
33. Goel VK, Kong W, Han JS et al (1993) A combined finite element and optimization investigation of lumbar spine mechanics with and without muscles. Spine 18(11):1531–1541
34. Périé D, Aubin CE, Lacroix M et al (2004) Biomechanical modelling of orthotic treatment of the scoliotic spine including a detailed representation of the brace-torso interface. Med Biol Eng Comput 42(3):339–344
35. Sylvestre PL, Villemure I, Aubin CE (2007) Finite element modeling of the growth plate in a detailed spine model. Med Biol Eng Comput 45(10):977–988
36. Wagnac E, Arnoux PJ, Garo A et al (2012) Finite element analysis of the influence of loading rate on a model of the full lumbar spine under dynamic loading conditions. Med Biol Eng Comput 50(9):903–915
37. Dreischarf M, Rohlmann A, Bergmann G et al (2011) Optimised loads for the simulation of axial rotation in the lumbar spine. J Biomech 44(12):2323–2327
38. Dreischarf M, Rohlmann A, Bergmann G et al (2010) A non-optimized follower load path may cause considerable intervertebral rotations. J Biomech 43(13):2625–2628
39. Munoz F (2014) Évaluation biomécanique des orthèses lombaires - application à l'orthèse Lordactiv®. PhD Thesis, Univ Jean Monnet, France
40. Pierrat B, Molimard J, Navarro L et al (2015) Evaluation of the mechanical efficiency of knee braces based on computational modelling. Comput Methods Biomech Biomed Engin 18(6):646–661

Quantitative Validation of MRI-Based Motion Estimation for Brain Impact Biomechanics

Arnold D. Gomez, Andrew K. Knutsen, Dzung L. Pham, Philip V. Bayly, and Jerry L. Prince

Abstract Head impact can cause traumatic brain injury (TBI) through axonal overstretch or subsequent inflammation and understanding the biomechanics of the impact event is useful for TBI prevention research. Tagged magnetic resonance imaging (MRI) acquired during a mild-acceleration impact has enabled measurement and visualization of brain deformation in vivo. However, measurements using MRI are subject to error, and having independent validation while imaging in vivo is very difficult. Thus, characterizing the accuracy of these measurements needs to be done in a separate experiment using a phantom where a gold standard is available. This study describes a method for error quantification using a calibration phantom compatible with MRI and high-speed video (the gold standard). During linear acceleration, the maximum shear strain (MSS) in the phantom ranged from 0 to 12%, which is similar to in vivo brain deformation at a similar acceleration. The mean displacement error against video was 0.3 ± 0.3 mm, and the MSS error was 1.4 ± 0.3%. To match resolutions, video data was filtered temporally using an averaging filter. Compared to the unfiltered results, resolution matching improved the agreement between MRI and video results by 15%. In conclusion, tagged MRI analysis compares well to video data provided that resolutions are matched—a finding that is also applicable when using MRI to validate simulations.

Keywords Finite strain · Tagged MRI · Brain deformation · Impact

---

A. D. Gomez (✉) · J. L. Prince
Department of Electrical and Computer Engineering, Johns Hopkins University, Baltimore, MD, USA
e-mail: adgomez@jhu.edu

A. K. Knutsen · D. L. Pham
Center for Neuroscience and Regenerative Medicine, The Henry Jackson Foundation, Bethesda, MD, USA

P. V. Bayly
Mechanical Engineering Department, Washington University in St. Louis, St. Louis, MO, USA

M. P. Nash et al. (eds.), *Computational Biomechanics for Medicine*,
https://doi.org/10.1007/978-3-030-15923-8_5

1 Introduction

Concussions and other forms of TBI involve a cascade of events that start with a head blow and can culminate in death or permanent disability [1]. Experimental observations via tagged magnetic resonance imaging (MRI) have increased our understanding on how acceleration-induced brain deformation varies as a function of acceleration type and head size [2, 3]. Experimental studies include qualitative observations on the general deformation patterns and specific quantitative analysis, such as resonant frequency calculations [4, 5]. Quantitative data is also useful to evaluate the performance of simulations, which are a key tool for the design of protective strategies [6]. Error characterization is a necessary step for effective qualitative analysis of MRI results for these applications.

Acquisition of MRI data for brain motion estimation is subject to experimental error. Typically, tagged slices are produced by successfully acquiring lines in the frequency domain (k-space), one line at a time, and motion is repeated using an MRI-compatible device. For instance, the device in Fig. 1a is designed to induce brain acceleration by a short drop. Each k-space line stems from an echo, which arises from a volume after being excited by a radiofrequency pulse [7]. The echo takes several milliseconds to appear; thus, the user has the option of acquiring an adjacent line immediately after or waiting for another motion repetition and acquiring at a similar moment in the cycle [7, 8]. This presents a problem: Merging temporally adjacent k-space lines into the same time frame results in reduced temporal resolution, but acquiring a single line per repetition requires numerous repeated motions (e.g., head bumps) to finalize the frame. Both of these approaches can introduce error, either by blurring data from the object at two spatial locations or by inconsistency of the repeated motion. As a compromise, a *segmented* acquisition protocol is used, where only some temporally adjacent k-space lines are merged, repeating motion as needed [8]. Acquisition effects are not always visible. However, the acquisition protocol alters quantitative results, particularly when the underlying mechanical process is relatively fast, such as a sudden acceleration during an impact.

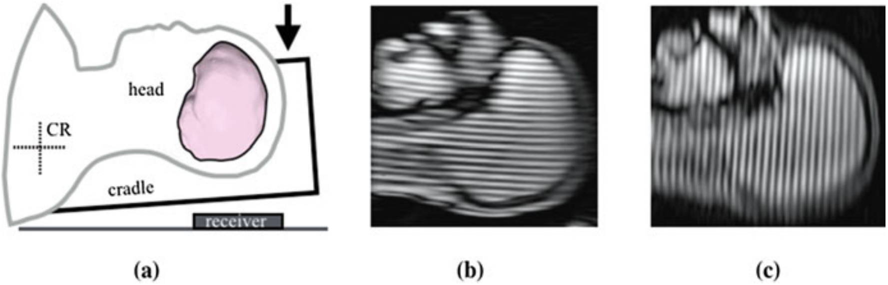

Fig. 1 Experimental measurement of acceleration-induced brain deformation. The schematic (**a**) shows the position of the head and the direction of motion (arrow). Tagged images are acquired in three orthogonal directions, two of which are shown in (**b**) and (**c**). *CR* center of rotation

Validating motion estimation in vivo is very difficult because in vivo tissue visualization is limited; thus, validation is performed as a separate experiment where a gold standard is available. Most commonly, this is accomplished with a phantom mimicking the target organ [9]. Alternatively, calibration databases with imaging and gold standard data have been useful to evaluate postprocessing approaches to extract motion information [10] (more information about strain estimation can be found in [2, 10, 11]). Unfortunately, neither of these evaluation options are available for MRI-based motion estimation during a head impact, and there is a need for data and methods to facilitate this objective.

2 Materials and Methods

The goal of this study is to characterize error in MRI-based motion estimation using high-speed video observations, and to generate data that can be used to evaluate motion estimation algorithms. Calibration was performed in a phantom compatible with both modalities, which was subjected to linear acceleration. To compare the results, we evaluated the use of an averaging filter to account for resolution differences between modalities.

2.1 Experimental Phantom

A schematic of the phantom appears in Fig. 2. The phantom's frame was cylindrical, roughly 185 mm in diameter and 50 mm in depth, and was constructed from a U.S. standard-wall schedule 40 6-in. straight fitting (part 4880K131, McMaster-Carr, Elmhurst, IL, USA). A semi-rectangular silicone slab was attached to the internal walls of the frame. The phantom was created using a 1:10 mixture of Sylgard 184 and 527 (Dow Corning, Bay City, MI, USA). Each of these silicone elastomers has two parts, which were mixed according to the manufacturer's instructions prior to being combined. This strategy enabled tuning the relative stiffness of the material while maintaining a solid consistency [12]. (It is also possible to tune stiffness by varying the mix between resin and hardener parts, but this is not recommended, because incomplete mixtures are biphasic and unstable.) The silicone slab was 150 × 100 × 50 mm and 750 cc in volume. Given the mixture of Sylgard types, the Young's modulus of the slab was roughly 10 kPa [12].

To control the silicone slab's motion, two transparent covers were added on each circular face of the cylinder. The clearance between the covers and the slab was filled with interleaved bead patterns, which served a dual purpose: First, the nylon beads constrain motion in one direction (i.e., the z-direction in Fig. 2). Second, because the phantom was optically clear, the beads were used to track motion along the unconstrained directions, i.e., the beads' motion was assumed to be the same as the phantom's surface in contact with them. Beads also allowed airflow between

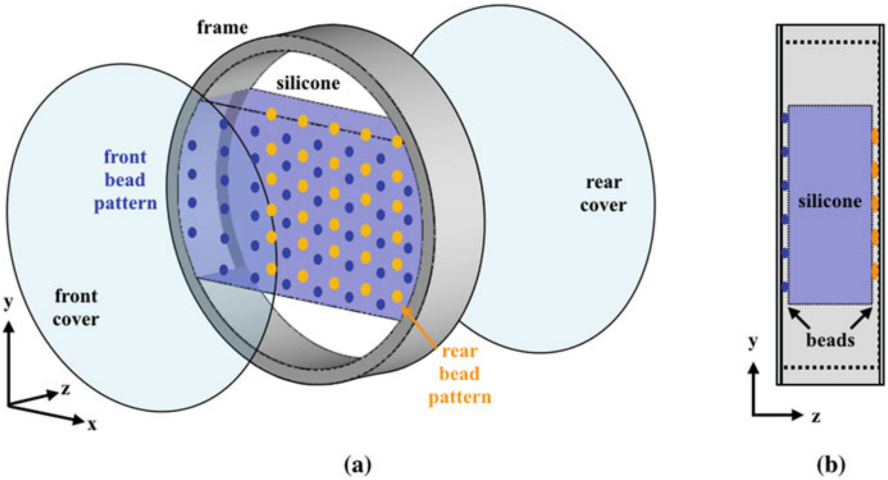

Fig. 2 Schematic of experimental motion phantom. The exploded view (**a**) shows the covers on each size, which are used to constrain the motion of the silicone slab. The cross-sectional view (**b**) indicates the locations of each landmark bead pattern

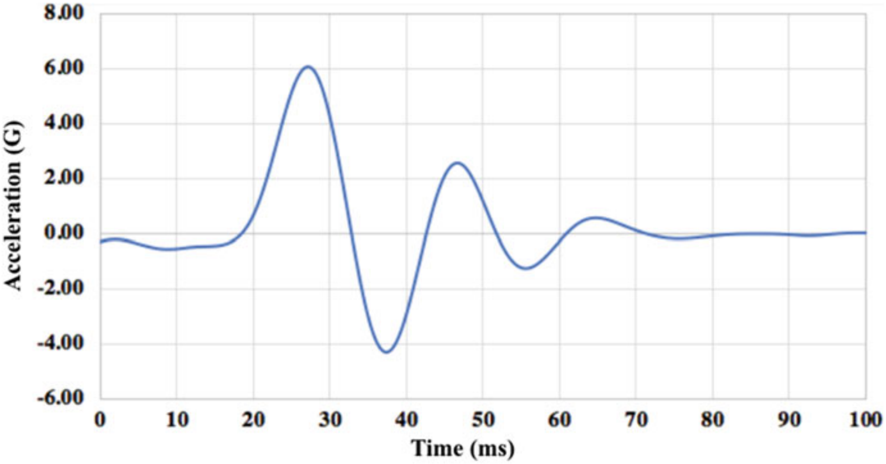

Fig. 3 Acceleration pulse. The approximate acceleration of the phantom's frame was derived from the rotation of the device's cradle (Fig. 1) measured using a rotational encoder

the chambers above and below the silicone slab so that motion was not impeded by air pressurization. For the imaging experiments, the phantom was mounted on the device described in Fig. 1, and the imaging plane was equivalent to an axial slice near the brain. The inertial load consisted of a 3 cm drop, which produced a linear acceleration pulse of roughly 40 ms with a peak of about 6 G as shown in Fig. 3 (1 G = 9.81 m/s^2).

2.2 Image Acquisition and Motion Estimation

Optical imaging was acquired at 240 frames/s using a camera (Hero 4, Gopro, San Mateo, CA, USA). Several calibration images were acquired prior to filming. All images were converted into 16-bit grayscale. The sequence resulted in 100 images, which were processes to correct barrel distortion and to determine plane depth [13]. Landmark tracking was performed via cross-correlation with a subpixel resolution algorithm [14, 15] implemented via a custom MATLAB script (2018a, MathWorks, Natick, MA, USA). The patch containing the landmark was a square of 6 pixels per side, and the search radius was 14 pixels. The initial location of each landmark bead was identified manually in 6 reference frames (1, 20, 40, 60, 80, and 100), and tracking was performed using each of these references. The tracking results were averaged to produce a tracking sequence, and the standard deviation was assumed to approximate the variance of the measurement (error propagation via Taylor's expansion [16]). This study focused on planar motion, using the front bead pattern, where beads formed a grid with a 12 mm separation.

Anatomical MRI consisted of a T1-weighted volume with 1 mm isotropic resolution. Tagged MRI for motion estimation included 4 axial slices (i.e., the x–y plane in Fig. 2) and 8 transverse slices (i.e., x–z plane). We used a Siemens Biograph mMR 3T instrument. Each slice was a 30×160 matrix (resampled to 160×160) with $TE = 1.32$ ms, and $TR = 2.7$ ms. Six temporally adjacent phase encode lines were acquired during each motion repetition; thus, to construct a slice, 5 motion repeats were necessary, resulting in a frame rate of 16.2 ms. The tag frequency was 8 mm. Motion estimation was performed in 4D (volume and time) using harmonic phase analysis with finite elements (HARP-FE) [11]. We constructed a finite-element mesh of the phantom based on the T1-weighted image (9,000 hexahedral elements). The mesh included a frame, which was set to be rigid. The slab was modeled as a Neo-Hookean solid with $C_1 = 1.0$ kPa and bulk modulus of 100 kPa to enforce incompressibility. The images were filtered using a high-pass Fourier filter set at half of the tagging frequency [17]. The HARP-FE tracking penalty was set at 800 mN/rad with an augmented Lagrangian termination of 0.3.

For comparison, the video landmarks were registered to the tagged MRI coordinates using manual registration (zoom, rotation, and displacement) since both modalities preserve aspect ratios. Time shifting (or temporal alignment) was needed to account for MRI trigger delay during slice excitation and was done semi-automatically by finding the delay that minimized the difference in displacement magnitudes. In order to match spatial resolutions, we projected the 3D MRI-based displacements into the 2D landmark locations via isoperimetric interpolation. That is, the spatial resolution of the MRI result was lowered to match the resolution of the video landmarks. We also filtered and resampled video displacements by averaging temporally adjacent results to match the MRI frame rate. Different averaging windows were tested to approximate the merging of k-space lines onto a single frame. Finally, strains and displacements were compared. Strains were calculated using triangular elements based on the landmarks using the last frame as the reference (to minimize any rigid motion effects), and evaluated via the local maximum shear strain (MSS), which is defined as

$$\mathrm{MSS} = E_1 - E_3,$$

where E_1 and E_3 represent the first and third eigenvalue of the Green-Lagrange strain tensor [18]. Comparison was based on the root mean squared (RMS) error, using t-tests (significance level, $p = 0.05$).

3 Results and Discussion

3.1 Displacement Calibration

Typical imaging results appear in Fig. 4. As expected, deformation occurred primarily along the direction of motion (the vertical direction or y-direction in Fig. 2), particularly near the center of the silicone slab. Movement was highly

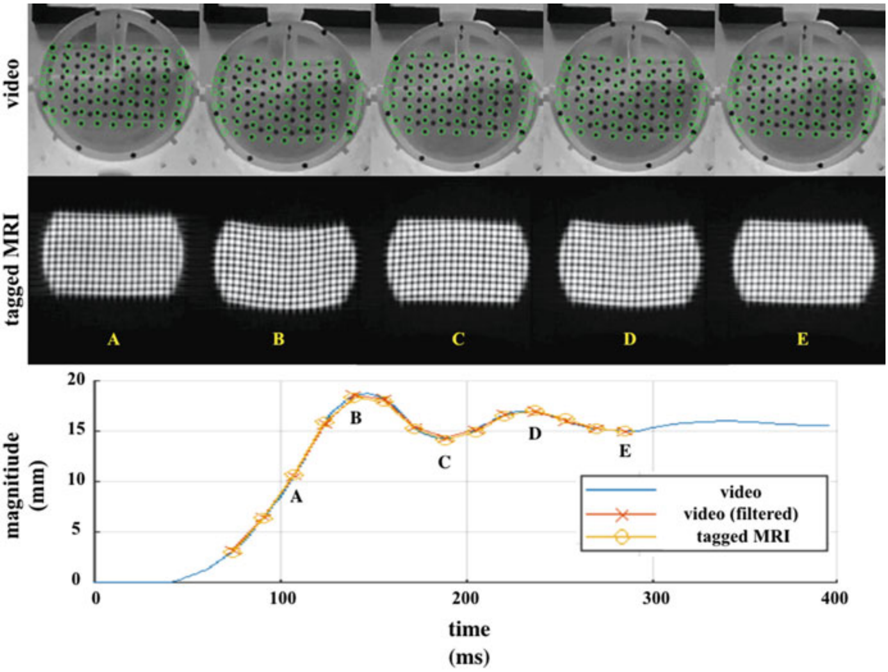

Fig. 4 Imaging results. Video (top) includes circular makers around beads (green circles). MRI (middle) shows two combined tagging directions. Mean displacement magnitudes (bottom) traces are all similar

Table 1 Discrepancy between tagged MRI and video results with respect to temporal filter size

Averaging filter size (frames)	Displacement RMS (mm)	MSS RMS (%)
No filter	0.33 ± 0.3	1.35 ± 0.29
3	0.32 ± 0.3	1.20 ± 0.30
5	0.32 ± 0.3	1.04 ± 0.34*
7	0.36 ± 0.3	0.98 ± 0.42*
9	0.46 ± 0.4	0.99 ± 0.50

The asterisk denotes significant differences with respect to unfiltered result using p=0.05

transient and showed damped oscillation, which was expected given the viscoelastic nature of silicone gel. While calculating the frequency and dampening factors of the phantom was not the objective of the study, note that the brain also shows damped resonant behavior [4].

After temporal alignment, which placed the first frame of the MRI sequence at 72 ms after the video sequence, both motion patterns were similar per visual inspection. The initial time frame in the MRI data shows that some displacement from the motionless starting position (approximately 3 mm) took place during slice excitation for imaging. Comparison between the displacement magnitudes from tagged MRI (via HARP-FE) and video results shows no obvious differences (Fig. 4). However, differences between MRI and the video results are visible when the averaging filtering is included, but these differences were not statistically significant when comparing between averaging windows ranging from 3 to 9 temporally adjacent frames, as shown in Table 1.

3.2 *Strain Calibration*

Strain maps (in Fig. 5) show spatial heterogeneity ranging between 0 and approximately 12%. Similar MSS levels have been measured in in vivo experiments in the human brain at comparable accelerations [2, 3]. MSS results also show transient behavior, which suggests some damping.

Differences across all time points indicate that averaging reduces displacement and MSS differences. Statistically significant residual RMS between unfiltered and filtered video data appears when averaging five and seven temporally adjacent video frames (Table 1). In this best-case scenario, the results have a mean displacement error between 0.32 and 0.36 mm, and MSS error between 0.98 and 1.04%. Figure 4 shows displacement results averaged with a window of 5 frames. MSS maps comparison appears in Fig. 4. The unfiltered video results tend to indicate larger strains with respect to the MRI-based solution, including values over 11% near the center of the slab at time 140 ms (i.e., the frame indicated as “B” in Fig. 4). Filtered results match MRI results more closely than unfiltered results, and the similarities are particularly apparent in the latter frames, i.e., after 156 ms. The result during

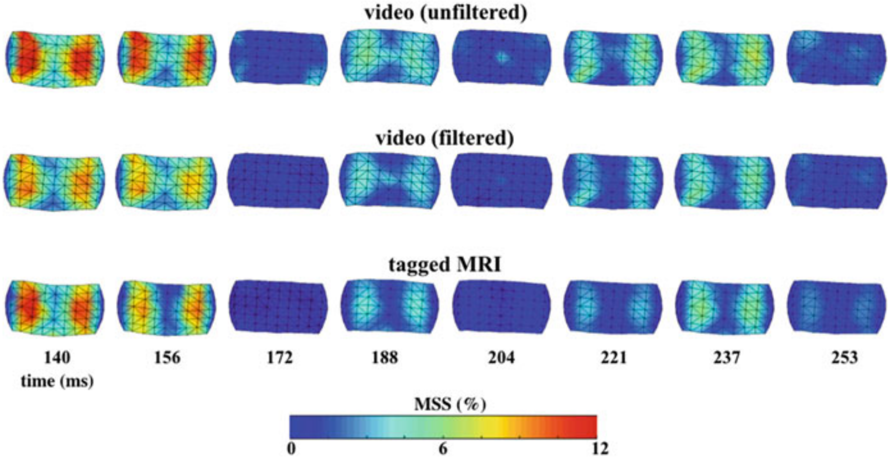

Fig. 5 Strain map comparison. The filtered results shown were achieved with a temporal averaging window of 5 frames. The imaging results in Fig. 3 can be matched as follows: B = 140 ms, C = 188 ms, D = 237 ms (A and E are not shown in the sequence above)

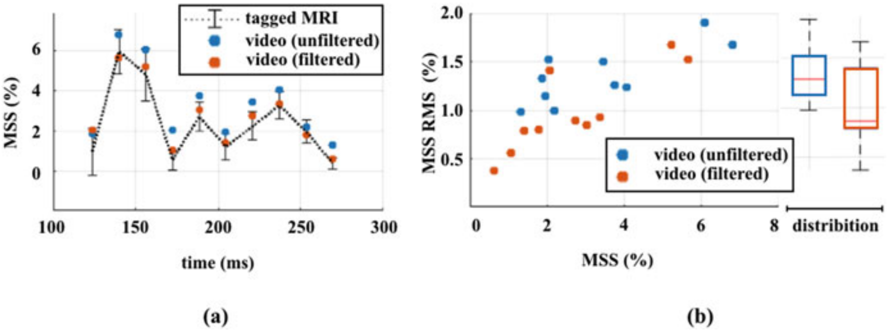

Fig. 6 Mean strain values. In the time sequence (**a**) the bars for tagged MRI results were based on the RMS values against video. The spread of each video value was omitted for clarity. The scattered plot (**b**) indicates RMS differences with respect to the level of strain per MSS

maximum deformation (140 ms) tends to appear more "washed out" (i.e., the peak values are lower) in the filtered video results.

Spatially averaged MSS values, shown in Fig. 6a, also show the transient nature of the deformation of the viscoelastic phantom due to a short drop. However, a damped decay pattern was not observed in the same way as the displacements in Fig. 4. This is likely because strains were calculated using the last MRI frame as the reference to reduce rigid motion effects. Some downward deflection (at the reference, which is marked as "E" in Fig. 4) would magnify deflection in the opposite direction, resulting in different apparent strain. However, consistent with visual inspection of Fig. 5, the mean MSS of filtered video results is closer to the tagged MRI results than the unfiltered values. In fact, comparing the average MSS at different time points and the corresponding RMS errors shows that the filtered results produce lower RMS across all time points. The difference was statistically significant ($p = 0.03$). There was no statistical difference between the MRI-based and filtered video strain results.

Combining all RMS results (Fig. 6b), it is possible to observe that, in general, the MSS RMS is proportional to MSS, and comparison between these values suggests that overall error ranges between 30% (at values above 4% MSS) and 40% (for values below 4%). This would mean that a measurement of, say, 10% MSS via MRI could be roughly interpreted as 10 ± 3% MSS; however, as shown in Fig. 5, the tagged-MRI solution has the tendency of underestimating strain. Note that the video tracking results apply to the surface of the silicone slab, while the tagged MRI measurements are only inside the material; thus, 3D MSS value ranges may vary substantially compared to the 2D results presented here.

The broader significance of these experiments in terms of generalization is subject to further investigation. Additional study will allow accounting for different resolutions and including motion inconsistency (not addressed in this study). Likewise, our experiment only used results via HARP-FE, and we did not use the phantom to optimize imaging or tracking parameters to improve accuracy. Further, we report that displacement results are more accurate than strain results, which is likely due to the gradient operator in strain calculation from displacements [18], magnifying the effects of displacement noise. This too warrants further investigation, because it affects both MRI and video results (notice that the error bars in Fig. 6a result from variability in video displacements via tracking from reference frames). Thus, the contribution of this study was providing the means to quantify error as a function of practical considerations (including imaging acquisition, displacement tracking, and strain calculation), particularly because available evaluation data generally include displacements [10] or strains [19], but databases including both are few—and virtually nonexistent for impact experiments.

This study describes a conservative approach to resolution matching. Displacement results were obtained using separate modalities: the first (MRI) has relatively high in-plane spatial resolution but poor temporal resolution, and the second (video) features the opposite. MRI features 1.5 mm in-plane resolution and 8-mm tag spacing, which are high compared to the video landmarks placed roughly 12 mm apart. Thus, we choose to convect displacement information from the higher resolution to the lower resolution prior to strain calculation. Likewise, video results were temporally averaged to account for the segmented MRI acquisition process. This process is nonlinear, and averaging is perhaps and overly simplified model for it, as the slight disagreement in Fig. 5 may attest. However, resolution matching is necessary to make an adequate comparison (and to reduce noise). Note that the best averaging window (5 frames) was also the closest to the number of video frames at 4 ms that are acquired in an interval of 16.2 ms, which is the effective temporal resolution of MRI measurements. The described process is conservative because as a consequence of resolution matching, strain information was sparse spatially and temporally. In the future, the opposite may be true, and MRI results could be processed to mitigate the effects of the segmented acquisition protocol.

Similar ideas to those discussed here also apply when comparing simulated results to tagged MRI. Simulation resolution calculation follows a fundamentally different thought process to that in imaging, but its limits are essentially arbitrary. Imaging does not enjoy limitless resolution. MRI results should also account for slice thickness in full 3D comparisons, which are also an area of future research (as additional considerations can be made by including both sets of beads in the phantom). We have also shown that, while the video experiment is able to capture the phantom from a stationary state, the first frame of the MRI measurement occurs after the application of a tagging pulse of roughly 10 ms. As the magnetic resonance signal fades in time, a completely deformation-free state may not be available within the MRI-based results unless a motion-free reference acquisition is added to the protocol. Thus, interpretation of strain is subject to both the accuracy of the measurement and the possibility of motion in the available MRI frames; hence, validation of simulated results should also account for differences in reference frame between experimental and simulated data.

4 Conclusion

This paper discusses MRI-based strain measurement calibration for studying brain motion during head impact. The study contributes the design of a quantitative phantom for evaluation against high-speed video, new data for evaluation of motion estimation methodology, and a description of calibration considering the imaging acquisition process. We show that excitation delay, segmented acquisition, and strain reference alter displacement and strain results, but resolution matching and informed interpretation of results enables adequate comparison across modalities. In summary, the comparison process should include: (1) spatiotemporal registration between domains, (2) filtering the source of strain to match resolutions, and (3) a consistent strain reference. Future research includes measurement optimization and evaluation of 3D data. Calibration images are available at iacl.jhu.edu/impactdata.

Acknowledgments This research was funded by NIH Grants R01-NS055951 and R01-DC014717, and support by the U.S. Department of Defense in the Center for Neuroscience and Regenerative Medicine.

References

1. Langlois JA, Rutland-Brown W, Wald MM (2006) The epidemiology and impact of traumatic brain injury: a brief overview. J Head Trauma Rehabil 21:375–378

2. Feng Y, Abney TM, Okamoto RJ, Pless RB, Genin GM, Bayly PV (2010) Relative brain displacement and deformation during constrained mild frontal head impact. J R Soc Interface 7:1677–1688
3. Abney TM, Feng Y, Pless R, Okamoto RJ, Genin GM, Bayly PV (2011) Principal component analysis of dynamic relative displacement fields estimated from MR images. PLoS One 6:e22063
4. Laksari K, Wu LC, Kurt M, Kuo C, Camarillo DC (2015) Resonance of human brain under head acceleration. J R Soc Interface 12:20150331
5. Bayly PV, Clayton EH, Genin GM (2012) Quantitative imaging methods for the development and validation of brain biomechanics models. Annu Rev Biomed Eng 14:369–396
6. Goriely A, Geers MGD, Holzapfel GA, Jayamohan J, Jérusalem A, Sivaloganathan S, Squier W, van Dommelen JAW, Waters S, Kuhl E (2015) Mechanics of the brain: perspectives, challenges, and opportunities. Biomech Model Mechanobiol 14:931–965
7. Haacke EM, Brown RW, Thompson MR, Venkatesan R (1999) Magnetic resonance imaging: physical principles and sequence design. Wiley-Liss, New York
8. Knutsen AK, Magrath E, McEntee JE, Xing F, Prince JL, Bayly PV, Butman JA, Pham DL (2014) Improved measurement of brain deformation during mild head acceleration using a novel tagged MRI sequence. J Biomech 47:3475–3481
9. Fortune S, Jansen MA, Anderson T, Gray GA, Schneider JE, Hoskins PR, Marshall I (2012) Development and characterization of rodent cardiac phantoms: comparison with in vivo cardiac imaging. Magn Reson Imaging 30:1186–1191
10. Tobon-Gomez C, De Craene M, McLeod K, Tautz L, Shi W, Hennemuth A, Prakosa A, Wang H, Carr-White G, Kapetanakis S, Lutz A, Rasche V, Schaeffter T, Butakoff C, Friman O, Mansi T, Sermesant M, Zhuang X, Ourselin S, Peitgen HO, Pennec X, Razavi R, Rueckert D, Frangi AF, Rhode KS (2013) Benchmarking framework for myocardial tracking and deformation algorithms: an open access database. Med Image Anal 17:632–648
11. Gomez AD, Xing F, Chan D, Pham D, Prince J (2017) Motion estimation with finite-element biomechanical models and tracking constraints from tagged MRI. In: Wittek A, Joldes G, Nielsen PMF, Doyle BJ, Miller K (eds) Computational biomechanics for medicine. Springer Nature, Cham, pp 81–90
12. Palchesko RN, Zhang L, Sun Y, Feinberg AW (2012) Development of polydimethylsiloxane substrates with tunable elastic modulus to study cell mechanobiology in muscle and nerve. PLoS One 7:e51499
13. Bukhari F, Dailey MN (2013) Automatic radial distortion estimation from a single image. J Math Imaging Vision 45:31–45
14. Willert CE, Gharib M (1991) Digital particle image velocimetry. Exp Fluids 10:181–193
15. Kähler CJ, Scharnowski S, Cierpka C (2012) On the resolution limit of digital particle image velocimetry. Exp Fluids 52:1629–1639
16. Venkateshan SP (2015) Mechanical measurements. Wiley, Chichester
17. Wang X, Stone M, Prince JL, Gomez AD (2018) A novel filtering approach for 3D harmonic phase analysis of tagged MRI. In: Angelini ED, Landman BA (eds) Medical imaging 2018: image processing. SPIE, p 39
18. Spencer AJM (1985) Continuum mechanics. Dover Books, Essex
19. Boyle JJ, Kume M, Wyczalkowski MA, Taber LA, Pless RB, Xia Y, Genin GM, Thomopoulos S (2014) Simple and accurate methods for quantifying deformation, disruption, and development in biological tissues. J R Soc Interface 11:20140685

Meshless Method for Simulation of Needle Insertion into Soft Tissues: Preliminary Results

Adam Wittek, George Bourantas, Grand Roman Joldes, Anton Khau, Konstantinos Mountris, Surya P. N. Singh, and Karol Miller

Abstract Needle insertion (placement) into human body organs is a frequently performed procedure in clinical practice. Its success largely depends on the accuracy with which the needle tip reaches the anatomical target. As the tissue deforms due to interactions with the needle, the target tends to change its position. One possible way to decrease the risk of missing the target can be to account for tissue deformations when planning the needle insertion. This can be achieved by employing computational biomechanics models to predict the tissue deformations.

In this study, for computing the tissue deformations due to needle insertion, we employed a meshless formulation of computational mechanics that uses a spatial discretisation in a form of a cloud of points. We used the previously verified Meshless Total Lagrangian Explicit Dynamics (MTLED) algorithm that facilitates accurate and robust prediction of soft continua/soft tissues mechanical responses under large deformations. For modelling of interactions between the needle and soft tissues, we propose a kinematic approach that directly links deformation of the tissue adjacent to the needle with the needle motion. This approach does not require any assumptions about the exact mechanisms of such interactions. Its parameters can be determined directly from observation of the tissue sample/body organ deformations during needle insertion.

A. Wittek (✉) · G. R. Joldes · K. Miller
Intelligent Systems for Medicine Laboratory, Department of Mechanical Engineering, The University of Western Australia, Perth, WA, Australia
e-mail: adam.wittek@uwa.edu.au

K. Mountris
Aragón Institute for Engineering Research, University of Zaragoza, IIS Aragón, Zaragoza, Spain

S. P. N. Singh
Robotics Design Laboratory, School of Information Technology and Electrical Engineering, The University of Queensland, Brisbane, QLD, Australia

G. Bourantas · A. Khau
Intelligent Systems for Medicine Laboratory, The University of Western Australia, Perth, WA, Australia

M. P. Nash et al. (eds.), *Computational Biomechanics for Medicine*,
https://doi.org/10.1007/978-3-030-15923-8_6

We evaluated the performance of our kinematic approach for modelling the interactions between the needle and the tissue through application in modelling of needle insertion into a cylindrical sample (diameter of 30 mm and height of 17 mm) of Sylgard 527 (by Dow Corning) silicone gel and comparing the results obtained from the model with the experimentally measured force acting on the needle. The needle insertion depth was up to 10 mm. For modelling of the constitutive responses of Sylgard 527 gel, we used the neo-Hookean hyperelastic material model with the shear modulus experimentally determined from compression of Sylgard 527 gel samples.

The general behaviour of the needle force–insertion depth relationship was correctly predicted by our framework that combines a meshless method of computational mechanics for computing the deformations and kinematic approach for modelling the interactions between the needle and soft tissues. The predicted force magnitude differed by only 25% from the experimentally observed value. These differences require further analysis. One possible explanation can be that the neo-Hookean material model we used here may not be sufficient to correctly represent Sylgard 527 gel constitutive behaviour.

Keywords Needle insertion simulation · Meshless methods · Meshless Total Lagrange Explicit Dynamics · Hyperelastic material models · Computational biomechanics

1 Introduction

Needle insertion (placement) into human body organs is a frequently performed procedure in clinical practice [1]. Examples include placement of electrodes for deep brain stimulation [2], breast lesion biopsy [3], brachytherapy, and lumbar anaesthesia. Success of these procedures largely depends on the accuracy with which the needle tip reaches the anatomical target (the area of interest). The target position before surgery can be accurately determined from high-quality preoperative medical images. However, the tissue deformation caused by interactions with the needle tends to change position of the target, which, in turn, can lead to inaccurate insertion [4]. If enough time is available, the target can be usually reached with assistance of image-guidance systems using ultrasound, computed tomography (CT) and magnetic resonance (MR) images [5, 6]. However, such systems may not be sufficient to eliminate the need for multiply insertion attempts [5]. One possible way to decrease the risk of faulty needle placement can be to account for tissue deformations (and associated surgical target motion) when planning the needle insertion procedures. This can be achieved by employing computational biomechanics models to predict the tissue deformations during needle insertion. Consequently, needle insertion simulation has been a subject of substantial research effort with finite element algorithms as a method of choice for solving the equations of continuum mechanics governing the behaviour of body organs/tissues and their interactions with the needle [7–10]. However, ensuring stable and robust solution for large local strain caused by the needle and modelling of crack/discontinuity propagation due to the organ surface puncture and tissue penetration by the needle still remains a challenge.

In this study, for computing the tissue deformations due to needle insertion, we employ a meshless formulation of computational mechanics that relies on spatial discretisation in a form of a cloud of points. We use Meshless Total Lagrangian Explicit Dynamics (MTLED) framework previously developed and verified by our research group [11, 12]. Our previous research has indicated that the MTLED framework facilitates accurate prediction of the organ (brain) deformations due to surgery [13] and ensures robust and stable solution in the presence of very large strain [11, 14] and discontinuities/cracks induced by surgical dissection [15]. For modelling of interactions between the needle and soft tissues, we propose a kinematic approach that directly links deformation of the tissue adjacent to the needle with the needle motion. Unlike many previously proposed solutions, this approach does not require any assumptions about the exact mechanisms of such interactions.

We present the preliminary results of evaluation of the performance of the proposed method for simulation of needle insertion into soft tissues by comparing the modelling and experimental results obtained when conducting indentation and needle insertion into tissue phantom (cylindrical samples of soft incompressible Sylgard 527 silicone gel by Dow Corning) that exhibits the constitutive behaviour similar to the brain tissue. We acknowledge that the biofidelity of different materials in representing the brain tissue constitutive responses is a subject of extensive research [16]. Such research is, however, not within the scope of this study.

2 Methods

2.1 Meshless Method for Simulation of Needle Insertion into Soft Tissues

2.1.1 Meshless Total Lagrangian Explicit Dynamics (MTLED) Algorithm for Computing Soft Tissue Deformations

We numerically solve the governing equations of continuum mechanics using the Meshless Total Lagrangian Explicit Dynamics (MTLED) framework that was introduced to compute deformation of soft tissues and other soft continua [11–13]. The MTLED is a Galerkin-type meshless method that uses an unstructured cloud of nodes to discretise the spatial domain (instead of elements like in finite element method) and spatial integration over the background grid of either hexahedral or tetrahedral integration cells. This way, ‘good quality’ mesh, that tends to be time consuming to build for continua with complex geometry (such as human body organs), is not needed. Placement of the nodes is automatic and their arrangement can be almost arbitrary. MTLED framework can handle large deformations and boundary changes [14, 15]. As MTLED framework uses explicit time stepping, no iterations are needed even for strongly non-linear problems. More analytical and comprehensive description of the MTLED framework is available in papers [11–15] (and the references therein).

For all models in this study, we used the MTLED framework with the Modified Moving Least Squares (MMLS) shape functions [17] and boundary-conforming tetrahedral background integration cells with one integration (Gauss) point.

2.1.2 A New Method for Modelling of Interactions Between the Needle and Soft Tissues Using Kinematic Approach

For simulation of needle insertion into soft tissues, we propose a kinematic approach that does not require knowledge about the type of interactions between the needle and the tissue as it directly links the deformation of the tissues adjacent to the needle with the needle displacement/motion. As in most surgical procedures needle is much stiffer than the organ tissue, we consider the needle as a rigid body and represent it using a set of nodes that cannot move in relation to each other. Following the experimental literature on needle insertion into soft tissues [18], two phases of needle insertion are distinguished in our kinematic approach: (1) Indentation where the organ surface deforms as a result of contact interactions with the needle tip; and (2) Tissue penetration by the needle that follows the puncture of the organ surface by the needle tip. During the insertion phase, the tissue is in contact with both the needle tip and the needle shaft.

1. *Indentation*: During the indentation, only a small area on the organ surface (analysed continuum) is in contact with the needle. We represent this area by a subset of nodes located on the organ surface. During indentation, the displacement of these nodes equals the known (predefined) needle tip displacement. We monitor strain in the needle insertion area. When the strain exceeds a threshold value (referred to as puncture strain ε_p), the needle punctures the organ surface and the penetration phase starts.
2. *Penetration*: We define the nodes located in the support domain of the needle nodes. The nodes located in this support domain are then displaced by a fraction (referred to as of the deformation coefficient C_D) of the known (predefined) displacement of the needle.

For software implementation of our method for simulation of needle insertion into soft tissues (soft continua), we used MATLAB version 2017b programming language (MathWorks, https://au.mathworks.com/).

2.2 Verification of the Proposed Meshless Method for Simulation of Needle Insertion into Soft Tissues

We follow the procedure outlined in Babuska and Oden [19] who recommend to verify new algorithms of computational mechanics against the established benchmark solutions. As the biomechanics research community has not formulated yet the benchmark solutions and established algorithms for needle insertion simulation, we conducted verification of our meshless method in the following two stages. In the first stage, we evaluated the accuracy and robustness of our meshless algorithm (MTLED) for computing soft continua deformations under large strain consistent with needle insertion. This was done by applying the MTLED framework to model the indentation of a cylindrical sample made from Sylgard 527 (Dow Corning, Midland, MI) silicone gel and comparing the forces predicted using MTLED framework with the results computed using established non-linear algorithms available in ABAQUS (version 16.14-1) finite element code (Dassault Systems, Simulia https://www.3ds.com/products-services/simulia/products/abaqus/) and the experimentally measured indentation force (Fig. 1). The rationale for selecting Sylgard 527 gel was that this gel has been previously used in numerous studies as the brain tissue substitute [20, 21]. As direct modelling of contact interactions requires calibration/tuning of the parameters of contact models, the indenter was not directly modelled. We prescribed the displacements of the nodes located on the sample surface that were in contact with the indenter face so that their displacement equalled the indenter displacement. As Sylgard 527 gel firmly stuck to the indenter face, there was no artefact related to the gel movement in relation to the indenter face (Fig. 1).

In the second verification stage, we evaluated the performance of our kinematic approach for modelling the interactions between the needle and the tissue. This was done through application of this approach in modelling of needle insertion into a cylindrical sample of Sylgard 527 gel and comparing the results obtained from the model with the experimentally measured force acting on the needle (Fig. 2).

All the experiments in this study were conducted using an in-house portable tension–compression test rig developed at the Intelligent Systems for Medicine Laboratory at The University of Western Australia [22] (see also http://isml.ecm.uwa.edu.au/ISML/) equipped with Burster 8532 EN load-cell (https://www.burster.com/) and MTS Temposonics CS H2 LVDT linear displacement sensor (http://www.mtssensors.com/) (Figs. 1, 2, and 3).

2.2.1 Determining the Parameters for Our Meshless Method for Simulation of Needle Insertion into Soft Tissues

Constitutive Model for Needle Insertion Simulation The previous research has indicated that Sylgard 527 gel exhibits non-linear stress–strain relationship that can

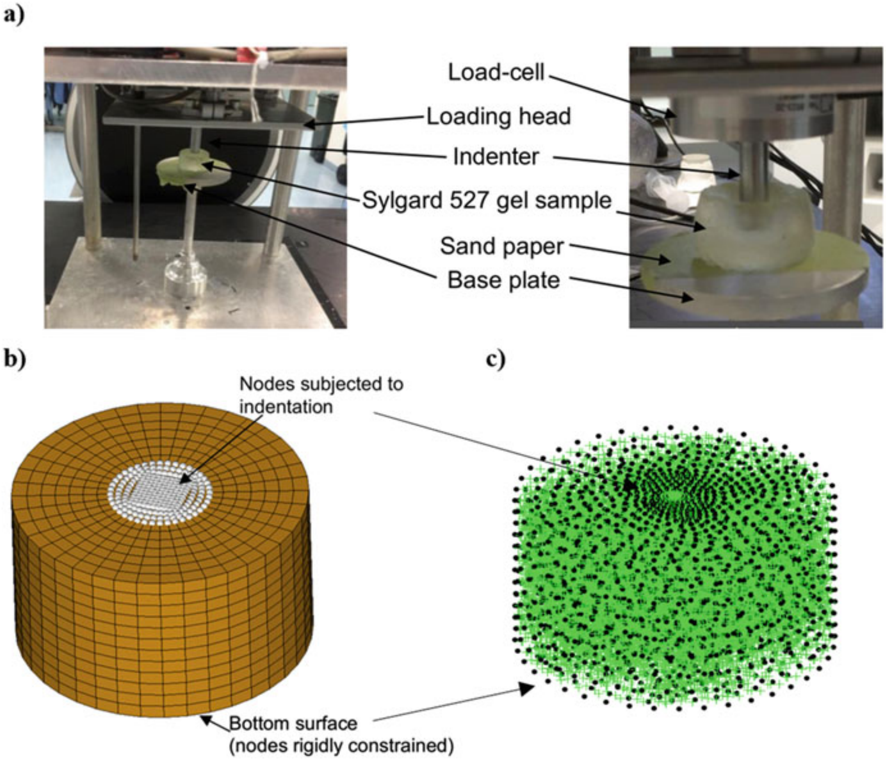

Fig. 1 (**a**) Indentation of cylindrical samples (diameter of 30 mm, height of 17 mm) of Sylgard 527 gel conducted in this study. The indenter (aluminium) diameter is 10 mm. (**b**) Finite element mesh for modelling of indentation of cylindrical samples of Sylgard 527 gel. The model was implemented using ABAQUS non-linear finite element code. The gel sample was discretised using 8223 nodes and 6000 eight-noded hexahedral elements with hybrid formulation (solid element C3D8H in ABAQUS finite element code). The hybrid formulation was used to prevent volumetric locking. (**c**) Meshless discretisation (using the MTLED algorithm) for simulation of gel sample indentation. The sample was discretised using 8233 nodes (black dots) and 44,343 background tetrahedral integration cells with one Gauss point (green crosses) per cell

be accurately represented using hyperelastic constitutive models [21]. In this study, we used the neo-Hookean model [23]:

$$W = \frac{\mu}{2}(I_1 - 3) + \frac{K}{2}(J - 3) \quad (1)$$

where W is the strain energy, μ is the shear modulus, K is the bulk modulus, I_1 is the first strain invariant of the right Cauchy Green deformation tensor, and J is the volume ratio which equals the determinant of deformation gradient.

Data regarding the Sylgard 527 shear modulus have been previously reported in the literature [16, 21]. However, as Sylgard 527 is a two-compound (part ‘A’ and ‘B’) gel, its stiffness tends to exhibit sensitivity to even small variation in proportion

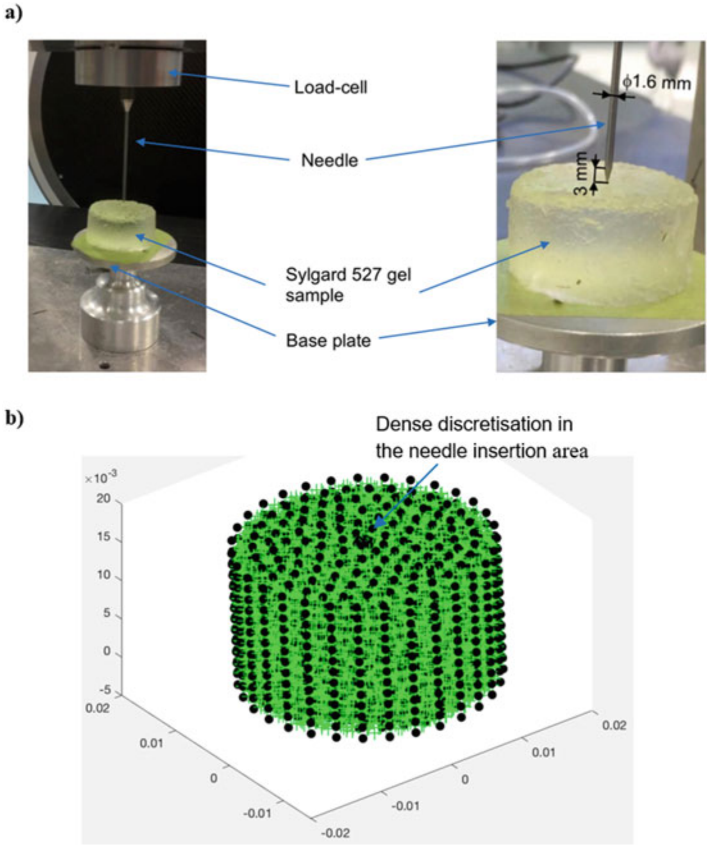

Fig. 2 (**a**) Needle insertion in the sample of Sylgard 527 gel. (**b**) Meshless discretisation (using the MTLED algorithm) for simulation of the experimental setup shown in figure (**a**). The sample was discretised using 5224 nodes (black dots) with 28,645 background tetrahedral integration cells with one Gauss point (green crosses) per cell. The coordinate frame indicates dimensions in meters

of the two compounds and curing conditions. To determine the shear modulus for the specific compound proportion (nominally 1:1 weight ratio) and curing conditions (temperature of 60 °C for 24 h) used in this study, a cylindrical gel sample (height of 17 mm and diameter of 30 mm) was subjected to compression (Fig. 1). The bottom surface of the sample was placed on sandpaper glued to the rig base, i.e. this surface was rigidly constrained (Fig. 3). As the loading plate was also covered with sandpaper, the sample's top surface was constrained in the horizontal plane and only vertical displacement was allowed. Following [21], the experiments were modelled (the model is shown in Fig. 3b) using the non-linear procedures available in ABAQUS finite element code. The shear modulus (μ in Eq. (1)) was varied to obtain the computed force–displacement relationship close to the relationship determined from the experiments [25, 26]. As Sylgard 527 is nearly incompressible,

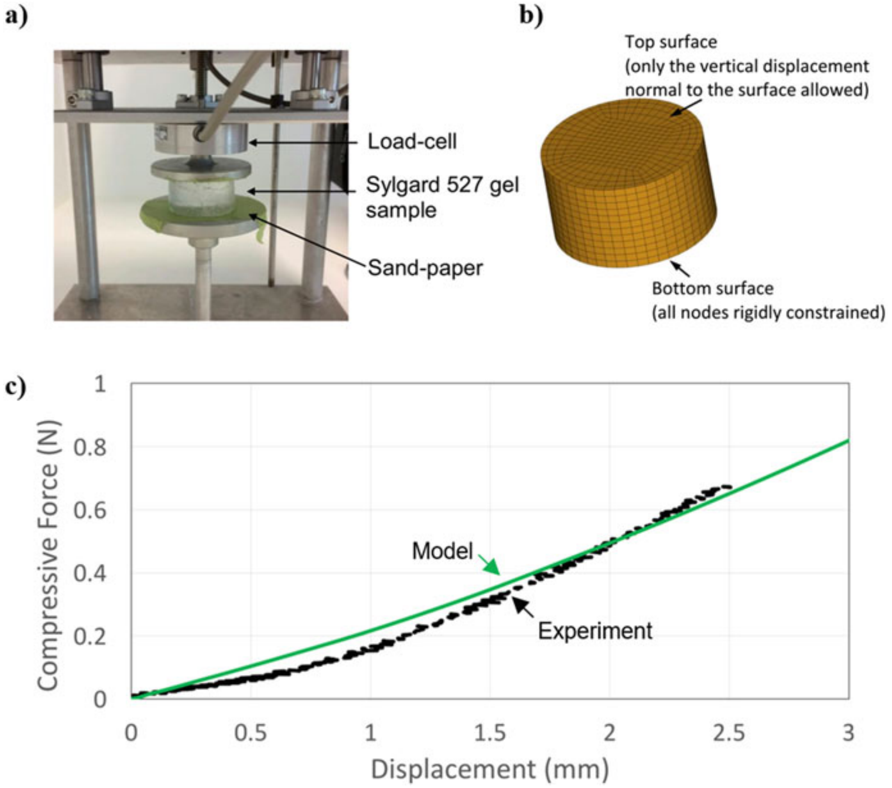

Fig. 3 (**a**) Compression of Sylgard 527 gel samples for determining the constitutive behaviour and shear modulus of the gel used in this study. (**b**) Finite element model of the experiments using the setup shown in figure (**a**). The model was implemented using ABAQUS non-linear finite element code. The gel sample was discretised using 4032 eight-noded hexahedral elements with hybrid formulation (solid element C3D8H in ABAQUS finite element code). The hybrid formulation was used to prevent volumetric locking. (**c**) Comparison of the results obtained using the model (green solid line) shown in figure (**b**) and the experimental data (black dotted line). The compression was done up to 2.5 mm (15% of the unloaded sample height)

we used the Poisson's ratio of 0.49—a value used in our previous studies [11]. Using this protocol, we determined that the shear modulus of Sylgard 527 gel used to prepare the sample analysed in this study was 1678 Pa. This result is consisted with the data we previously obtained [21] and with the literature [25, 26].

2.3 Determining the Parameters for New Algorithm for Modelling of Interactions Between the Needle and Soft Tissues Using Kinematic Approach

As explained in Sect. 2.1.2, our algorithm for modelling of needle–tissue interactions uses two parameters: puncture strain ε_p and deformation coefficient C_D that links the deformation of the material adjacent to the needle with the needle displacement. These parameters were determined from the experiments using the needle insertion into the silicone gel samples (tissue phantom) (Fig. 2).

Puncture Strain ε_p The needle force–insertion depth characteristics observed in this study exhibited a continuous increase without any visible local force drop that can be associated with the puncture (Fig. 6). Consequently, the puncture strain was designated an arbitrarily low value of $\varepsilon_p = 10^{-6}$. We considered also $\varepsilon_p = 0.0$, but decided against using it as it would not allow us to test the part of our new algorithm for modelling of interactions between the needle and tissue responsible for computing the puncture strain.

Deformation Coefficient C_D *(linking the deformation of the tissue adjacent to the needle with the needle motion)* Sylgard 527 gel tends to firmly stick/attach to smooth surfaces such as surgical needle shafts. From observation of the deformation the gel sample surface during the needle insertion, we determined that the gel adjacent to the needle moves/deforms by around 40–60% of the distance travelled by the needle tip. Consequently, we used the deformation coefficient of $C_D = 0.4$.

3 Results

Verification of the MTLED framework performance for predicting the responses of soft incompressible continua was done through modelling of indentation of Sylgard 527 gel sample (for the experimental setup and its model, see Fig. 1). We were able to obtain the reference solution using the established non-linear algorithms available in ABAQUS finite element code for the indentation depth of only 4.0 mm. At around 4.1 mm the finite element solution started to diverge. We hypothesise that this was caused by distortion of the elements forming the finite element mesh in the indentation area. As the MTLED framework uses the computational grid in a form of cloud points, it does not suffer from this type of instability. Therefore, using the MTLED framework, we obtained the stable result for the indentation depth of 10 mm which is the maximum indentation depth used in the experiments.

The force–indentation depth relationship from the MTLED framework is for practical purposes the same as the relationship obtained using non-linear finite element procedures available in ABAQUS finite element code and agrees well with the experimental data (Fig. 4). The difference between the modelling and experimental results for the indentation depth of 4 mm was only around 0.025 N

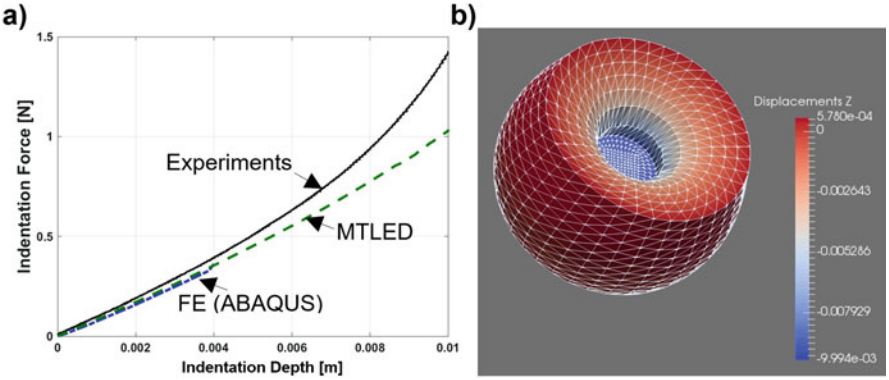

Fig. 4 (**a**) Verification of the Meshless Total Lagrangian Explicit Dynamics (MTLED) framework through modelling of the experiments (indentation of Sylgard 527 gel samples) conducted using the setup shown in Fig. 1. Comparison of the force–indentation depth relationship obtained using the MTLED framework (green dotted line), non-linear finite element procedures available in ABAQUS finite element (FE) code (blue dotted line), and the experimental data (black solid line)—average from three experiments. Using ABAQUS finite element code we were able to obtain the results for the indentation depth of up to only 4 mm after which the solution diverged. For the indentation depth of up to 4 mm, the results obtained using the MTLED framework and ABAQUS code are very close and cannot be visually distinguished. (**b**) Overall deformation of the meshless model for the indentation depth of 10 mm (the displacement scale in the figure is in meters). The interpolating nodes were connected to form the triangles to visualise the deformed model surface. The meshless discretisation is shown in Fig. 1c

which is around 5% of the measured force. The difference increases with the indentation depth. We propose the following two explanations for this phenomenon. The first is that we prescribed the displacements of the nodes on the sample surface in contact with the indenter face and did not directly model the indenter. This does not account for the contact between the gel and cylindrical surface of the indenter which occurs when the indentation depth increases (see Fig. 1a). The second possible explanation for the fact that the differences between the modelling and experimental result increased with the indentation depth can be that the neo-Hookean hyperelastic constitutive model we use here may not accurately represent Sylgard 527 stress–strain relationship for large strain. In this model, the strain energy is proportional to the second power of the principal stretch ratios (first left deformation tensor invariant) (see Eq. (1)). More complex hyperelastic models that include higher order terms in strain energy function (such as Ogden hyperelastic model used in our previous studies [21, 24]) may be needed to accurately represent the Sylgard 527 gel constitutive behaviour for large strain.

The results of modelling of needle insertion into a cylindrical sample of Sylgard 527 gel indicate that our kinematics approach for representing the needle–tissue (soft tissue phantom) interactions implemented in the MTLED framework not only provides a stable solution for large local strain induced by the needle (Fig. 5), but also accurately predicts the general behaviour and magnitude of the needle force–

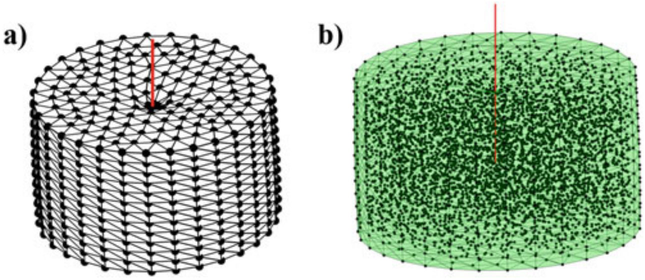

Fig. 5 Modelling of needle insertion into the Sylgard 527 gel sample using our meshless method for needle insertion simulation. (**a**) The predicted shape of the sample surface for the insertion depth of 10 mm. The interpolating nodes are connected to form the triangles to visualise the deformed model surface. (**b**) Position of the interpolating nodes for the needle insertion depth of 10 mm

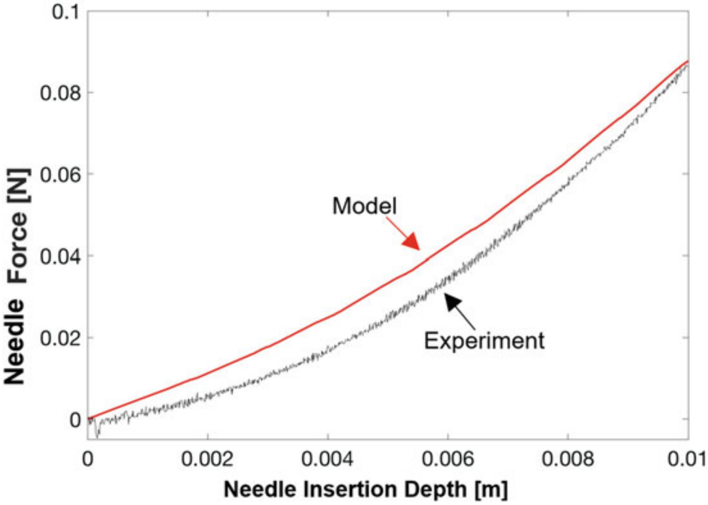

Fig. 6 Comparison of the force–insertion depth relationship when inserting a needle into the cylindrical samples of Sylgard 527 gel obtained using our meshless method for needle insertion simulation (red line) and the experimental data (black line). The needle insertion was conducted for the depth of up to 10 mm. The experimental setup is shown in Fig. 2. The model is shown in Figs. 2 and 5

insertion depth relationship (Fig. 6). The maximum difference between the force predicted by our method and experimental results was only around 25% (under 0.01 N). This difference can be minimised by adjusting the parameter C_D that links the deformation of the material adjacent to the needle with the needle displacement. However, this fairly straightforward exercise has not been conducted here as we are more interested in assessing predictive rather than explanatory power of our approach.

4 Discussion

The results of modelling of indentation of tissue phantom (Sylgard 527 gel sample) confirm the capability of Meshless Total Lagrangian Explicit Dynamics (MTLED) framework, in providing the stable solution of equations of continuum mechanics for large localised deformations/strain where the procedures available in established non-linear finite element codes (we used the ABAQUS code) tend to fail (Fig. 4). This makes the MTLED framework a suitable method for simulation of needle insertion and other surgical procedures.

The results of modelling of needle insertion into a Sylgard 527 gel sample indicate that our kinematics approach for representing the needle–tissue (soft tissue phantom) interactions, in which the deformation of the material adjacent to the needle is directly linked with the needle motion without any assumptions regarding the exact mechanism of the interactions between the needle and tissue (soft tissue phantom), correctly predicts the general behaviour of the needle force–insertion depth relationship (Fig. 6). The predicted force magnitude differed by only 25% from the experimentally observed value (Fig. 6). Similar difference (20%) between the modelling and experimental results was obtained by Oldfield et al. [10] who used extensive calibration of their high-resolution cohesive element model of needle insertion into the gelatine phantom. It might be expected that with more elaborate calibration, that includes determining the deformation coefficient C_D (that links the deformation of the material adjacent to the needle with the needle motion) by tracking the deformations at the selected locations within the tissue sample (tissue phantom) in the needle insertion area, the accuracy of force prediction obtained using our kinematics approach for modelling of interactions between the needle and tissue (tissue phantom) may improve. Another possible reason for the differences between the results of needle insertion simulation and experimental data observed here can be that, as discussed when analysing the results of modelling of Sylgard 527 gel sample indentation, the neo-Hookean hyperelastic constitutive model we use here may not accurately represent Sylgard 527 stress–strain relationship for large strain. This can be addressed through application of more complex hyperelastic models that include higher order terms in strain energy function (such as Ogden hyperelastic model).

The needle force–insertion depth characteristics obtained in this study using tissue phantom (Sylgard 527 gel) do not exhibit any significant force decrease/drop we observed in our previous experiments on needle insertion into swine brain specimens [24]. Consequently, we were not able to evaluate the performance of our meshless method for simulation of needle insertion into soft tissues for this important aspect of the needle force–insertion depth behaviour. Such evaluation requires studies that would compare the modelling results against the experimental data obtained using tissue/organ specimens rather than tissue phantoms.

Acknowledgements This research was supported by the Australian Government through the Australian Research Council's *Discovery Projects* funding scheme (project DP160100714). Adam Wittek and Anton Khau thank Dr Barry Doyle for use of the VascLab tension–compression rig.

References

1. Zhu Y, Magee D, Ratnalingam R, Kessel D (2007) A training system for ultrasound-guided needle insertion procedures. In Ayache N., Ourselin S. and Maeder A. (eds) Proc. of Medical Image Computing and Computer-Assisted Intervention – MICCAI 2007, Springer, Berlin, pp 566–574
2. Vega RA, Holloway KL, Larson PS (2014) Image-guided deep brain stimulation. Neurosurg Clin N Am 25:159–172
3. Apesteguía L, Pina LJ (2011) Ultrasound-guided core-needle biopsy of breast lesions. Insights Imaging 2:493–500
4. Leibinger A, Oldfield MJ, Rodriguez Y Baena F (2016) Minimally disruptive needle insertion: a biologically inspired solution. Interface Focus 6:20150107
5. Fichtinger G, Deguet A, Masamune K, Balogh E, Fischer GS, Mathieu H, Taylor RH, Zinreich SJ, Fayad LM (2005) Image overlay guidance for needle insertion in CT scanner. IEEE Trans Biomed Eng 52:1415–1424
6. Ungi T, Beiko D, Fuoco M, King F, Holden MS, Fichtinger G, Siemens DR (2014) Tracked ultrasound snapshots enhance needle guidance for percutaneous renal access: a pilot study. J Endourol 28:1040–1045
7. Bui HP, Tomar S, Courtecuisse H, Cotin S, Bordas SPA (2018) Real-time error control for surgical simulation. IEEE Trans Biomed Eng 65:596–607
8. Courtecuisse H, Allard J, Kerfriden P, Bordas SPA, Cotin S, Duriez C (2014) Real-time simulation of contact and cutting of heterogeneous soft-tissues. Med Image Anal 18:394–410
9. DiMaio SP, Salcudean SE (2003) Needle insertion modeling and simulation. IEEE Trans Robot Autom 19:864–875
10. Oldfield M, Dini D, Giordano G, Rodriguez y Baena F (2013) Detailed finite element modelling of deep needle insertions into a soft tissue phantom using a cohesive approach. Comput Methods Biomech Biomed Engin 16:530–543
11. Horton A, Wittek A, Joldes GR, Miller K (2010) A meshless Total Lagrangian explicit dynamics algorithm for surgical simulation. Int J Numer Methods Biomed Eng 26:977–998
12. Joldes GR, Chowdhury H, Wittek A, Miller K (2017) A new method for essential boundary conditions imposition in explicit meshless methods. Eng Anal Bound Elem 80:94–104
13. Miller K, Horton A, Joldes GR, Wittek A (2012) Beyond finite elements: a comprehensive, patient-specific neurosurgical simulation utilizing a meshless method. J Biomech 45:2698–2701
14. Joldes G, Bourantas G, Zwick B, Chowdhury H, Wittek A, Agrawal S, Mountris K, Hyde D, Warfield SK, Miller K (2019) Suite of meshless algorithms for accurate computation of soft tissue deformation for surgical simulation. Med Image Anal 56:152–171.
15. Jin X, Joldes GR, Miller K, Yang KH, Wittek A (2014) Meshless algorithm for soft tissue cutting in surgical simulation. Comput Methods Biomech Biomed Engin 17:800–817
16. Leibinger A, Forte AE, Tan Z, Oldfield MJ, Beyrau F, Dini D, Rodriguez Y Baena F (2016) Soft tissue phantoms for realistic needle insertion: a comparative study. Ann Biomed Eng 44:2442–2452
17. Chowdhury HA, Wittek A, Miller K, Joldes GR (2017) An element free Galerkin method based on the modified moving least squares approximation. J Sci Comput 71:1197–1211
18. Washio T, Chinzei K (2004) Needle force sensor, robust and sensitive detection of the instant of needle puncture. In: 7th International Conference on Medical Image Computing and Computer-Assisted Intervention MICCAI 2004, Proceedings: Lecture Notes in computer Science 3217, Berlin, Springer, pp 113–120
19. Babuska I, Oden JT (2004) Verification and validation in computational engineering and science: basic concepts. Comput Methods Appl Mech E 193:4057–4066
20. Bottan S, Poulikakos D, Kurtcuoglu V (2012) Phantom model of physiologic intracranial pressure and cerebrospinal fluid dynamics. IEEE Trans Biomed Eng 59:1532–1538

21. Ma J, Wittek A, Singh S, Joldes G, Washio T, Chinzei K, Miller K (2010) Evaluation of accuracy of non-linear finite element computations for surgical simulation: study using brain phantom. Comput Methods Biomech Biomed Engin 13:783–794
22. Agrawal S, Wittek A, Joldes G, Bunt S, Miller K (2015) Mechanical properties of brain–skull interface in compression. In: Doyle B, Miller K, Wittek A, Nielsen MFP (eds) Computational Biomechanics for Medicine X: New Approaches and New Applications. Springer, Cham, pp 83–91
23. Rivlin RS, Sawyers KN (1976) The strain-energy function for elastomers. Trans Soc Rheol 20:545–557
24. Wittek A, Dutta-Roy T, Taylor Z, Horton A, Washio T, Chinzei K, Miller K (2008) Subject-specific non-linear biomechanical model of needle insertion into brain. Comput Methods Biomech Biomed Engin 11:135–146
25. Ivarsson J, Viano DC, Lövsund P, Aldman B (2000) Strain relief from the cerebral ventricles during head impact: experimental studies on natural protection of the brain. J Biomech 33:181–189
26. Basati SS, Harris TJ, Linninger AA (2011) Dynamic brain phantom for intracranial volume measurements. IEEE Trans Biomed Eng 58:1450–1455

A Biomechanical Study on the Use of Curved Drilling Technique for Treatment of Osteonecrosis of Femoral Head

Mahsan Bakhtiarinejad, Farshid Alambeigi, Alireza Chamani, Mathias Unberath, Harpal Khanuja, and Mehran Armand

Abstract Osteonecrosis occurs due to the loss of blood supply to the bone, leading to spontaneous death of the trabecular bone. Delayed treatment of the involved patients results in collapse of the femoral head, which leads to a need for total hip arthroplasty surgery. Core decompression, as the most popular technique for treatment of the osteonecrosis, includes removal of the lesion area by drilling a straight tunnel to the lesion, debriding the dead bone and replacing it with bone substitutes. However, there are two drawbacks for this treatment method. First, due to the rigidity of the instruments currently used during core decompression, lesions cannot be completely removed and/or excessive healthy bone may also be removed with the lesion. Second, the use of bone substitutes, despite its biocompatibility and osteoconductivity, may not provide sufficient mechanical strength and support for the bone. To address these shortcomings, a novel robot-assisted curved core decompression (CCD) technique is introduced to provide surgeons with direct access to the lesions causing minimal damage to the healthy bone. In this study, with the aid of finite element (FE) simulations, we investigate biomechanical performance of core decompression using the curved drilling technique in the presence of normal gait

---

M. Bakhtiarinejad (✉) · F. Alambeigi · A. Chamani
Laboratory for Computational Sensing and Robotics, Department of Mechanical Engineering, Johns Hopkins University, Baltimore, MD, USA
e-mail: mbnejad@jhu.edu

M. Unberath
Laboratory for Computational Sensing and Robotics, Department of Computer Science, Johns Hopkins University, Baltimore, MD, USA

H. Khanuja
Department of Orthopedic Surgery, Johns Hopkins Medical School, Baltimore, MD, USA

M. Armand
Laboratory for Computational Sensing and Robotics, Department of Mechanical Engineering, Johns Hopkins University, Baltimore, MD, USA

Department of Orthopedic Surgery, Johns Hopkins Medical School, Baltimore, MD, USA

Applied Physics Laboratory, Johns Hopkins University, Laurel, MD, USA

M. P. Nash et al. (eds.), *Computational Biomechanics for Medicine*,
https://doi.org/10.1007/978-3-030-15923-8_7

loading. In this regard, we compare the result of the CCD using bone substitutes and flexible implants with other conventional core decompression techniques. The study finding shows that the maximum principal stress occurring at the superior domain of the neck is smaller in the CCD techniques (i.e., 52.847 MPa) compared to the other core decompression methods; furthermore, the peak value of normal stress at the interface for the CCD model is substantially smaller than traditional and advanced core decompression techniques (89% and 76%, respectively). FE results demonstrate the superior performance of CCD compared to the other approaches without any compromise to patient's safety and markedly reducing the risk of femoral fracture in the postoperative phase for normal gait loading.

Keywords Osteonecrosis · AVN · Core decompression · Curved drilling · Finite element method · Biomechanical analysis · Stress · Strain · Femoral fracture

1 Introduction

Avascular necrosis (AVN) of the femoral head, also known as osteonecrosis, is a degenerative joint disease, which happens due to the interruption of blood supply to the bone leading to the spontaneous death of the trabecular bone (Fig. 1a, b) [1, 2]. The rate of occurrence of this disease in the USA is between 10,000 and 30,000 per year, which typically happens in young adults with around 35–50 years of age. Studies show that due to late diagnosis and treatment, more than 85% of the early-stage AVN leads to collapse of the femur's subchondral and finally total hip arthroplasty [2]. The key parameter in successful treatment of AVN is complete removal of the necrotic region with individual variation in shapes and locations, which is typically not easily accessible due to the complexity of the femur anatomy and utilizing rigid instruments [3].

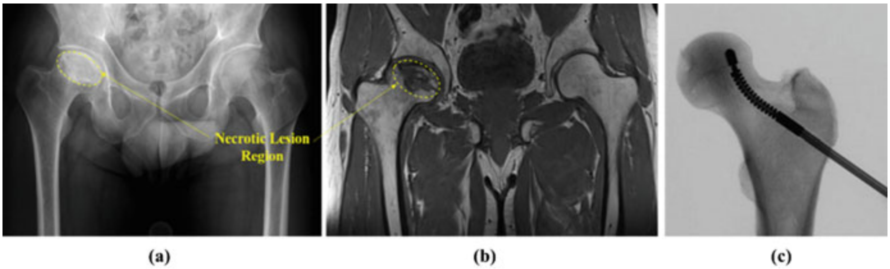

Fig. 1 (**a**) Fluoroscopic and (**b**) MRI image of a patient suffering from osteonecrosis of right femoral head (Case courtesy of Dr Henry Knipe, Radiopaedia.org, rID: 44260); (**c**) Fluoroscopic image of the core decompression procedure using the curved drilling technique

Literature documents several early-stage (i.e., before femoral head collapse) AVN treatments including osteotomy [4] and various types of core decompressions [5]. Among these approaches, core decompression (CD) is a well-established procedure performed with the goal of reducing the femoral head pressure and revitalizing the bone by restoring blood flow to the lesion area. In the simple CD procedure, surgeon drills either one straight tunnel of 8–10 mm diameter or multiple tunnels of 3.2 mm diameter with a single-entry point in the lateral subtrochanteric region [2].

This approach is plagued with the following challenges:

1. The rigidity of the tools currently utilized does not provide the surgeon with sufficient access for complete removal of necrotic lesions; each of which tends to be of a unique and amorphous shape.
2. Consequential weakening of the healthy bone puts the patient at risk of subchondral bone collapse either during or after surgery, due to the patient's weight.

As a remedy to the second issue, some surgeons use structural bone grafts [6] or bone grafts with porous tantalum implant [7] to provide additional structural support for the subchondral bone and stimulate bone formation with blood and bone cells.

To address the accessibility and the structural strength issues, Landgraeber et al. [8] developed the advanced core decompression (ACD) technique that uses a percutaneous expandable reamer together with an artificial bone graft (i.e., PRO-DENSE®, Wright Medical TM, Arlington, TN, USA). Consequently, they could show a better accessibility to the necrotic lesion area and achieve a relatively good compressive strength for the first 13 weeks after surgery. However, this approach has two main shortcomings. First, in order to reach the necrotic region, the expandable reamer generates a relatively large conical hole, which unnecessarily removes healthy tissues along with the necrotic lesions, thereby potentially further weakening the femoral head. Also, the incorporated bone substitute becomes weaker after 26 weeks due to triphasic resorption [9].

To address the aforementioned challenges in core decompression, curved drilling technique has been recently proposed [10, 11]. In this approach, the authors used a continuum dexterous manipulator [12, 13] and developed appropriate flexible drilling tools [14, 15] to increase the reachability into necrotic regions while minimizing the damage to safe tissues as opposed to the mentioned techniques utilizing rigid instruments. In this study, we investigate the effect of curved core decompression (CCD) on the structural stability of the femoral head after AVN treatment using biomechanical analysis.

We perform finite element (FE) analysis to evaluate the biomechanical performance of the CCD (Fig. 1c) against (1) traditional core decompression and (2) ACD technique reinforced using PRO-DENSE bone substitute. In order to evaluate neck stability and fracture risk after core decompression, we also investigate traditional CD and CCD techniques using flexible Nitinol implant as an alternative bone substitute.

2 Materials and Methods

2.1 Geometrical Modeling

We first generate a three-dimensional (3D) model of the femur from segmented computed tomography (CT) scan of the specimen. Through a threshold-based segmentation of the bony anatomy, the domains of the femur are identified using image processing software, Medical Imaging Interaction Toolkit (MITK) [16]. Manual refinement improves the segmentation and smoothens the three-dimensional femur model [17]. Using SolidWorks (Dassault Systèmes SolidWorks Corporation, MA, USA) software, we first consider an arbitrary necrotic region area, which is not completely accessible with the simple CD approach and then, modify the 3D models based on the ACD and CCD techniques. Figure 2 demonstrates the aforementioned 3D models together with the considered drilled tunnels and an arbitrary lesion area in the femoral head. For all models, we consider a similar single-entry point in the lateral subtrochanteric region and lesion area to study the biomechanical performance of these approaches in the presence of identical normal walking loads. For the case of ACD, the size of the conical head is designed such that the tunnel can reach the lesion region.

2.2 Finite Element Simulation

The finite element model of the femur is generated using linear 10-node tetrahedral elements (Fig. 2) in COMSOL Multiphysics® (COMSOL AB, Stockholm, Sweden). An automated mesh convergence is performed during the simulation in COMSOL

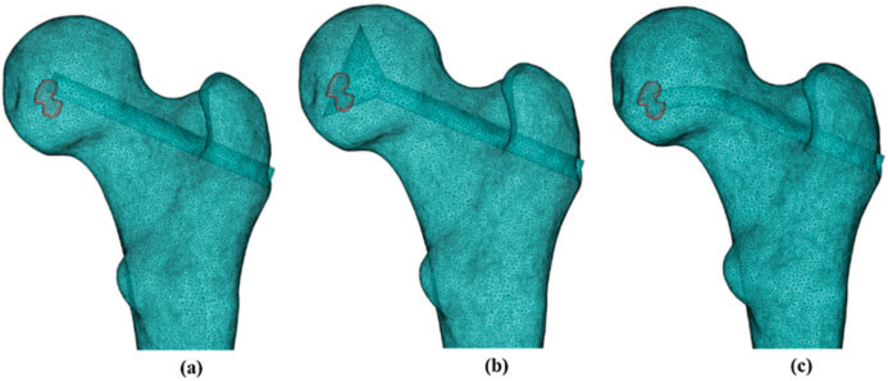

Fig. 2 Geometrical and finite element models of (**a**) CD, (**b**) ACD, and (**c**) CCD configurations with the arbitrary lesion area

and the largest mesh size that would produce the converging results is chosen. The element numbers for final meshes are displayed in Table 1.

For material properties of the femur, a linear, elastic, and isotropic bone with 3 mm uniform thickness of the cortical bone layer [18] and internal cancellous bone is considered. For this purpose, the distance between triangular surfaces of the femur and centroids of the bone elements is found using closest neighbor and bounding spheres approach of the ICP algorithm [19]. The elements within 3 mm of the surface bone are assigned as cortical and the remaining as cancellous. The average Young's modulus and Poisson's ratio of the cortical and cancellous regions of the bone are considered as 12 GPa and 600 MPa and 0.40 and 0.29, respectively. PRO-DENSE and Nitinol elements are also assumed linear, elastic, and isotropic with average Young's modulus of 221.6 MPa and 83 GPa and Poisson's ratio of 0.3 and 0.33, respectively [2, 18, 20, 21].

We investigate the fracture risk for the peak hip joint loads during normal walking. The applied load of 2132.8 (−411.24, −247.1, 2078.14) N is extracted from the patient data set "HSR" measured during normal walking [18, 22]. The load is distributed over the cartilaginous surface of the femur that is in contact within the hip joint. A fixed boundary condition is applied at the distal end of the femur (Fig. 3).

Table 1 Number of the elements in FE model meshes

Model	Element
CD	524,940
ACD	532,832
CCD	524,894
Untreated	495,062

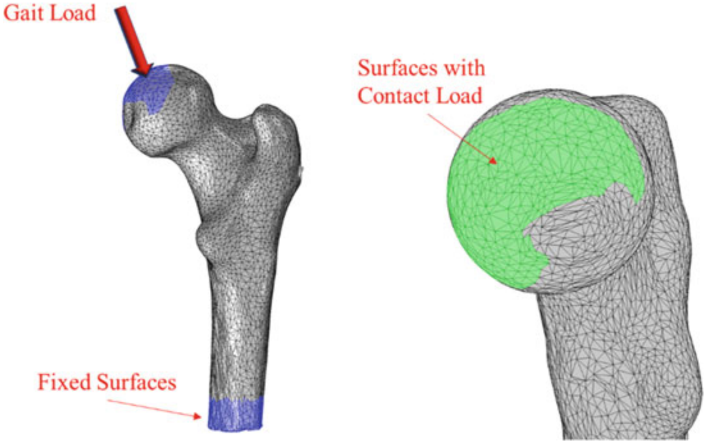

Fig. 3 Fixed boundary and loading condition

3 Computational Results

In this study, we define the bone failure criteria based on the maximum principal stress and maximum principal strain. During normal walking, tensile stress emerges in the subtrochanteric region; therefore, maximum first principal stress of the femur is compared with $\sigma_{ult}^{t} = 110$ MPa which is the tensile strength of cortical bone reported in the literature [2, 18]. The maximum first principal stress given in percent of the tensile strength is displayed in Table 2 for all models.

All the treated configurations and untreated femur exhibit typical tensile stress distribution subject to gait loading as shown in Fig. 4. The maximum principal stress in all models occurs at the superior domain of the neck and is smaller than tensile strength σ_{ult}^{t}. Furthermore, high stresses emerge in distal regions of the subtrochanter as well as in the small regions around the drilling areas within the bone (Fig. 4g, h).

In the treated models, the maximum tensile stress is 48–51% of the appropriate tensile strength which is slightly larger than that of the untreated model (47%). Therefore, the fracture risk is estimated quite low for all the models subject to normal walking loading. The peak normal and shear stresses at the interface for all treated models are also computed and shown in Table 3. The peak stress values of the CD and CCD configurations decrease substantially using a bone substitute with lower modulus of elasticity; consequently, using stiffer filling material, Nitinol, increasingly raises the peak of the normal and shear stresses compared to the PRO-DENSE.

Similar distribution of normal and shear stresses is observed at the interface of the treated models (Figs. 5 and 6) with the peak values appearing at the tip of the interface located in the femoral head. The peak value of the normal stress for the CCD technique using PRO-DENSE is 1.96 MPa which is substantially lower than that of the CD and ACD (4.549 and 8.058 MPa). In addition, the shear stress of CCD using PRO-DENSE has a peak value of 4.39 MPa which is lower than that of the ACD (5.941 MPa); however, it is higher than peak shear stress for the CD procedure (2.61 MPa). The distribution of normal and shear stress of the ACD configuration using PRO-DENSE demonstrates that due to larger surfaces of the tip of the tunnel compared to the CCD procedure, surfaces of high stress at the femoral head are more spread.

Table 2 Maximum first principal stress of the femur in percent of the tensile strength σ_{ult}^{t} subject to normal walking loading

Model	Maximum first principal stress (MPa)	Percent of σ_{ult}^{t}
CD with PRO-DENSE	53.678	49
CD with Nitinol	53.676	49
ACD with PRO-DENSE	55.667	51
CCD with PRO-DENSE	52.856	48
CCD with Nitinol	52.847	48
Untreated	51.872	47

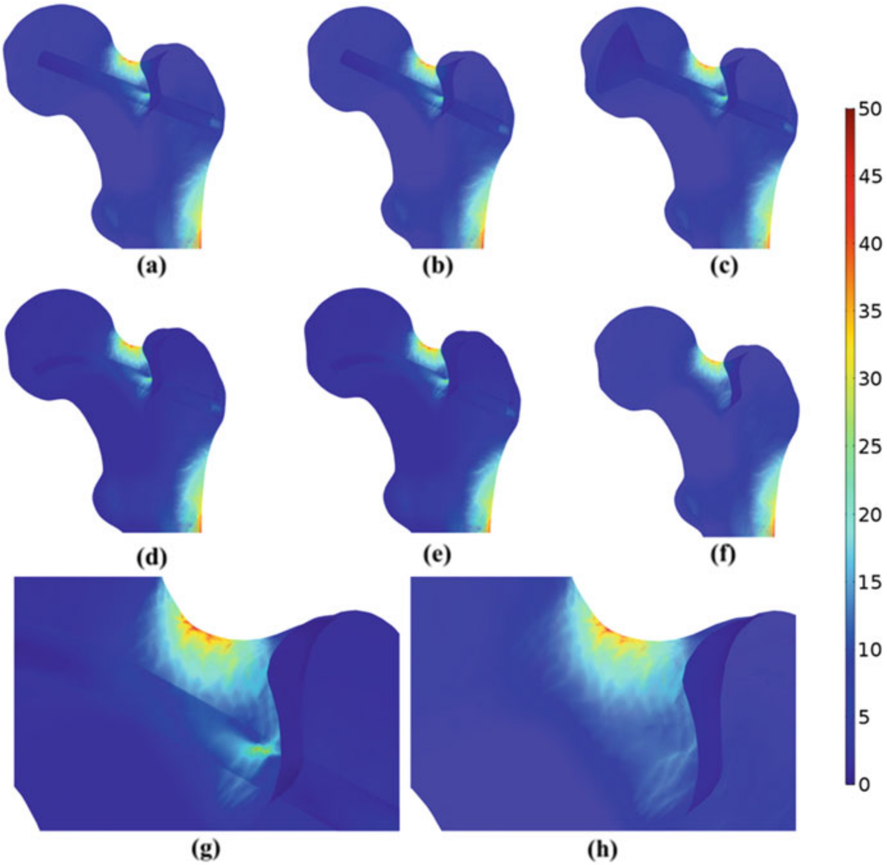

Fig. 4 First principal stress distribution (MPa) in femoral bone using (**a**) CD with PRO-DENSE, (**b**) CD with Nitinol, (**c**) ACD with PRO-DENSE, (**d**) CCD with PRO-DENSE, (**e**) CCD with Nitinol, and (**f**) Untreated model. (**g**) Enlarged view of CCD with PRO-DENSE, (**h**) Enlarged view of Untreated model

Table 3 Peak normal stress and shear stress at the interface

Model	Peak normal stress (MPa)	Peak shear stress (MPa)
CD with PRO-DENSE	4.549	2.606
CD with Nitinol	17.368	14.356
ACD with PRO-DENSE	8.058	5.941
CCD with PRO-DENSE	1.958	4.388
CCD with Nitinol	45.428	40.141

Based on the principal maximum strain criterion, the maximum (ε_{max}) and minimum (ε_{min}) principal strain values computed at the centroid of each bone element, are used to determine the volume of the failed elements where the bone tissue reaches the yield strain. For this purpose, greater value of $|\varepsilon_{max}|$

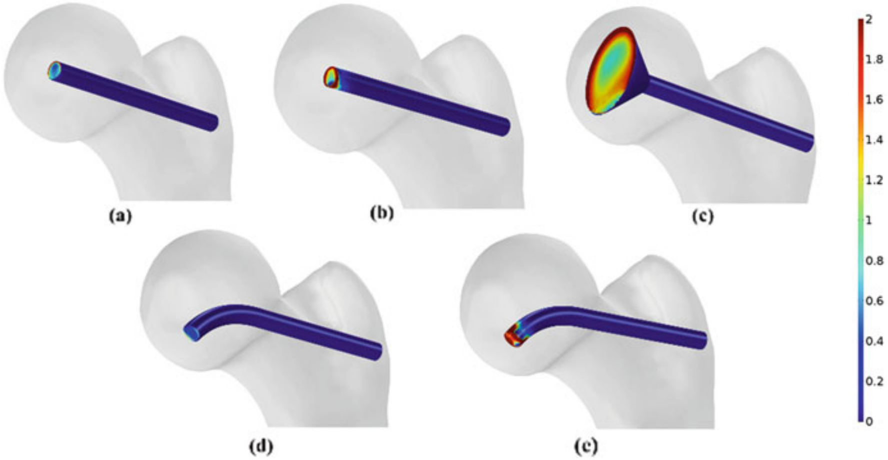

Fig. 5 Normal stress distribution (MPa) at the interface using (**a**) CD with PRO-DENSE, (**b**) CD with Nitinol (**c**) ACD with PRO-DENSE, (**d**) CCD with PRO-DENSE, and (**e**) CCD with Nitinol

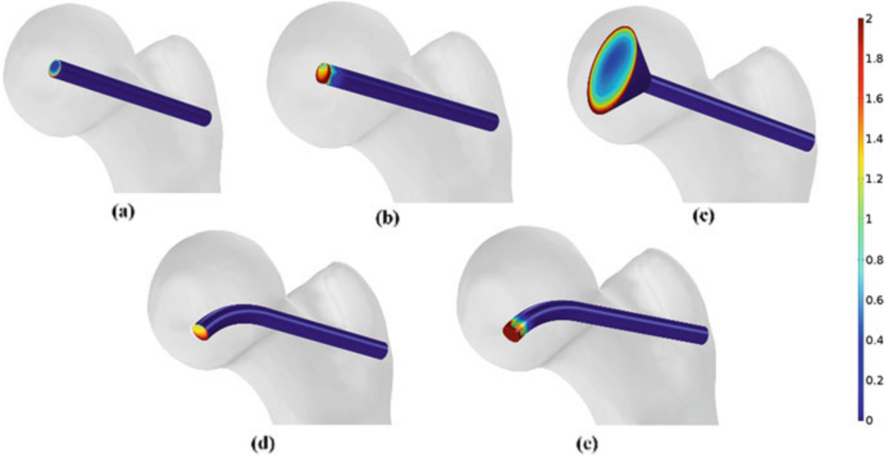

Fig. 6 Shear stress distribution (MPa) at the interface using (**a**) CD with PRO-DENSE, (**b**) CD with Nitinol (**c**) ACD with PRO-DENSE, (**d**) CCD with PRO-DENSE, and (**e**) CCD with Nitinol

and $|\varepsilon_{min}|$ is compared with the appropriate compressive and tensile yield strains which is $\varepsilon_{yC} = 0.0104$ for compression and ε_{yT}=0.0073 for tension [23, 24]. Consequently, the volume of the failed elements is computed by adding up the volume of the elements that have a strain higher than its yield value (Table 4). It is demonstrated that all treated and untreated models have similar percentage of the volume failure, that is, 0.04% of the total bone volume.

Table 4 Volume of the failed elements using principal maximum strain criterion

Model	Volume of failed elements (mm^3)	Femur volume (mm^3)
CD with PRO-DENSE	56	141,483
CD with Nitinol	56	141,483
ACD with PRO-DENSE	55	138,687
CCD with PRO-DENSE	57	141,416
CCD with Nitinol	57	141,416
Untreated	55	143,419

4 Discussion and Conclusion

The ultimate tensile stress of the cortical bone reported in the literature varies from 78 MPa to 151 MPa [18, 25–27]. In this study, a limit tensile strength of 110 MPa is chosen as a reference [2, 9, 18]. According to Table 2, the maximum principal stress in untreated and treated models is on average about 52 MPa, which is smaller than both the ultimate tensile strength of the chosen cortical bone (i.e., 110 MPa) and the reported maximum principal stress (i.e., 75.46 MPa) [28]. It is demonstrated that the maximum principal stress in the treated models using curved drilling technique utilizing PRO-DENSE (i.e., ~52.847 MPa) is smaller than the other techniques (i.e., ACD and CD). Moreover, the peak value of normal stress at the interface for the CCD model using PRO-DENSE decreases substantially when compared to the CD and ACD (57% and 76%, respectively); in addition, the peak value of shear stress for the CCD with PRO-DENSE is 26% lower than ACD showing the advantage of CCD compared to the other approaches.

Simulation results, therefore, confirm that the CCD approach like the other approaches does not increase the risk of femoral fracture. Tren et al. [9] also achieved similar results for their ACD technique. However, ACD unnecessarily removes healthy tissues and results in larger values of maximum principal stress at the superior domain of the femoral neck and peak values of normal and shear stresses at the tip of the interface compared to CCD (Tables 2 and 3).

The simulation of CCD technique with PRO-DENSE generates the smallest peak value of normal stress, whereas CCD with Nitinol results in the largest peak stress. This result is in accordance with the reported results in [7] and [9] representing that the use of a stiff implant increases the maximum stress values while incorporating a lower stiffness of the bone substitutes (e.g., PRO-DENSE) may have better outcomes. On the other hand, as mentioned in [9], incorporating bone substitute with low stiffness such as PRO-DENSE may increase the risk of femoral fracture due to the triphasic resorption after 26 weeks [9]. Considering this limitation and the acceptable maximum principal stress of the bone using CCD with Nitinol implant, the use of this implant can be justified as compared to the PRO-DENSE. A potential path forward that may constitute a healthy compromise between the two aforementioned approaches can be the use of a calcium phosphate bone cement reinforced with a bendable implant. This approach will increase bone strength while minimizing femoral damage risk during the first weeks of the postoperative phase.

As shown in Tables 3 and 4 and Figs. 5 and 6, the maximum principal, normal and shear stresses of ACD undergo larger values compared to the CCD method. ACD, therefore, may compromise safety by removing the healthy bone tissue and increasing the risk of collapse of the articular surface [29, 30]. It also may cause femoral head depression during and after the operation which happens due to larger surfaces of high stress at the tip of the interface located at the femoral head.

This preliminary study is performed on a simulated lesion on a femur model. Future studies must consider the effect of each treatment technique in the presence of a variety of lesion geometries. Also, in the future, the FE model of the CCD technique using PRO-DENSE in combination with the Nitinol implant needs to be investigated and further enhanced to include more geometric details including a more accurate interface between the bone and the implant. Optimizing the bending curvature when approaching the lesion location may also enhance the effectiveness of the CCD approach. Eventually, the FE model analysis can become a part of the AVN evaluation and prognosis procedures, providing patient-specific results.

Acknowledgments The research reported in this publication was supported by the National Institute of Arthritis and Musculoskeletal and Skin Diseases of the National Institutes of Health under Award Number R01EB016703 and R01EB023939. The content is solely the responsibility of the authors and does not necessarily represent the official views of the National Institutes of Health.

References

1. Mont MA (1999) Symptomatic multifocal osteonecrosis: a multicenter study. Clin Orthop Relat Res 369:312–326
2. Lutz A et al (2011) Numerical studies on alternative therapies for femoral head necrosis. Biomech Model Mechanobiol 10(5):627–640
3. Nishii T et al (2002) Significance of lesion size and location in the prediction of collapse of osteonecrosis of the femoral head: a new three-dimensional quantification using magnetic resonance imaging. J Orthop Res 20(1):130–136
4. Ganz R, Büchler U (1983) Overview of attempts to revitalize the dead head in aseptic necrosis of the femoral head—osteotomy and revascularization. Hip:296, 296–305
5. Lee MS et al (2008) Elevated intraosseous pressure in the intertrochanteric region is associated with poorer results in osteonecrosis of the femoral head treated by multiple drilling. J Bone Joint Surg Br 90(7):852–857
6. Babhulkar S (2009) Osteonecrosis of femoral head: treatment by core decompression and vascular pedicle grafting. Indian J Orthop 43(1):27
7. Tsao AK et al (2005) Biomechanical and clinical evaluations of a porous tantalum implant for the treatment of early-stage osteonecrosis. J Bone Joint Surg Am 87:22–27
8. Landgraeber S et al (2013) Advanced core decompression, a new treatment option of avascular necrosis of the femoral head–a first follow-up. J Tissue Eng Regen Med 7(11):893–900
9. Tran TN et al (2016) Effect of the stiffness of bone substitutes on the biomechanical behaviour of femur for core decompression. Med Eng Phys 38(9):911–916

10. Alambeigi F et al (2017) A curved-drilling approach in core decompression of the femoral head osteonecrosis using a continuum manipulator. IEEE Robot. Autom. Lett 2(3):1480–1487
11. Alambeigi F, Bakhtiarinejad M, Azizi A, Hegeman R, Iordachita I, Khanuja H, Armand M (2018) Inroads toward robot-assisted internal fixation of bone fractures using a bendable medical screw and the curved drilling technique. In: Proceedings of IEEE RAS/EMBS international conference on biomedical robotics and biomechatronics (BioRob), pp 1–6
12. Wilkening P, Alambeigi F, Murphy RJ, Taylor RH, Armand M (2017) Development and experimental evaluation of concurrent control of a robotic arm and continuum manipulator for osteolytic lesion treatment. IEEE Robot. Autom. Lett 2(3):1625–1631
13. Alambeigi F, Murphy RJ, Basafa E, Taylor RH, Armand M (2014) Control of the coupled motion of a 6 DoF robotic arm and a continuum manipulator for the treatment of pelvis osteolysis. In: Conference proceedings: annual international conference of the IEEE Engineering in Medicine and Biology Society. IEEE Engineering in Medicine and Biology Society. Annual Conference, vol 2014, p 6521. NIH Public Access
14. Alambeigi F, Yu W, Murphy RJ, Iordachita I, Armand M (2016) Toward robot-assisted hard osteolytic lesion treatment using a continuum manipulator. In: 2016 IEEE 38th annual international conference of the engineering in medicine and biology society (EMBC). IEEE, pp 5103–5106
15. Alambeigi, F, Sefati S, Murphy RJ, Iordachita I, Armand M (2016) Design and characterization of a debriding tool in robot-assisted treatment of osteolysis. In: 2016 IEEE international conference on robotics and automation (ICRA). IEEE, pp 5664–5669
16. Wolf I et al (2005) The medical imaging interaction toolkit. Med Image Anal 9(6):594–604
17. Murphy RJ et al (2015) Development of a biomechanical guidance system for periacetabular osteotomy. Int J Comput Assist Radiol Surg 10(4):497–508
18. Tran TN et al (2014) Experimental and computational studies on the femoral fracture risk for advanced core decompression. Clin Biomech 29(4):412–417
19. Nuchter A, Lingemann K, Hertzberg J (2007) Cached kd tree search for ICP algorithms. In: Sixth international conference on 3-D digital imaging and modeling, 2007. 3DIM'07. IEEE
20. Keyak JH et al (1997) Prediction of femoral fracture load using automated finite element modeling. J Biomech 31(2):125–133
21. Keaveny TM et al (1994) Trabecular bone exhibits fully linear elastic behavior and yields at low strains. J Biomech 27(9):1127–1136
22. Bergmann G et al (2001) Hip contact forces and gait patterns from routine activities. J Biomech 34(7):859–871
23. Yosibash Z, Tal D, Trabelsi N (2010) Predicting the yield of the proximal femur using high-order finite-element analysis with inhomogeneous orthotropic material properties. Philos Trans A Math Phys Eng Sci 368(1920):2707–2723
24. Basafa E et al (2013) Patient-specific finite element modeling for femoral bone augmentation. Med Eng Phys 35(6):860–865
25. Burstein AH, Reilly DT, Frankel VH (1973) Failure characteristics of bone and bone tissue. In: Perspectives in biomedical engineering. Palgrave Macmillan, London, pp 131–134
26. Dempster WT, Liddicoat RT (1952) Compact bone as a non-isotropic material. Dev Dyn 91(3):331–362
27. Wirtz DC et al (2000) Critical evaluation of known bone material properties to realize anisotropic FE-simulation of the proximal femur. J Biomech 33(10):1325–1330
28. Floerkemeier T et al (2011) Core decompression and osteonecrosis intervention rod in osteonecrosis of the femoral head: clinical outcome and finite element analysis. Int Orthop 35(10):1461–1466
29. Mwale F et al (2011) Abnormal vascular endothelial growth factor expression in mesenchymal stem cells from both osteonecrotic and osteoarthritic hips. Bull NYU Hosp Jt Dis 69(1):S56
30. Pierce TP et al (2015) A current review of non-vascularized bone grafting in osteonecrosis of the femoral head. Cur Rev Musculoskelet Med 8(3):240–245

A Hybrid 0D–1D Model for Cerebral Circulation and Cerebral Arteries

Nixon Chau and Harvey Ho

Abstract In this paper we present a hybrid 0D–1D model for the cerebral circulation and blood flow in large cerebral arteries. The 0D model contains the electrical analog circuit running from the aorta to the circle of Willis (CoW), and the venous network from the superior sagittal sinus (SSS) to the superior vena cava (SVC). To simulate the cerebral autoregulation, the vascular bed between the arterial and venous networks is implemented using an inductor/resistor couple. An artificial pulsatile pressure waveform includes the normal (∼100 mmHg), hypotensive (∼50 mmHg) and hypertensive (∼150 mmHg) phases. A 1D model is used to numerically solve the 1D Navier–Stokes equations coupled with an empirical arterial wall equation. The 1D model is then applied to the internal carotid, middle and anterior cerebral arteries (ICA, MCA and ACA) in the CoW, with the simulation results from the 0D model as boundary conditions. With this hybrid 0D–1D approach, we show that: (a) the cerebral flow may regain a normal flow rate value (∼600 mL/min) within several cardiac cycles; (b) an incomplete CoW can substantially affect the flow distribution in CoW; and (c) the flow rates in the MCA, ACA and PCA alter in response to the cerebral regulation. In conclusion a hybrid 0D–1D model for the cerebral blood flow is proposed, which can potentially be used for the cerebral flow modelling of different age groups or under different vascular diseases.

Keywords Cerebral circulation · Model · Electrical analog · Brain

1 Introduction

The brain accounts for only 2% of the body mass, yet the cerebral blood flow (CBF) receives approximately 14% of the cardiac output (∼5 L/min) [1]. Human consciousness is lost after only a few seconds of cerebral ischemia, and irreversible

---

N. Chau · H. Ho (✉)
Auckland Bioengineering Institute, The University of Auckland, Auckland, New Zealand
e-mail: harvey.ho@auckland.ac.nz

M. P. Nash et al. (eds.), *Computational Biomechanics for Medicine*,
https://doi.org/10.1007/978-3-030-15923-8_8

neuronal damage occurs after 4 min [1]. Therefore, CBF must be maintained within a narrow physiological range despite cerebral perfusion pressure (CPP) variations, which can deviate from a normal mean value of 100 mmHg to as low as 50 mmHg or to as high as 180 mmHg [1]. This homeostatic mechanism is known as cerebral autoregulation, which involves a myogenic response occurring at small arteries and arterioles (diameter 100–200 μm) in the vascular bed [1].

Although numerous computational/mathematical models have been proposed for the cerebral circulation employing different modelling techniques (e.g., see [2–4, 6–8]), modelling for the autoregulation mechanism is only described in a small number of publications, using either lumped parameter or distributed circuit models. For example, Ursino et al. used nonlinear resistors and capacitors to mimic the sigmoidal curve of blood flow regulation [2], and Gao et al. used an empirical step equation to model the varying resistance with respect to different blood pressure [9].

In our previous work, an anatomically accurate one-dimensional (1D) cerebral arterial and venous model was constructed [7]. However, the arterial and venous flows in that model were not connected, and the autoregulation mechanism was not implemented. The aim of this work is to construct a cerebral circulation model using a different approach, i.e., using an electrical analog model (also known as 0D model) that includes as many topological features of the cerebral vasculature as possible while implementing an autoregulation mechanism. Then, the simulation results are utilised as boundary conditions for flow solvers at a higher dimensional level, such as the 1D model. This falls in the same vein as a typical 0D–1D coupling scheme whereby the 0D or lumped parameter model is used as the out boundary conditions [6]. In this short paper we apply this approach to several major arteries of the Circle of Willis (CoW), i.e., the internal carotid, the middle and anterior cerebral arteries (ICA, MCA and ACA).

2 Methods

2.1 The Cerebral Vascular Anatomy and 0D Model Design

Oxygenated blood is delivered to the brain via two pairs of arteries, the carotid arteries (CA) and vertebral arteries (VA). After entering the skull, they form a ring-like anastomotic structure called the CoW (Fig. 1). After irrigating brain tissues, the deoxygenated blood is drained by the cerebral venous network, whose morphology is more variant than its arterial counterpart due to the more compliant venous wall and low venous pressure [7]. The main cerebral arteries and veins are illustrated in Fig. 1a (vessel abbreviations are explained in the caption). Its corresponding schematic circuit is shown in Fig. 1b, whereby the arrows in the circuit represent blood flow directions. The heart, which pumps blood through the

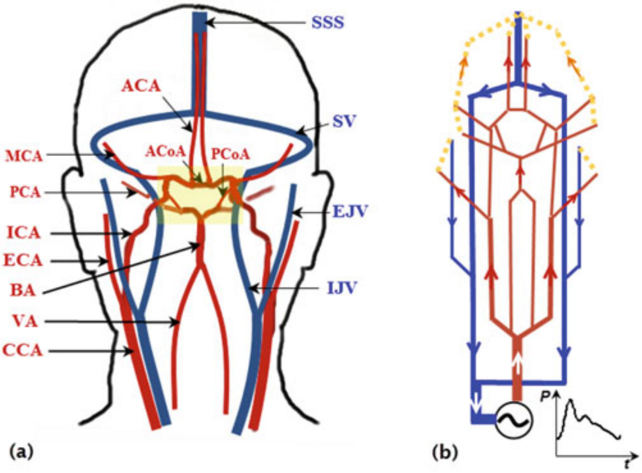

Fig. 1 (**a**) The cerebral vascular anatomy. The vessels in red are arteries, in blue, veins. Note that the CoW, highlighted in yellow, forms at the base of skull; (**b**) Schematic circuit of the cerebral circulation. CCA, ICA and ECA common, internal and external carotid artery, respectively; BA basilar artery; VA vertebral artery; MCA, PCA and ACA middle, posterior and anterior cerebral artery, respectively; SSS superior sagittal sinus; SV sigmoid vein; EJV and IJV external and internal jugular vein, respectively

cerebral vasculature, is represented by a power source whose voltage waveform is approximated by the first five harmonics of aortic pressure (also shown in the inset of Fig. 1).

The typical lengths and diameters of the cerebral arterial/venous tree are provided in the Appendix.

2.2 *The Electrical Analog Model*

An electrical circuit was constructed to mimic the topology of the cerebral vasculature of Fig. 1b. In this circuit, each arterial/venous segment was represented by a corresponding resistor. The parameter for each resistor is calculated by referring to the data in Table 2 (Appendix), and following the Poiseuille flow principle.

The cerebral vascular bed (approximated by dotted lines in Fig. 1b) was lumped as an inductor and a nonlinear resistor coupling. The inductor was used to damp the highly pulsatile arterial flow, while the nonlinear resistor was used to regulate the CBF through the following simple equation:

$$R_t = \left(1 + \frac{P_t - P_n}{P_n}\right) R_n \tag{1}$$

where R_t is the transient resistance of the nonlinear resistor, P_t is the pulsatile arterial pressure. P_n is the normal mean blood pressure (∼100 mmHg), R_n is the resistance functioning at a normal pressure range (80–100 mmHg). Since R_t depends on the difference between the mean and transient blood pressure $(P_t - P_n)$, it becomes larger when $P_t > P_n$, and thus resist the increased perfusion pressure to maintain a relatively steady blood flow, and vice versa. Consequently autoregulation is mimicked in this simple mechanism.

Overall, the circuit contains 49 electronic components, among which 42 resistors represent cerebral arteries, 5 resistors represent veins and a resistor/inductor couple to represent the vascular bed. The electrical analog model was implemented using the SimPowerSystems toolbox within SimuLink of Matlab (MathWorks, Natick, MA, USA). More details of the electrical circuit are provided in the Appendix.

2.3 *One-Dimensional (1D) Model*

The 1D formulation for the blood flow equations consists of three equations, i.e., the mass and momentum conservation equations, and an empirical arterial wall equation that describes the nonlinear elasticity of arterial wall in response to pulsatile pressures [3, 4, 7]. This can be written as:

$$\begin{aligned} \frac{\partial A}{\partial t} + \frac{\partial Q}{\partial x} &= 0 \\ \frac{\partial Q}{\partial t} + \frac{\partial (Q^2/A)}{\partial x} + \frac{A}{\rho}\frac{\partial p}{\partial x} &= -\frac{2\pi \nu R}{\sigma}\frac{Q}{A} \\ p - p_{ext} &= \frac{\sqrt{\pi} E h}{(1-\sigma^2 A_0)}(\sqrt{A} - \sqrt{A_0}) \end{aligned} \tag{2}$$

where A, Q, p are the cross-sectional area, the flow rate and pressure in a vessel, respectively. p_{ext} is the external pressure. A_0 is the cross-sectional area under no blood pressure. E, $\sigma (= 0.5)$ and h are the Young's modulus, Poisson's ratio, thickness of the arterial wall, respectively.

The equation system (2) is solved using an in-house developed flow solver. In brief, the system was numerically solved using a MacCormack finite difference method. Furthermore, a bifurcation model is used to predict flow distribution across vessel branches. The initial velocity and pressure at the arterial segments are 0 mm/s and 10.6 kPa (80 mmHg), respectively. The spatial and temporal step of the finite difference grid is set as 1 mm and 0.1 ms for numerical stability. The physiological pulsatile pressure computed from the 0D model is prescribed from the inlet/outlet of the arterial tree. For numerical details such as the time stepping scheme, the stability criteria, etc., we refer the interested reader to [7].

We use the cerebral blood vessels digitised from MRI images, available in [7], as shown in Fig. 2. In Fig. 2a the main cerebral arteries are shown in the maximum intensity projection (MIP) image of the MRI sequence. In Fig. 2b the main arteries of the CoW are shown. For this subject, the A1 segment of the left ACA is not

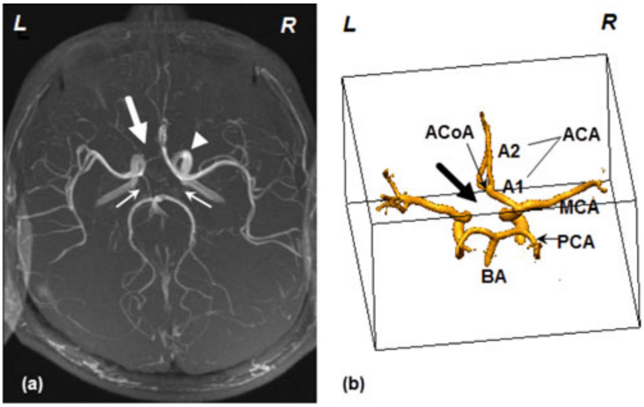

Fig. 2 Main branches of the CoW (note that A1 segment of the left ACA is occluded)

present in the image, implying an undeveloped segment in CoW. In the 1D model, we will simulate the blood flow at the right ICA, MCA and ACA.

3 Results

3.1 *Baseline 0D model*

Assuming an anatomically complete CoW and healthy blood pressure/flow conditions in an adult man, we firstly solved the blood flow in the whole cerebral vasculature over 50 cardiac cycles with the 0D model. The flow rate and blood pressure at several key sites of CoW, i.e., the ICA, MCA and ACA are shown in Fig. 3. It can be seen that blood flows in these large cerebral arteries are pulsatile and they have a similar pressure profile (75–115 mmHg). The pressure drop in large arteries is small due to small resistances in them (Fig. 3, upper panel). Also note that there is a small flow rate ($\sim$40 mL/min) (not shown in Fig. 3) in the posterior communicating artery (PCoA) which connects the anterior circulation (supplied by CA) and the posterior circulation (supplied by VA). This suggests a pressure gradient exists between the two regions.

The total blood supply to the brain (the sum of flow rates through the left and right ICAs and VAs) was $\sim$660 mL/min, close to the 700 mL/min theoretical CBF (i.e., 15% of cardiac output). In particular, the flow rate to the anterior circulation was 460 mL/min ($\sim$70% of the CBF), as opposed to 200 mL/min to the posterior circulation, consistent with clinical observations and model studies for normal subjects [5, 9]. Such comparisons are shown in Table 1.

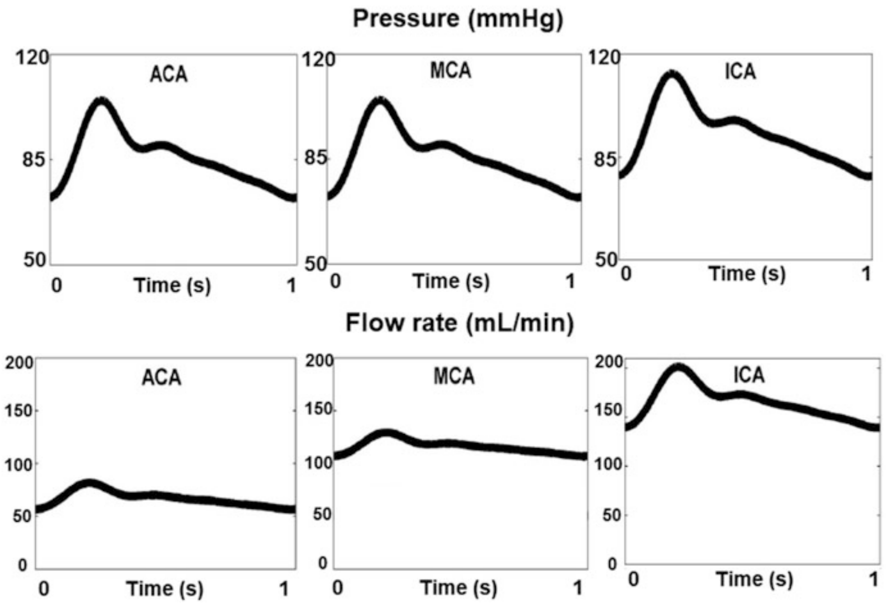

Fig. 3 Temporal blood pressure and flow rate profiles at key sites of the CoW (ICA, ACA and MCA)

Table 1 Distribution of CBF in anterior and posterior circulation

Vessel name	Flow rate		% of CBF	
	Literature [9]	Our model	Literature [5]	Our model
ACA	136	152	20.2	28
MCA	254	230	57.7	42
PCA	79	160	22.2	30

3.2 *The Autoregulation Model for CBF*

To demonstrate the effective pressure range in which autoregulation operates under, we designed an artificial pressure waveform shown in Fig. 4a, where phases I, III and V represented the normal blood pressure range of 80–120 mmHg (100 mmHg mean). In phase II there was a step decrease to 50–90 mmHg (mean 70 mmHg) to represent a hypotensive condition, and in phase IV there was a step increase to 130–170 mmHg (mean 150 mmHg) to represent hypertension. The full blood pressure range (50–170 mmHg) mimics the wide pressure deviations that may be effectively regulated. The computed flow rate waveforms without autoregulation are shown in Fig. 4b. It can be seen that this flow waveform follows that of the pressure waveform,

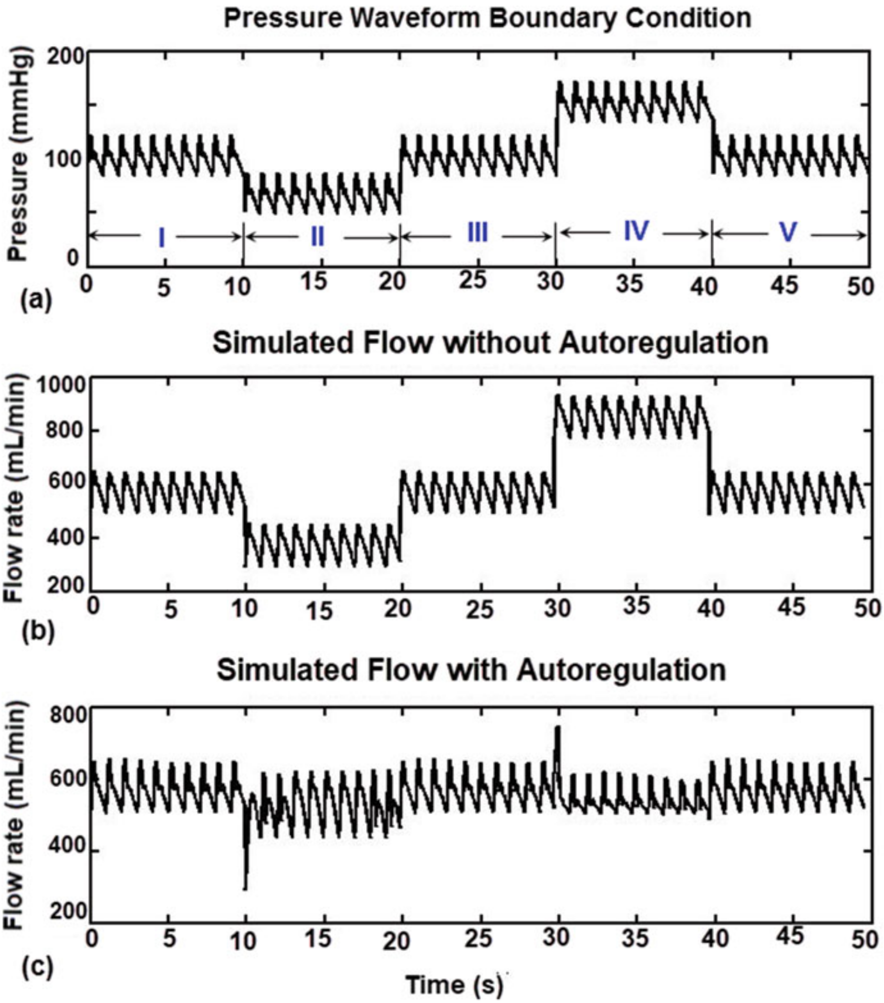

Fig. 4 (**a**) The artificially designed pressure waveform at the heart; (**b**) The simulated CBF without autoregulation; (**c**) With autoregulation, the CBF was relatively stable at approximately 590 mL/min in both hypotensive and hypertensive phases

which is not physiologically desirable because a relatively constant flow rate should be maintained. With the autoregulation mechanism introduced, as shown in Fig. 4c, the flow rates are able to recover from an initial oscillation and maintain a relatively stable flow at approximately 600 mL/min.

In Fig. 4c there appears to be changes in the flow waveform amplitude after a step pressure change, i.e., the amplitude becomes wider under hypotension, whereas it becomes more narrow under hypertension. The physiological relevance of these phenomena requires further investigation. However it has been shown that the flow pulsatility does have a variation with a pose change [3]. Also can be noticed are the flow rate spikes immediately after step pressure changes ($t = 10\,\text{s}, 30\,\text{s}$). Although these spikes were caused by numerical oscillations in response to a sharp pressure change, this phenomenon coincides with the transcranial Doppler recordings reported in [10], where a small time lag of approximately 3 s is required for the autoregulation to take effect.

3.3 Blood Flow in an Incomplete CoW: A Hybrid 0D–1D Model

For the subject-specific CoW shown in Fig. 2, where the left A1 segment is missing, the flow rate (mL/min) simulated from the 0D model is shown in Fig. 5. It can be seen that when the left A1 segment is absent, the flow in the anterior communicating artery (ACoA) is critical to supply the left ACA, whereas the flow in the ACoA can be minimal (zero) if the left A1 is patent (Fig. 5a). For this subject, since the right A1 segment supplies blood to both the left and right ACA A2 segments (Fig. 5b), the right A1 segment needs to accommodate a much higher (two fold) flow rate (Fig. 5c). This leads to vascular remodelling of the right A1 segment so that this vessel is dilated.

To investigate this subtle cerebral flow scenario further, the flow in the ICA, MCA and ACA is simulated using the 1D flow model introduced in Sect. 2.3. The boundary conditions are the inlet and outlet pressures to induce the pressure gradient. Figure 6 (upper panel) represents the subject-specific case, i.e., when the left A1 segment is occluded, while Fig. 6 (lower panel) shows the pressure and flow rate when the CoW is complete and normal.

With a normal, complete CoW, the pressures at the left and right ACA A1 segment are almost identical, hence there is little pressure gradient in the ACoA segment to drive the flow. This is consistent with what we found from the 0D model

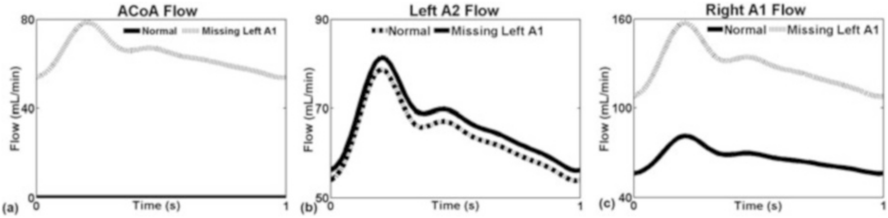

Fig. 5 Comparison of the blood flow rate with/without the A1 segment in CoW

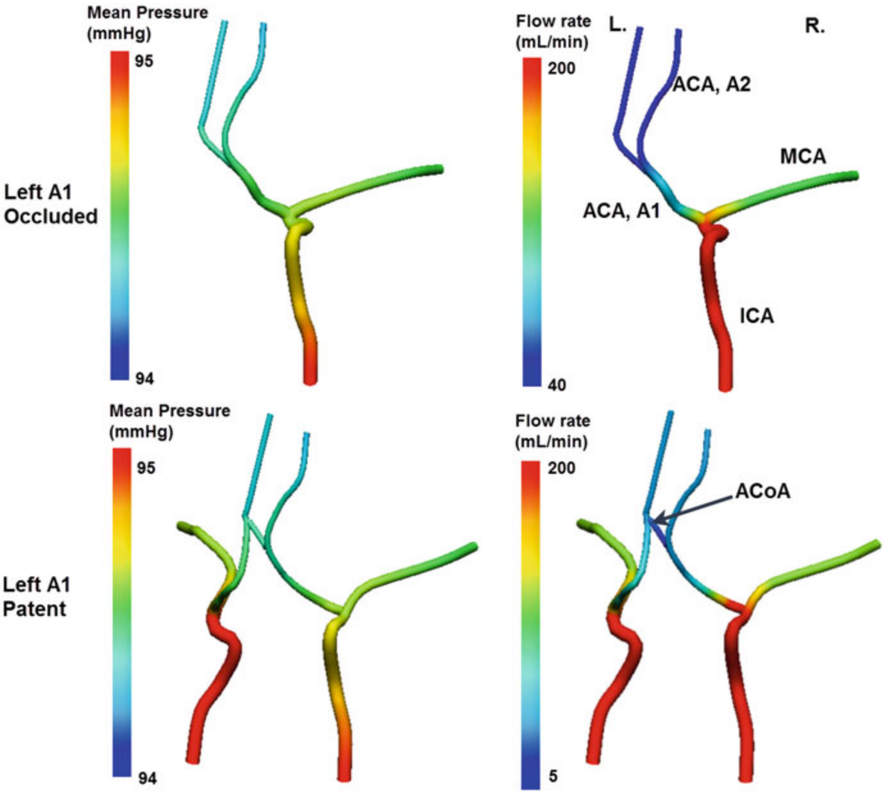

Fig. 6 Comparison of the blood flow rate with/without the A1 segment in CoW

(Fig. 5a). Vessel dilation can be observed in the ACA A1 segment (radius 2 mm vs 1.5 mm) when the left A1 segment is occluded, manifesting the vessel remodelling introduced above.

4 Discussion

In this paper we presented a hybrid 0D–1D model for the cerebral circulation and the flow in CoW. The 0D model retained the topological features of a generic cerebral vasculature, similar to that described in [9] but our model also included extracranial arteries efferent ECA. The computed blood pressure and flow rate profiles (Fig. 3) had a good agreement with that reported in literature. A simple model for autoregulation was implemented per Eq. (1) which served its role of regulating CBF under hypo- and hypertension scenarios. With the model we studied a subject-specific case, where the left ACA A1 segment was not present in the CoW. The corresponding cerebral circulation phenomena unsurprisingly yielded a higher flow rate in the right ACA A1 segment. This implies a lower resistance to flow, or a dilated arterial lumen in this segment, which was confirmed from the 1D model. Furthermore, while the little flow rate in the ACoA is the norm for a complete CoW, its role becomes critical in this subject-specific case with an incomplete CoW to convey blood supply from the right anterior brain to the left brain.

There are several limitations pertaining to the presented model. One such limitation is that the blood vessels in the 0D model are only modelled with resistors. The effects of compliance, which are an important property of large blood vessels, are not simulated. However, adding capacitors into the circuit would substantially increase the circuit complexity. Another limitation is that changing the resistance at any location downstream will have repercussions with the flows and pressures of every element prior.

There are several directions that the current model may be extended. Firstly, by altering the parameters of the electronic components in the circuit, which were designed for adult men, the modified model may be used to simulate the blood flow in children, which is undergoing in our group. Secondly, by altering the topology of the circuit we are able to apply the model to the research of cerebral circulation under other pathological conditions (e.g., arterial venous malformation) [9] per patient specific cerebral vascular anatomy, as we demonstrated in this work.

5 Conclusion

A hybrid 0D and 1D cerebral circulation model was proposed in this work. It seems that this model has potential in simulating various flow phenomena observed in surgical theatres and physiology laboratories.

Appendix

The electrical circuit of the 0D model is quite large. The diameters and lengths of the arteries and veins and their nominal resistance value in the circuit are listed in Table 2. The diagram of the posterior circulation is shown in Fig. 7 to illustrate the design of the posterior circulation and venous return.

Table 2 Nominal diameter and length of blood vessels and corresponding resistance in the model

Vessel name	Diameter (mm)	Length (mm)	Resistance (Ohm)
Arteries			
CCA	6.1	150[a]	425
ICA	4.0	60	600
VA	3.0	150	500
BA	4.0	35	300
MCA	3.3	21.1	1150
ACoA	1.0	25	2000
PCoA	1.0	13.5	1750
ACA(A1)	2.5	10.7	500
ACA(A2)	2.5	23.0	400
PCA(P1)	3.0	3.33	100
PCA(P2)	3.0	7.56	575
ECA Seg 1	3.2	30[a]	2500
ECA Seg 2	3	10[a]	1000
ECA Seg 3	2.8	10[a]	1000
ECA Seg 4	2.5	10[a]	1000
Temporal	2[a]	15[a]	1000
Maxillary	2[a]	15[a]	1000
Facial	2.5[a]	15[a]	1000
Occipital	2[a]	15[a]	1000
Lingual	2.5[a]	20[a]	2000
Auricular	1.5[a]	15[a]	1000
Veins			
IJV	7.2	750	10
EJV	4	500[a]	2500
SSS	15	500	50
Sigmoid sinus	7	350	50

Note: Vessel dimension data adopted from references [2–5, 7, 8]
[a] Estimated values

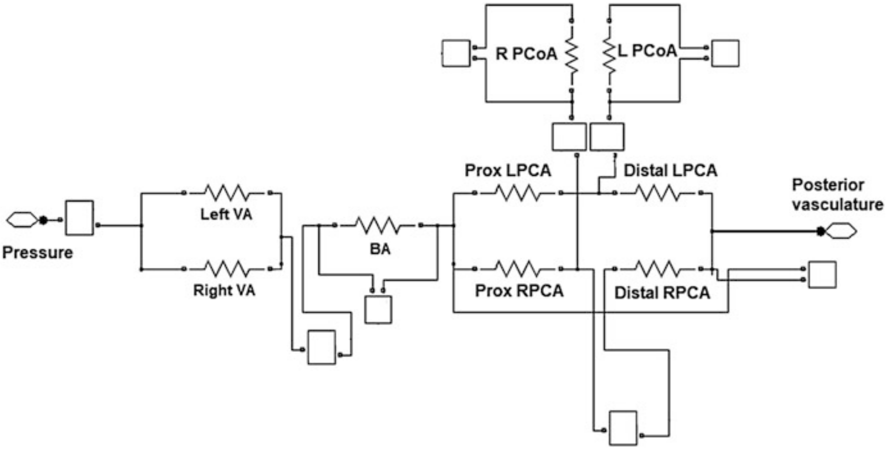

Fig. 7 Diagram for the circuit of the posterior circulation

Acknowledgements This project was partially supported by a seed grant (project number UOAX1702) from the Science for Technological Innovation programme of National Science Challenge of New Zealand.

References

1. Levick JR (2003) An introduction to cardiovascular physiology. Arnold, London.
2. Ursino M, Lodi CA (1997) A simple mathematical model of the interaction between intracranial pressure and cerebral hemodynamics. J Appl Physiol 82:1256–1269
3. Olufsen MS, Nadim A, Lipsitz LA (2002) Dynamics of cerebral blood flow regulation explained using a lumped parameter model. Am J Physiol Regul Integr Comp Physiol 282:R611–R622
4. Alastruey J, Parker KH, Peiro J, Sherwin SJ (2007) Modelling the circle of Willis to assess the effects of anatomical variations and occlusions on cerebral flows. J Biomech 40:1794–1805
5. Zagzoule M, Marc-Vergnes JP (1986) A global mathematical model of the cerebral circulation in man. J Biomech 19:1015–1022
6. Reymond P, Merenda F, Perren F, Rfenacht D, Stergiopulos N (2009) Validation of a one-dimensional model of the systemic arterial tree. Am J Physiol Heart Circ Physiol 297:H208–H222
7. Ho H, Mithraratne K, Hunter P (2013) Numerical simulation of blood flow in an anatomically-accurate cerebral venous tree. IEEE Trans Med Imaging 32:85–91
8. Alns MS, Isaksen J, Mardal K-A, Romner B, Morgan MK, Ingebrigtsen T (2007) Computation of hemodynamics in the circle of Willis. Stroke 38:2500–2505
9. Gao E, Young WL, Pile-Spellman J, Ornstein E, Ma Q (1998) Mathematical considerations for modeling cerebral blood flow autoregulation to systemic arterial pressure. Am J Physiol Heart Circ Physiol 274:H1023–H1031
10. Aaslid R, Lindegaard KF, Sorteberg W, Nornes H (1989) Cerebral autoregulation dynamics in humans. Stroke 20:4552

Removing Drift from Carotid Arterial Pulse Waveforms: A Comparison of Motion Correction and High-Pass Filtering

Emily J. Lam Po Tang, Amir HajiRassouliha, Martyn P. Nash, Andrew J. Taberner, Poul M. F. Nielsen, and Yusuf O. Cakmak

Abstract Non-invasive methods for estimating carotid artery (CA) pressure waveforms have been recently developed as a tool to detect heart abnormalities. Among non-invasive techniques, camera-based methods have the advantage of being non-contact, which enables measurements without applying external pressures to the artery. Camera-based methods measure skin deformation waveforms caused by arterial blood flow, which are assumed to have a similar shape to the pressure waveforms. Video recordings of the subject's neck are analysed to quantify skin deformations caused by the carotid pressure pulse. However, in practice, unrelated motion, such as the relative movements of the camera and the subject, or movements due to breathing, can confound the skin measurements. One of the primary effects of this error is seen in the form of signal drift, which can make it difficult to analyse the shape of the skin displacement waveform. In this paper, we have investigated and compared two methods for removing the signal drift. One is to correct for the motion in the captured videos of the neck, and the second method is to use a high-pass wavelet filter. The results showed that, although both methods could reduce the signal drift, they had dissimilar effects on the shape of the CA displacement waveforms. The high-pass wavelet filter seemed to preserve the original measured shape of the CA displacement waveforms better than the motion-correction method. However, in this study, it was not possible to quantify the performance since the true shape of the CA displacement waveforms was not known.

E. J. Lam Po Tang · A. HajiRassouliha (✉)
Auckland Bioengineering Institute (ABI), The University of Auckland, Auckland, New Zealand
e-mail: elam872@aucklanduni.ac.nz; amir.hajirassouliha@auckland.ac.nz

M. P. Nash · P. M. F. Nielsen
Auckland Bioengineering Institute, University of Auckland, Auckland, New Zealand

A. J. Taberner
Auckland Bioengineering Institute (ABI), The University of Auckland, Auckland, New Zealand

Department of Engineering Science, The University of Auckland, Auckland, New Zealand

Y. O. Cakmak
Department of Anatomy, University of Otago, Dunedin, New Zealand

M. P. Nash et al. (eds.), *Computational Biomechanics for Medicine*,
https://doi.org/10.1007/978-3-030-15923-8_9

Keywords Carotid artery · Pressure · Motion artefacts · Subpixel image registration

1 Introduction

Cardiovascular disease (CVD) is one of the most common causes of death [1]. Early diagnosis of CVD is essential to plan an effective treatment. However, often the symptoms of CVD do not arise until late stages of the disease [2]. Hence, methods and tools that can help early diagnosis of CVD are valuable to prevent heart failure. There are several well-studied methods of monitoring heart activities. Echocardiography is often used to diagnose problems with heart mechanics. Other common clinical approaches to detect heart and valvular diseases include: cardiac magnetic resonance imaging (MRI), estimation of pulmonary arterial pressures using catheterisation, auscultation of cardiac sounds, and assessing the shape of the CA pressure waveforms [3]. The shape of the CA pressure waveform can indicate several heart pathologies and valvular diseases [4]. The CA has a pressure waveform with two peaks in healthy normal subjects (Fig. 1). The abnormalities of the shape of CA pressure waveform can be a sign of heart failure. Diseases that can be diagnosed using CA pressure waveforms include hypertrophic obstructive cardiomyopathy (Fig. 1), aortic stenosis, and aortic regurgitation.

The traditional clinical method of determining the pressure waveforms is to insert a pressure sensor into the CA via catheterisation. Catheterisation is an invasive and expensive method. A non-invasive method of measuring CA pressure waveforms is to use a pulsed-Doppler ultrasound device. To record images, the ultrasound probe of the device is pressed against the neck. One limitation of this method is that the applied force may alter the shape of the waveforms. Another limitation of the use

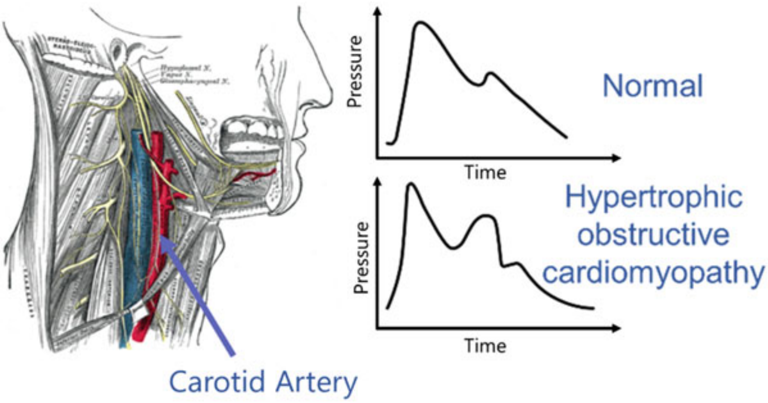

Fig. 1 The carotid artery and carotid arterial pressure waveforms

of ultrasound devices and catheterisation is the need for specially trained clinicians and operators [5].

Recently, non-contact camera-based methods have been developed to measure CA displacement waveforms caused by the pulsation of the skin of the neck. The camera-based methods rely upon the assumption that skin displacements on the neck follow the same pattern as the CA pressure waveform. Photoplethysmographic (PPG) imaging is the most common camera-based technique used [6, 7]. PPG systems use changes in the light intensity of the infrared wavelength to infer the blood flow inside the CA. These methods require special preparation of the light source and illumination [6, 7]. Another camera-based approach is to use subpixel image registration to measure deformation of the skin on the neck from video recordings. This method was first proposed by our group for measuring CA displacement waveforms [8]. In this approach, the image is divided to smaller square subimages (typically 64 pixel × 64 pixel), and subpixel relative shifts are measured between each of the subimages, from the initial (reference) image of the neck to the image for which pulsation of the CA has caused skin deformations. The use of subpixel image registration makes it possible to directly measure skin deformation, and hence to accurately estimate the displacement waveforms. In our technique, we took advantage of our precise and sensitive subpixel image registration algorithm that uses phase-based Savitzky–Golay gradient-correlation (P-SG-GC) [9]. This algorithm is capable of measuring skin deformations using only intrinsic skin surface features [8, 10] allowing direct measurement of CA displacement waveforms from video recordings of the neck without the need for special preparation of the skin.

Camera-based techniques for measuring CA displacement waveforms have many advantages, such as being non-invasive and non-contact, but there is one major challenge: the relative motion between the subject's neck and the camera can confound the analysis. Such motion often happens due to movement of the subject, which can be difficult to control. A primary assumption for all of the camera-based techniques is that the location of the region of interest (ROI) on the neck does not move from frame to frame during the recording. Unwanted movement can therefore compromise the accuracy of the measurement. An unintended consequence of movement is signal drift in CA displacement waveforms. Such signal drift can cause issues with diagnosis of CVD since both the shape and the amplitude of the CA waveform contain important information.

In this study, we investigated two methods of reducing the drift of CA displacement waveforms. One method was to correct for the motion of the ROI in the recorded videos and the second method was to apply a high-pass filter designed using Daubechies wavelets [11]. The effects of these two methods on reducing the signal drift of CA displacement waveforms were quantified in five healthy subjects. To extract the CA displacement waveforms, we used the camera-based method developed by HajiRassouliha et al. [8]. While this method is based on subpixel image registration, the methods we used to reduce waveform drift are general, and could be used for any other camera-based method designed to extract CA displacement waveforms.

2 Method

The camera rig, illustrated in Fig. 2 and described in [8], was used to record videos from the neck of subjects close to the area of pulsation. This device consists of a Flea 3 USB3 camera (FL3-U3-13Y3M-C), a light emitting diode (LED) to provide illumination, and a custom-built camera rig to hold the camera and the LED. Videos were captured at 90 frames per second (fps) with a resolution of 1280 pixel × 1024 pixel. The pixel size of the recordings was approximately 80 µm.

Five healthy subjects were selected for the measurements of CA displacement waveforms. This study was approved by the Otago University Human Ethics Committee (reference number D17/127, category B, 4/4/2017). All experiments were performed in accordance with the guidelines and regulations of the Otago University Human Ethics Committee. The locations of each region of interest (ROI) on the video recordings of the subjects were manually selected. The ROIs were divided into subimages of 64 pixel × 64 pixel in size with an overlap of 49 pixel between subimages (Fig. 3) (i.e. a step size of 15 pixel between control points). The subimage size and the overlap between subimages enabled measurement of localised deformations of the skin caused by the CA pulsation in a relatively dense grid of points on the images.

Two sets of measurements were performed for each of the five subjects. In the first set the CA displacement waveforms were extracted from the original (uncorrected) videos, and in the second set the videos were motion-corrected prior to measuring CA displacement waveforms. The same method was used to extract CA displacement waveforms from both sets of measurements.

The method of measuring CA displacement waveforms uses the P-SG-GC algorithm [9] to measure displacements of every subimage of each frame of the captured video with respect to the corresponding subimage of the first image. A

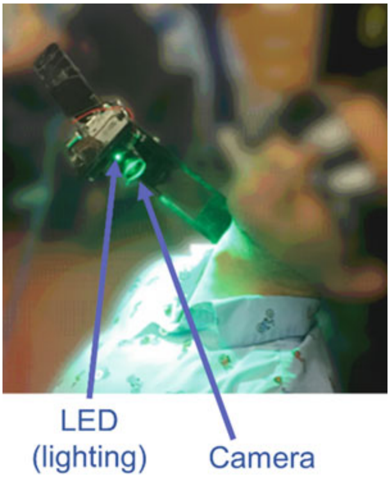

Fig. 2 The device used to quantify carotid pulse displacements waveforms

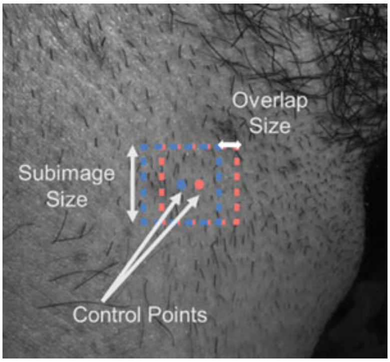

Fig. 3 Two sample subimages on the ROI for measuring the CA deformation waveforms

control point was defined at the centre of each subimage, and the locations of all control points were tracked and used to determine the displacements of the subimages between frames.

2.1 Motion Correction

Motion correction was performed on the videos using the method described by HajiRassouliha et al. in [12]. In this method, the images of the object are divided into subimages, and displacements of the control points are measured from the subimages following movement of the object. The displacements are used in a nonlinear least-squares optimisation method to define an affine transform matrix that maps the second image to the initial image. This transform then is applied to the image to map it back to the coordinates of the reference image, thereby correcting for relative motion between that image and the first image. The motion-correction method of HajiRassouliha et al. [12] was used in this application with a subimage size of 128 pixel × 128 pixel and a step size of 50 pixel (an overlap of 78 pixel between subimages). This method was applied to all of the video recordings from five subjects of this study to correct for unwanted motions in the videos.

The measured CA displacement waveforms for the original videos and motion-corrected videos were plotted and compared to illustrate the signal drifts before and after the correction.

2.2 High-Pass Filtering

Signal drift is a form of offset in the spatial domain. In the frequency domain, the signal offset (the DC component) of the signal is present in the low-frequencies. Therefore, a high-pass filter can remove the drift by attenuating the low-frequency components of the signal. Here, we applied a high-pass filter to the measured CA

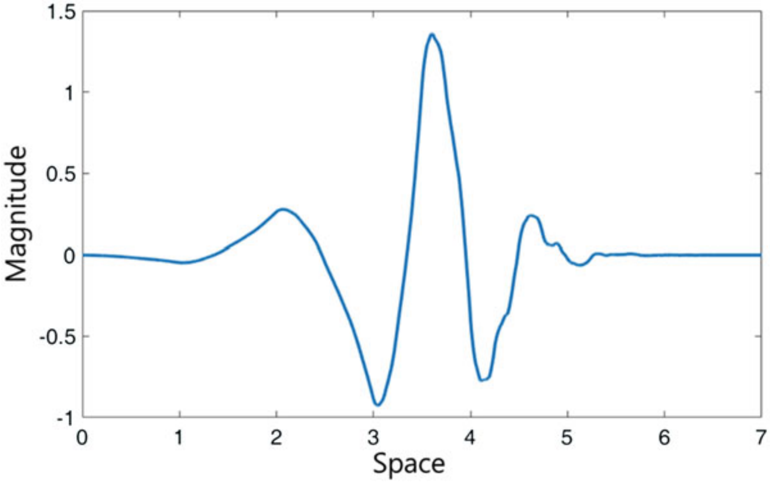

Fig. 4 The spatial domain representation of the Daubechies wavelet filter of order four

displacement waveforms in order to remove the drift. The high-pass filter used was designed based on Daubechies wavelets [11]. One advantage of using wavelet filters compared to traditional high-pass filters is their ability to capture the transient features of signals. The high-pass Daubechies wavelets filters used were of order four and had seven levels of decomposition (refer to [13, 14] for the definition of wavelet decomposition levels). The order and the decomposition level of wavelet filters were selected based on the signal shape and the frequency range of the waveform data. The Daubechies wavelets of order four (Fig. 4) are commonly used in processing biological signals, such as body surface potentials [15] and EEG signals [16, 17], because they have similar signal shapes to biological signals in the spatial domain (Fig. 4). This similar shape helps the wavelet filters to keep the details of the signal better than traditional frequency domain filters.

Since the sampling frequency of our recorded videos was 90 Hz (i.e. 90 fps), seven levels of decomposition were associated, with a threshold frequency of $\frac{90\text{ Hz}}{2^{7+1}} \approx 0.35$ Hz for the highest level of decomposition. Therefore, by applying this wavelet filter, the frequency components smaller than 0.35 Hz were removed from the measured CA displacement waveforms. The 0.35 Hz threshold was chosen based on visually observing the filtered CA displacement waveforms and ensuring that the high frequency features of the signal were preserved. This threshold provided a good compromise between removal of the signal drift and preservation of the signal shape in our recordings.

3 Results

The CA displacement waveforms in five subjects measured from the original videos using the P-SG-GC algorithm [9] are illustrated by the blue plots in Fig. 5. Upon visual inspection, there is a clear drift in the CA displacement waveforms from the original videos. The videos were then motion-corrected using the method of HajiRassouliha et al. [8], and were used to measure CA displacement waveforms. The orange plots in Fig. 5 show how motion correction of the videos has reduced the signal drift. Nevertheless, the shape of the signals has changed in some parts of the output signals, such as subject 1 and subject 2 where the waveforms from motion-corrected videos (orange plots in Fig. 5) have smaller peaks compared to the waveforms from the original videos (blue plots in Fig. 5). The green plots in

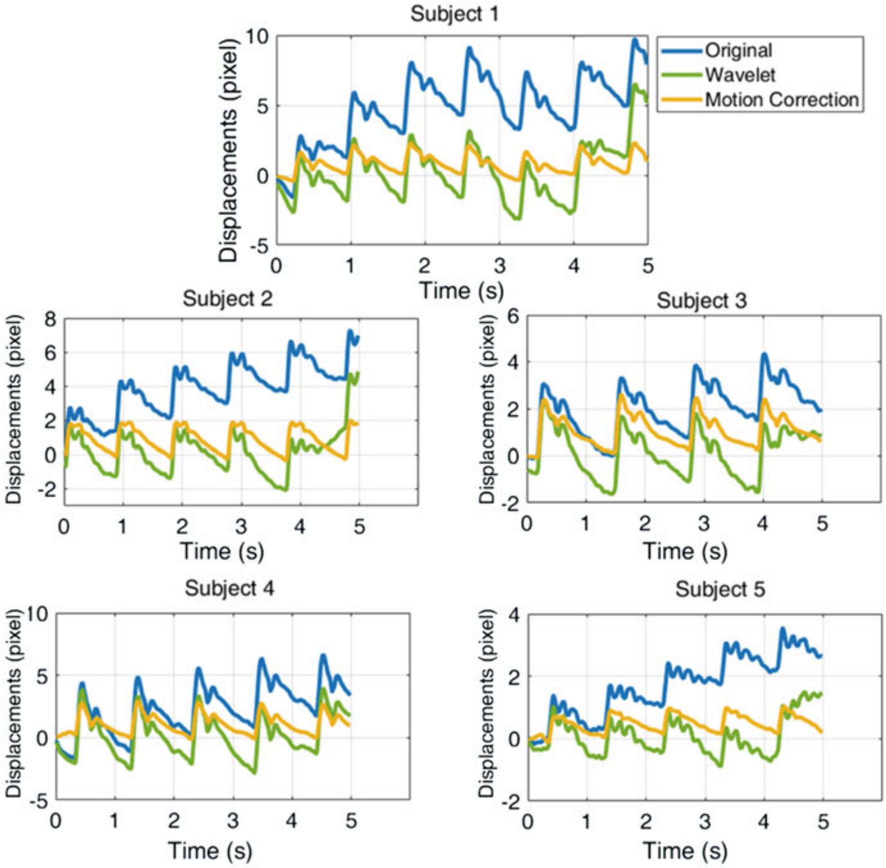

Fig. 5 Measured waveforms from the original video (blue), the motion-corrected videos (green), and signals filtered using high-pass Daubechies wavelet filters for each subject (orange)

Fig. 5 show the effect of filtering the measured CA displacement waveforms (blue plots in Fig. 5) using high-pass Daubechies wavelets. The filtering of the signal was also successful in removing the signal drift in most cases. However, as shown in Fig. 5, the shapes of the filtered signals were different from those in the original signals (blue plots) in some parts, such as the duration between 4.5 s and 5 s in subjects 3 and 5.

4 Discussion and Conclusion

The measurement of CA displacement waveforms from original videos showed that relative movements of the camera or the subject causes signal drift (blue plots in Fig. 5). We tested two approaches to reduce the signal drift. In the first approach, the source of the drift (i.e. relative movements) was targeted and was removed from the videos using a motion-correction method. In the second approach, the effects of drift were removed from the CA displacement waveforms using a high-pass Daubechies wavelet filter. While both these methods could successfully reduce the majority of the signal drift, they also changed the shape of the waveforms seen in original signal (Fig. 5). It is difficult to evaluate which of these two methods performed better since there is no ‘gold standard’ for the actual shape of the signal.

An important difference between the analyses using the motion-correction method and that using the high-pass filtering method was the material points used to extract the waveforms (Fig. 3). The filtering approach is a processing step applied to the output of measurements from the original videos. Even though the control points are fixed from frame to frame, the material points associated with the reference image’s control points may not remain at these locations due to movements unrelated to CA pulsations. The drift is removed from the measured waveforms of the fixed control points. On the other hand, the motion-correction method updates the coordinate system of each frame according to the measured unrelated motion between the frames. Therefore, if the motion-correction method performs successfully, the location of the material points is updated to match the location of the control points. This facilitates adjustment of the images to compensate for unrelated movements of the subject in order to only measure skin deformations from the pulsation on the neck. This will result in a more accurate measurement of skin displacements caused by the CA pulsations.

An advantage of using the filtering approach compared to the motion-correction method is its lower computational cost. However, the computational costs are not critically important for this application. Despite being effective for the five subjects we tested, both of these methods have their own limitations. The motion-correction method cannot deal with frame to frame movements larger than 20 pixel. On the other hand, the high-pass filtering does not help to perform more accurate measurement of the CA displacement waveforms. Filtering only removes some of the low-frequency components of the already measured waveforms, without maintaining focus on area of the pulsation. In future work, the effects of some other filtering approaches on more subjects will be investigated. Furthermore, synthetic data will be generated to provide a gold standard with which to evaluate the performance of different approaches.

References

1. Townsend N, Wilson L, Bhatnagar P, Wickramasinghe K, Rayner M, Nichols M (2016) Cardiovascular disease in Europe: Epidemiological update 2016. Eur Heart J 37:3232–3245
2. Kasznicki J, Drzewoski J (2014) Heart failure in the diabetic population – pathophysiology, diagnosis and management. Arch Med Sci 3:546–556
3. DeSilva, R (2013) Heart disease. Biographies of disease. Greenwood, Oxford. https://books.google.co.nz/books?id=JgWb1QzudRMC
4. Maganti K, Rigolin VH, Sarano ME, Bonow RO (2010) Valvular heart disease: diagnosis and management. Mayo Clin Proc 85:483–500
5. O'Rourke MF, Pauca A, Jiang X-J (2001) Pulse wave analysis. Br J Clin Pharmacol 51:507–522
6. Amelard R, Hughson RL, Greaves DK, Pfisterer KJ, Leung J, Clausi DA, Wong A (2017) Non-contact hemodynamic imaging reveals the jugular venous pulse waveform. Sci Rep 7:1–10
7. Moco AV, Mondragon LZ, Wang W, Stuijk S, De Haan G (2017) Camera-based assessment of arterial stiffness and wave reflection parameters from neck micro-motion. Physiol Meas 38:1576–1598
8. HajiRassouliha A, Lam Po Tang E, Nash MP, Taberner AJ, Nielsen PMF, Cakmak YO (2017) Quantifying carotid pulse waveforms using subpixel image registration. In: Computational biomechanics of medicine XII workshop, MICCAI
9. HajiRassouliha A, Taberner AJ, Nash MP, Nielsen PMF (2018) Subpixel phase-based image registration using Savitzky–Golay differentiators in gradient-correlation. Comput Vis Image Underst 170:28–39
10. HajiRassouliha A, Taberner AJ, Nash MP, Nielsen PMF (2016) Subpixel measurement of living skin deformation using intrinsic features. In: Proceedings of computational biomechanics of medicine XI workshop, MICCAI
11. Daubechies I (1988) Orthonormal bases of compactly supported wavelets. Commun Pure Appl Math 41:909–996
12. HajiRassouliha A, Taberner AJ, Nash MP, Nielsen PMF (2017) Motion correction using subpixel image registration. In: Proceedings of international workshop on reconstruction and analysis of moving body organs, MICCAI, pp 14–23
13. Mallat SG (1989) A theory for multiresolution signal decomposition: the wavelet representation. IEEE Trans Pattern Anal Mach Intell 11:674–693
14. Lei L, Wang C, Liu X (2013) Discrete wavelet transform decomposition level determination exploiting sparseness measurement. Int J Electr Comput Energy Electron Commun Eng 7:691–694
15. HajiRassouliha A, Amoon M, Doostmohammadi MH, Sadr A, Ayatollahi A, Rezairad GA (2008) Comparison of using different types of wavelet or FFT for de-nosing of body surface potential signals. In: 2008 third international conference on broadband communications, information technology & biomedical applications. IEEE, pp 233–238
16. Subasi A (2007) EEG signal classification using wavelet feature extraction and a mixture of expert model. Expert Syst Appl 32:1084–1093
17. Amin HU, Malik AS, Ahmad RF, Badruddin N, Kamel N, Hussain M, Chooi W-T (2015) Feature extraction and classification for EEG signals using wavelet transform and machine learning techniques. Australas Phys Eng Sci Med 38:139–149

Rapid Blood Flow Computation on Digital Subtraction Angiography: Preliminary Results

George Bourantas, Grand Roman Joldes, Konstantinos Katsanos, George Kagadis, Adam Wittek, and Karol Miller

Abstract In this study, we simulate blood flow in complex geometries obtained by digital subtraction angiography (DSA) images. We represent the flow domain by a set of irregularly distributed nodes or uniform Cartesian embedded grid, and we numerically solve the non-stationary Navier–Stokes (N-S) equations, in their velocity–vorticity formulation, by using a meshless point collocation method. The spatial derivatives are computed with the discretization corrected particle strength exchange (DC PSE) method, a recently developed meshless interpolation method. For the transient term a fourth order Runge–Kutta time integration scheme is used.

Keywords Blood flow · Computational fluid dynamics · Meshless · Navier–Stokes · Explicit · Runge–Kutta

---

G. Bourantas (✉)
Intelligent Systems for Medicine Laboratory, The University of Western Australia, Perth, WA, Australia
e-mail: george.bourantas@uwa.edu.au

K. Katsanos
The Department of Interventional Radiology, Patras University Hospital, School of Medicine, Rion, Greece

The Department of Interventional Radiology, Guy's and St. Thomas' Hospitals, NHS Foundation Trust, King's Health Partners, London, UK

G. Kagadis
Department of Medical Physics, School of Medicine, University of Patras, Rion, Greece

Department of Imaging Physics, The University of Texas MD Anderson Cancer Center, Houston, TX, USA

K. Miller · G. R. Joldes · A. Wittek
Intelligent Systems for Medicine Laboratory, Department of Mechanical Engineering, The University of Western Australia, Perth, WA, Australia

M. P. Nash et al. (eds.), *Computational Biomechanics for Medicine*,
https://doi.org/10.1007/978-3-030-15923-8_10

1 Introduction

Rapid assessment of blood flow in cerebral vascular diseases during neurovascular intervention is important for medical treatment planning. Unfortunately, estimation of local hemodynamic conditions in a given patient relies on the physicians' subjective judgment of dynamic contrast agent distribution patterns observed with digital subtraction angiography (DSA).

Current DSA technology used in clinical practice cannot display volumetric blood flow rates. However, recent advancements, that include DSA with dual panel detector combined with deconvolution analysis, are beginning to provide metrics of cerebral blood flow, cerebral blood volume and mean transit time. The major limitation of these noninvasive imaging techniques is the lack of temporal resolution.

Computational fluid dynamics (CFD) simulations provide quantitative assessment of the local hemodynamics. After the flow domain (vessel lumen) is segmented (usually with an efficient segmentation and edge detection algorithm), clinically relevant flow parameters can be computed. For the simulation results to be potentially useful in clinical practice, it is crucial to obtain the flow field fast and accurately. This can be achieved using 'image as a model' concept previously proposed in the context of creation of patient-specific computational biomechanics models for computing organ deformations for image guide surgery by Zhang et al. [1]. Using this concept, patient-specific computational grids are automatically generated directly from medical images.

In this study, the image as a model concept is implemented by representing the flow domain using a set or irregularly distributed nodes and uniform Cartesian embedded grid. The non-stationary Navier–Stokes equations, in their velocity–vorticity formulation are solved, using a meshless point collocation method. The spatial derivatives are computed with the recently developed meshless interpolation method referred to discretization corrected particle strength exchange (DC PSE) [2]. For the transient term a fourth order Runge–Kutta time integration scheme is used.

2 Methods

2.1 Governing Equations

We consider the blood flow as non-stationary, viscous, laminar flow of an incompressible fluid. The governing equations for such flow are based on conservation of mass and momentum. The relevant non-dimensional form of the stream function–vorticity (ψ-ω) formulation [3] is

$$\frac{\partial \omega}{\partial t} + \frac{\partial \psi}{\partial y}\frac{\partial \omega}{\partial x} - \frac{\partial \psi}{\partial x}\frac{\partial \omega}{\partial y} = \frac{1}{\mathrm{Re}}\nabla^2 \omega \tag{1}$$

$$\nabla^2 \psi = -\omega \tag{2}$$

where *Re* is the Reynolds number. The stream function ψ is used to compute the velocity components u and v, using the following equations:

$$u = \frac{\partial \psi}{\partial y} \tag{3a}$$

$$v = -\frac{\partial \psi}{\partial x} \tag{3b}$$

We numerically solve Eqs. (1) and (2), defined in the spatial domain Ω with boundary $\partial\Omega$, having initial conditions

$$\boldsymbol{u} = \boldsymbol{u}_0 \tag{4}$$

$$\omega = \omega_0 = \nabla \times \boldsymbol{u}_0, t = 0 \tag{5}$$

and boundary conditions

$$\boldsymbol{u} = \boldsymbol{u}_{\partial\Omega} \tag{6a}$$

$$\omega = (\nabla \times \boldsymbol{u}_0)_{\partial\Omega} \tag{6b}$$

2.2 Meshless Discretization: Discretization Corrected Particle Strength Exchange Method

We solve the partial differential equations (PDEs) governing the blood flow using the discretization corrected particle strength exchange (DC PSE) method. The DC PSE was introduced in [4] as a Lagrangian based particle solution method. The authors in [2] have reformulated DC PSE method to work in the Eulerian framework required for applications in fluid flow. For completeness of the presentation, we provide a brief description of the particle strength exchange (PSE) operators and the DC PSE interpolation method below.

2.2.1 Particle Strength Exchange (PSE) Operators

The particle strength exchange (PSE) method makes use of kernels to create approximate differential operators that guarantee the conservation of particle strength in particle–particle interactions. It was first introduced in 1989 by Degond and Mas-Gallic [5] for diffusion and convection–diffusion problems. Based on this initial work, Eldredge et al. [6] developed a framework for approximating arbitrary derivatives. In general, a PSE operator $Q^{\boldsymbol{\beta}}f(\boldsymbol{x})$ for approximating the derivative $D^{\boldsymbol{\beta}}f(\boldsymbol{x})$ has the form

$$Q^{\boldsymbol{\beta}} f\left(\boldsymbol{x}\right) = \frac{1}{\varepsilon^{|\boldsymbol{\beta}|}} \int \left(f\left(\boldsymbol{y}\right) \mp f\left(\boldsymbol{x}\right)\right) \eta_{\varepsilon}^{\boldsymbol{\beta}}\left(\boldsymbol{x} - \boldsymbol{y}\right) d\boldsymbol{y} \tag{7}$$

with $\eta_{\varepsilon}^{\boldsymbol{\beta}} = \eta^{\boldsymbol{\beta}}\left(x/\varepsilon\right)/\varepsilon^{d}$ being a scaled kernel of radius ε and, d being the number of dimensions. For conservation reasons, the sign in Eq. (7) is negative when $|\boldsymbol{\beta}|$ is even and positive when $|\boldsymbol{\beta}|$ is odd, with $\boldsymbol{\beta}$ a multi-index [5]. The challenge is to find a kernel $\eta_{\varepsilon}^{\boldsymbol{\beta}}$ that leads to accurate approximations for $D^{\boldsymbol{\beta}}$. To find such kernels for arbitrary derivatives, the idea in [6] is adopted, starting from the Taylor expansion of a function $f(\boldsymbol{y})$ about a point $\boldsymbol{x}$:

$$f\left(\boldsymbol{y}\right) = f\left(\boldsymbol{x}\right) + \sum_{|\boldsymbol{a}|=1}^{\infty} \frac{1}{\boldsymbol{a}!}\left(\boldsymbol{y} - \boldsymbol{x}\right)^{\boldsymbol{a}} D^{\boldsymbol{a}} f\left(\boldsymbol{x}\right) \tag{8}$$

By introducing the continuous $\boldsymbol{\alpha}$-moments

$$M_{\boldsymbol{a}} = \int \left(\boldsymbol{x} - \boldsymbol{y}\right)^{\boldsymbol{\alpha}} \eta^{\boldsymbol{\beta}}\left(\boldsymbol{x} - \boldsymbol{y}\right) d\boldsymbol{y} = \int z^{\boldsymbol{\alpha}} \eta^{\boldsymbol{\beta}}\left(z\right) dz \tag{9}$$

we obtain

$$Q^{\boldsymbol{\beta}} f\left(\boldsymbol{x}\right) = \frac{(-1)^{|\boldsymbol{\beta}|}}{\boldsymbol{\beta}!} M_{\boldsymbol{\beta}} D^{\boldsymbol{\beta}} f\left(\boldsymbol{x}\right) + \sum_{\substack{|\boldsymbol{a}| = 1\\ \boldsymbol{a} \neq \boldsymbol{\beta}}}^{\infty} \frac{(-1)^{|\boldsymbol{a}|}}{\boldsymbol{a}!} \varepsilon^{|\boldsymbol{a}|-|\boldsymbol{\beta}|} M_{\boldsymbol{a}} D^{\boldsymbol{a}} f\left(\boldsymbol{x}\right) \tag{10}$$

Finally, to approximate $Q^{\boldsymbol{\beta}}f(\boldsymbol{x})$ with order of accuracy r, the following set of conditions is imposed for the moments M_{a}:

$$M_{\boldsymbol{a}} = \begin{cases} (-1)^{|\boldsymbol{\beta}|}\boldsymbol{\beta}! & \boldsymbol{a} = \boldsymbol{\beta} \\ 0, & \boldsymbol{a} \neq \boldsymbol{\beta},\ 1 \leq |\boldsymbol{a}| \leq |\boldsymbol{\beta}| + r - 1 \end{cases} \tag{11}$$

In addition, if we impose

$$\int |z|^{|\boldsymbol{\beta}|+r} \left|\eta^{\boldsymbol{\beta}}\left(z\right)\right| dz < \infty \tag{12}$$

the mollification error $\epsilon_{\varepsilon}(\boldsymbol{x})$= $D^{\boldsymbol{\beta}}f(\boldsymbol{x})$-$Q^{\boldsymbol{\beta}}f(\boldsymbol{x})$ is bounded [6]. The challenge is to construct a kernel that satisfies the conditions described in Eq. (10). A procedure has been described in [6]. Once the kernel is defined, the operator in Eq. (8) can be discretized using a midpoint quadrature over the nodes as

$$Q_h^{\boldsymbol{\beta}} f(\boldsymbol{x}) = \frac{1}{\varepsilon^{|\boldsymbol{\beta}|}} \sum_{p \in N(\boldsymbol{x})} \left(f\left(\boldsymbol{x}_p\right) \mp f(\boldsymbol{x}) \right) \eta_{\varepsilon}^{\boldsymbol{\beta}} \left(\boldsymbol{x} - \boldsymbol{x}_p\right) V_p \tag{13}$$

where $N(\boldsymbol{x})$ is the number of all nodes in a neighborhood around $\boldsymbol{x}$, which is usually defined by a cutoff radius r_c chosen such that $N(\boldsymbol{x})$ coincides to a certain level of accuracy with the kernel support. V_p is the volume associated with each particle. Given such a discretization, the discretization error $\epsilon_h(\boldsymbol{x}) = Q^{\boldsymbol{\beta}} f(\boldsymbol{x}) - Q_h^{\boldsymbol{\beta}} f(\boldsymbol{x})$ is also bounded [6].

2.2.2 The Discretization Corrected PSE Operators

The discretization corrected PSE (DC PSE) operators were introduced in [4], to reduce the discretization error $\epsilon_h(x)$ in the PSE operator approximation. The derivation of the DC PSE approximation starts from Eq. (13) (with V_p included in the kernel function), with the requirement of finding a kernel function which minimizes the difference between this specific discrete operator and the actual derivative. To achieve this, each term *f(*$\boldsymbol{x}_p$*)* in Eq. (13) is replaced with its Taylor expansion about $\boldsymbol{x}$, leading to the following expression for the derivative approximation:

$$Q_h^{\boldsymbol{\beta}} f(\boldsymbol{x}) = \frac{(-1)^{|\boldsymbol{\beta}|}}{\boldsymbol{\beta}!} Z_h^{\boldsymbol{\beta}} D^{\boldsymbol{\beta}} f(\boldsymbol{x}) + \sum_{\substack{|\boldsymbol{a}| = 1 \\ \boldsymbol{a} \neq \boldsymbol{\beta}}}^{\infty} \frac{(-1)^{|\boldsymbol{a}|}}{\boldsymbol{a}!} \varepsilon^{|\boldsymbol{a}| - |\boldsymbol{\beta}|} Z_h^{\boldsymbol{a}} D^{\boldsymbol{a}} f(\boldsymbol{x}) + r_0 \tag{14}$$

with

$$r_0 = \begin{cases} 0, & |\boldsymbol{\beta}| \ even \\ 2e^{-|\boldsymbol{\beta}|} Z_h^0 f(\boldsymbol{x}) & |\boldsymbol{\beta}| \ odd \end{cases} \tag{15}$$

and the discrete moments defined as

$$Z_h^{\boldsymbol{a}} = \frac{1}{\varepsilon^d} \sum_{p \in N(\boldsymbol{x})} \left(\frac{\boldsymbol{x} - \boldsymbol{x}_p}{\varepsilon} \right)^{\boldsymbol{a}} \eta^{\boldsymbol{\beta}} \left(\frac{\boldsymbol{x} - \boldsymbol{x}_p}{\varepsilon} \right) \tag{16}$$

Therefore, the set of moment conditions become

$$Z_h^a = \begin{cases} (-1)^{|\boldsymbol{\beta}|} \boldsymbol{\beta}! & \boldsymbol{a} = \boldsymbol{\beta} \\ 0 & \boldsymbol{a} \neq \boldsymbol{\beta} \quad a_{min} \leq |\boldsymbol{a}| \leq |\boldsymbol{\beta}| + r - 1 \\ < \infty & \text{otherwise} \end{cases} \tag{17}$$

for all $|\boldsymbol{\beta}| \neq 0$, where a_{min} is one when $|\boldsymbol{\beta}|$ is odd and 0 when $|\boldsymbol{\beta}|$ is even. The kernel $\eta^{\boldsymbol{\beta}}$ is chosen as:

$$\eta^{\boldsymbol{\beta}}(\boldsymbol{x}, z) = \left(\sum_{|\boldsymbol{\gamma}|=a_{min}}^{|\boldsymbol{\beta}|+r-1} a_{\boldsymbol{\gamma}}(\boldsymbol{x})\, z^{\boldsymbol{\gamma}} \right) e^{-|z|^2} = P(\boldsymbol{x}, z)\, W(z), z = \frac{\boldsymbol{x} - \boldsymbol{x}_p}{\varepsilon} \tag{18}$$

The kernel function consists of a polynomial correction function $P(\boldsymbol{x}, \boldsymbol{z})$ and the weight function $W(\boldsymbol{z})$. Different choices for the weight function applied can be found in [6]. The unknown coefficients $a_{\boldsymbol{\gamma}}(\boldsymbol{x})$ are obtained by requesting the kernel given by Eq. (18) to satisfy the conditions in Eq. (8). Given our choice of kernel function, the DC PSE derivative approximation becomes

$$Q_h^{\boldsymbol{\beta}} f(\boldsymbol{x}_p) = \frac{1}{\varepsilon(\boldsymbol{x}_p)^{\boldsymbol{\beta}}} \sum_{\boldsymbol{x}_q \in \mathcal{N}(\boldsymbol{x}_p)} \left(f(\boldsymbol{x}_q) \mp f(\boldsymbol{x}_p) \right) \boldsymbol{p}\left(\frac{\boldsymbol{x} - \boldsymbol{x}_p}{\varepsilon(\boldsymbol{x}_p)} \right) \boldsymbol{a}^T(\boldsymbol{x}_p)\, e^{-\left(\frac{|\boldsymbol{x}_p - \boldsymbol{x}_q|}{\varepsilon(\boldsymbol{x}_p)} \right)^2} \tag{19}$$

where $\boldsymbol{p}(\boldsymbol{x}) = [p_1(\boldsymbol{x}), p_2(\boldsymbol{x}), \ldots, p_m(\boldsymbol{x})]$, with m being the number of monomial used ($m = 6$ and 10 for second order monomials in two and three dimensions, respectively) and, $\boldsymbol{a}(\boldsymbol{x})$ are the vectors of terms in the monomial basis and their coefficients, respectively.

Runge–Kutta (RK4) Explicit Solver

Given the vorticity $\omega^{(n)}$ and stream function values $\psi^{(n)}$ on the nodes, the updated values $\{\omega^{(n+1)}, \psi^{(n+1)}\}$ can be computed by:

$$\frac{\omega^{(1)} - \omega^{(n)}}{\frac{1}{2}\Delta t} + \frac{\partial \psi^{(n)}}{\partial y}\frac{\partial \omega^{(n)}}{\partial x} - \frac{\partial \psi^{(n)}}{\partial x}\frac{\partial \omega^{(n)}}{\partial y} = \frac{1}{\mathrm{Re}}\nabla^2 \omega^{(n)}, \nabla^2 \psi^{(1)} = \omega^{(1)} \tag{20}$$

$$\frac{\omega^{(2)} - \omega^{(n)}}{\frac{1}{2}\Delta t} + \frac{\partial \psi^{(1)}}{\partial y}\frac{\partial \omega^{(1)}}{\partial x} - \frac{\partial \psi^{(1)}}{\partial x}\frac{\partial \omega^{(1)}}{\partial y} = \frac{1}{\mathrm{Re}}\nabla^2 \omega^{(1)}, \nabla^2 \psi^{(2)} = \omega^{(2)} \tag{21}$$

$$\frac{\omega^{(3)} - \omega^{(n)}}{\Delta t} + \frac{\partial \psi^{(2)}}{\partial y}\frac{\partial \omega^{(2)}}{\partial x} - \frac{\partial \psi^{(2)}}{\partial x}\frac{\partial \omega^{(2)}}{\partial y} = \frac{1}{\mathrm{Re}}\nabla^2 \omega^{(2)}, \nabla^2 \psi^{(3)} = \omega^{(3)} \tag{22}$$

$$k_4 = -\Delta t \left(\frac{\partial \psi^{(3)}}{\partial y}\frac{\partial \omega^{(3)}}{\partial x} - \frac{\partial \psi^{(3)}}{\partial x}\frac{\partial \omega^{(3)}}{\partial y} - \frac{1}{\mathrm{Re}}\nabla^2 \omega^{(3)} \right) \tag{23}$$

$$\omega^{(n+1)} = \frac{1}{3}\left(-\omega^{(n)} + \omega^{(1)} + 2\omega^{(2)} + \omega^{(3)} \right) + \frac{1}{6}k_4, \nabla^2 \psi^{(n+1)} = \omega^{(n+1)} \tag{24}$$

In each stage, updated values for the velocity are computed through Eqs. (3a) and (3b). Meshless methods are recognized as one of the most accurate and efficient numerical methods to compute derivatives on an irregularly distributed set (cloud) of nodes. For the stream function–vorticity N-S equations, given the velocity field values computed previously by the updated stream function values $\psi^{(n+1)}$, we can compute the updated vorticity values $\omega^{(n+1)}$ for the entire spatial domain (including boundaries) by using the strong form meshless operators for first order spatial derivative as

$$\omega^{(n+1)} = \frac{\partial v^{(n+1)}}{\partial x} - \frac{\partial u^{(n+1)}}{\partial y} \tag{25}$$

3 Results

We obtain the flow domain from brain digital subtraction angiography (DSA) images (University Hospital Rion, Patras, Greece) (Fig. 1). The resolution of the images is 128 × 128. For the test case examined, the flow domain downstream forms a dilation (aneurysm) and bifurcates.

The boundaries of the flow domain are obtained by thresholding segmentation and an edge detection method. In the context of meshless methods, the spatial domain is represented (not discretized like in mesh-based methods) by an irregular point cloud or a Cartesian embedded grid (Fig. 2). In both cases, generating the point cloud is a straightforward procedure. In the former, irregular nodes can be generated by using a standard 2D triangular mesh generator (we use only the nodes and not their connectivity). 2D mesh generators are fully automated and can be used to discretize complex geometries. Additionally, there is no need to generate 'good quality mesh' and consequently, 'good quality point clouds'. In the latter, uniform Cartesian grid nodes are generated and use for the simulation only those located inside the flow domain.

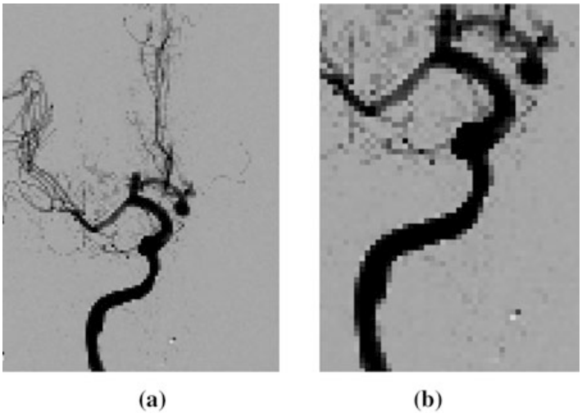

Fig. 1 (**a**) DSA image and (**b**) region of interest (ROI)

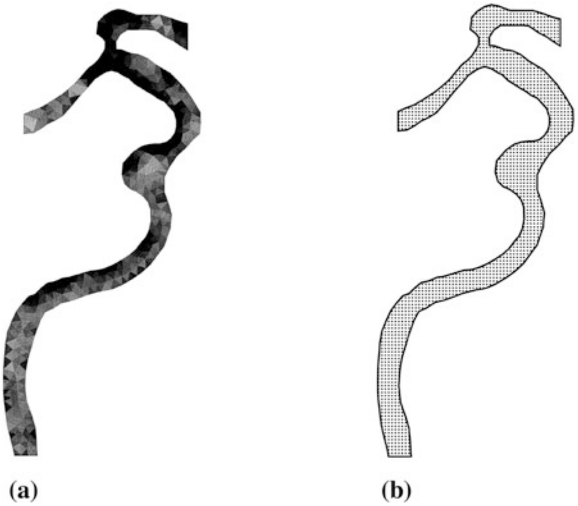

Fig. 2 Representation of the flow domain with (**a**) irregular nodal distribution and (**b**) Cartesian embedded grid

For the test case examined in the present study, we used in total 396,945 nodes (to ensure a grid independent numerical solution) to represent the flow domain. We used the 2D triangular mesh generator (MESH2D-Delaunay-based unstructured mesh-generation), and the time needed to create the irregular nodal distribution was not more than 5 s (computations were conducted in a Mac Pro laptop with 16 GB RAM and Intel i7 quad core 2.7 GHz processor). For the uniform Cartesian grid, we used the build-in MATLAB functions to create the Cartesian grid and define the nodes located in the flow domain. Again the computation took no more than 5 s.

For the meshless point collocation method, spatial derivatives (up to second order) are computed for the numerical solution of the governing equations. We use an in-house C++ code and for the number of nodes used, derivatives computed in 3.2 s. The dynamic viscosity is set to $\mu = 0.00032$ kg/m·s and the density to $\rho = 1050\,\mathrm{kg/m^3}$.

Flow simulation strongly depends on the boundary conditions (especially inflow and outflow boundary conditions) and on the flow domain geometry. We examine the robustness of the proposed scheme on the inflow boundary variability (different Reynolds number). We highlight that the method performs efficiently and is not altered by the variability of the inflow boundary conditions.

3.1 Dependence on Inflow Boundary Conditions

Flow characteristics play an important role in vascular disease, since they are heavily dependent on hemodynamic factors. As pointed-out earlier, measurement of in vivo hemodynamics can be difficult and in the majority of the cases invasive [7]. Computational fluid dynamics (CFD) is an approach able to quantify hemodynamics with high spatial and temporal resolution [8]. Due to the complex characteristics of the cardiovascular system, quantification of the intricate flow, velocity and pressure fields in vascular models can only be achieved by performing patient-specific simulations.

Accurate boundary conditions for CFD studies rely on a number of assumptions, such as the blood rheology, the computational grid size and adaptivity. Typically, in the majority of the studies idealized velocity profiles (such as a parabolic, plug or Womersley) for the inflow boundary conditions have been used, by measuring only a few in vivo velocity parameters such as peak velocity, average velocity or flow rate [9]. The need for accurate inflow boundary conditions is particularly important for realistic and clinically useful flow results. Therefore, it might be expected that use of idealized velocity profiles, which do not take into account patient-specific flow conditions and geometry alterations, would be inappropriate for patient-specific hemodynamics study, and yield inaccurate CFD results.

In the present study, we demonstrate the efficiency of the proposed scheme to work with different inlet boundary conditions. We therefore consider parabolic and plug velocity profiles and examined the efficiency of the scheme and the alterations in the velocity magnitude may result in different flow regimes downstream. For the plug velocity profile, we consider two velocity magnitudes, namely $U_m = 0.0015$ and 0.025 m/s, while in the case of parabolic and parabolic transient we apply $U_{\text{inlet}} = 4U_m x(H - x/H^2)$ and $U_{\text{inlet}} = 4U_m x(H - x/H^2)\sin(\pi t/3)$, respectively, with H being the inlet length. Reynolds number $Re = \rho U_m H/\mu$, with D being a characteristic length. At both outlets, the flow is fully developed ($du/dx = 0$) and, for the rest of the boundaries we applied no-slip conditions. The total time for the simulation was set to $T_{\text{tot}} = 3$ s and the time step used was $dt = 10^{-4}$ s (the critical time step computed was $dt_{\text{critical}} = 10^{-3}$ s). Figure 2 shows the nodal distributions, irregular and Cartesian embedded.

Figure 3 shows the iso-contours for the stream function at $t = 1$ s. We observe that when velocity inlet velocity increases, vortices are formed downstream, in the region of the aneurysm and close to the bifurcation.

4 Discussion

We have described a meshless point collocation algorithm for solving the non-stationary, incompressible, laminar Navier–Stokes equations over complex geometries of the vascular system.

We tested the proposed algorithm using a flow derived from digital subtraction angiography (DSA) images, and examined the dependency of the flow field on the boundary conditions. The results indicate that the method is efficient (computational time of around 5 s using a laptop for a model with close to 400,000 nodes) and facilitates straightforward treatment of different boundary conditions. The method is efficient for uniform Cartesian (embedded) grids and for irregular point clouds (see Fig. 3).

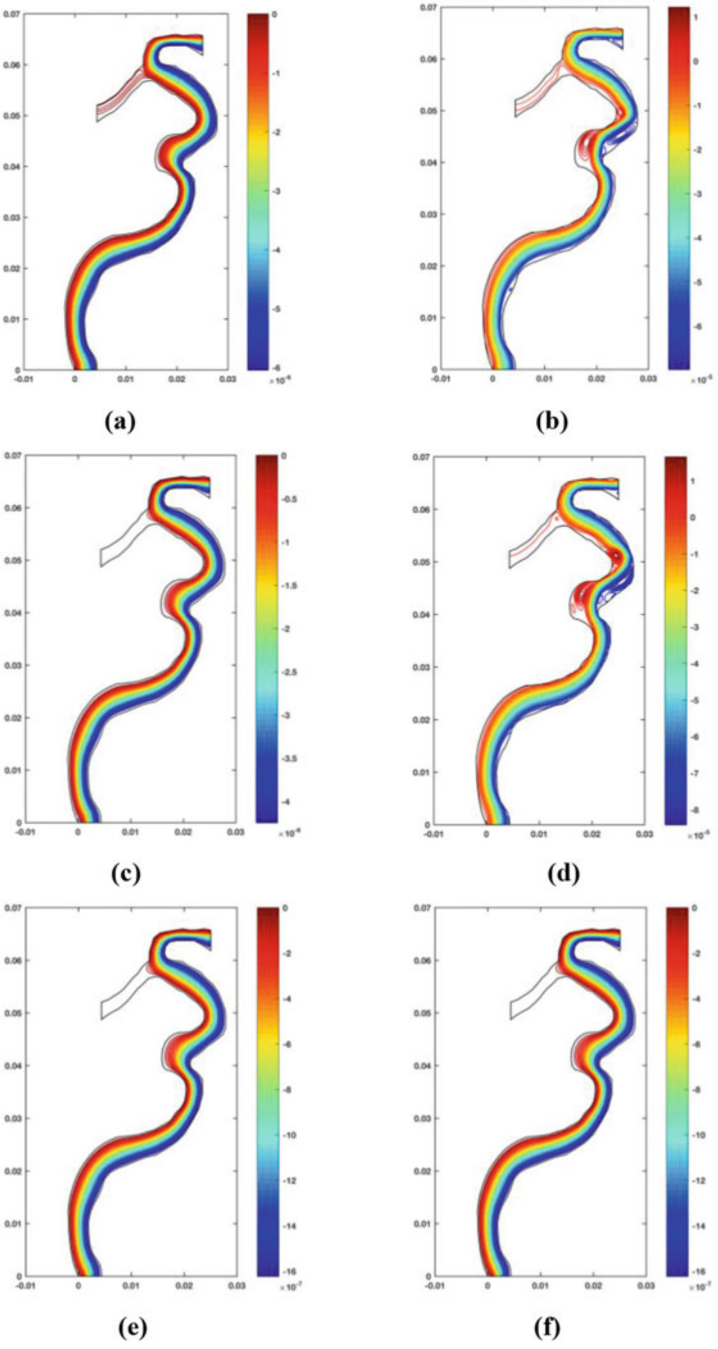

(a) (b) (c) (d) (e) (f)

Fig. 3 Predicted streamlines for $U_m = 0.0015$ (left) and $U_m = 0.025$ (right) (**a**, **b**) plug profile, (**c**, **d**) parabolic profile and (**e**, **f**) parabolic unsteady profile

Acknowledgements This research was supported by the Australian Government through the Australian Research Council's *Discovery Projects* funding scheme (project DP160100714).

References

1. Zhang JY, Joldes GR, Wittek A, Miller K (2013) Patient-specific computational biomechanics of the brain without segmentation and meshing. Int J Numer Methods Biomed Eng 29(2):293–308
2. Bourantas GC, Cheesman BL, Ramaswamy R, Sbalzarini IF (2016) Using DC PSE operator discretization in Eulerian meshless collocation methods improves their robustness in complex geometries. Comput Fluids 136:285–300
3. Fletcher CAJ (1988) Computational techniques for fluid dynamics, vol I and II. Springer series in computational physics. Springer, Berlin
4. Schrader B, Reboux S, Sbalzarini IF (2010) Discretization correction of general integral PSE operators for particle methods. J Comput Phys 229:4159–4182
5. Degond P, Mas-Gallic S (1989) The weighted particle method for convection-diffusion equations. Part 2: the anisotropic case. Math Comput 53(188):509–525
6. Eldredge JD, Leonard A, Colonius T (2002) A general deterministic treatment of derivatives in particle methods. J Comput Phys 180(2):686–709
7. Xiong G, Figueroa CA, Xiao N, Taylor CA (2011) Simulation of blood flow in deformable vessels using subject-specific geometry and spatially varying wall properties. Int J Numer Methods Biomed Eng 27(7):1000–1016
8. Milner JS, Moore JA, Rutt BK, Steinman DA (1998) Hemodynamics of human carotid artery bifurcations: computational studies with models reconstructed from magnetic resonance imaging of normal subjects. J Vasc Surg 28(1):143–156
9. Campbell IC, Ries J, Dhawan SS, Quyyumi AA, Taylor WR, Oshinski JN (2012) Effect of inlet velocity profiles on patient-specific computational fluid dynamics simulations of the carotid bifurcation. ASME J Biomech Eng 134(5):051001

Muscle Excitation Estimation in Biomechanical Simulation Using NAF Reinforcement Learning

Amir H. Abdi, Pramit Saha, Venkata Praneeth Srungarapu, and Sidney Fels

Abstract Motor control is a set of time-varying muscle excitations which generate desired motions for a biomechanical system. Muscle excitations cannot be directly measured from live subjects. An alternative approach is to estimate muscle activations using inverse motion-driven simulation. In this article, we propose a deep reinforcement learning method to estimate the muscle excitations in simulated biomechanical systems. Here, we introduce a custom-made reward function which incentivizes faster point-to-point tracking of target motion. Moreover, we deploy two new techniques, namely episode-based hard update and dual buffer experience replay, to avoid feedback training loops. The proposed method is tested in four simulated 2D and 3D environments with 6–24 axial muscles. The results show that the models were able to learn muscle excitations for given motions after nearly 100,000 simulated steps. Moreover, the root mean square error in point-to-point reaching of the target across experiments was less than 1% of the length of the domain of motion. Our reinforcement learning method is far from the conventional dynamic approaches as the muscle control is derived functionally by a set of distributed neurons. This can open paths for neural activity interpretation of this phenomenon.

Keywords Deep reinforcement learning · Muscle excitation · Inverse motion-driven simulation · Normalized advantage function · Deep Q-network

1 Introduction

Biomechanical modeling provides a powerful tool for analyzing structure and function of human anatomy, thereby establishing a scientific basis for treatment planning. Modeling is particularly indispensable in cases when mechanical variables

---

A. H. Abdi (✉) · P. Saha · V. P. Srungarapu · S. Fels
Electrical and Computer Engineering Department, University of British Columbia, Vancouver, Canada
e-mail: amirabdi@ece.ubc.ca

M. P. Nash et al. (eds.), *Computational Biomechanics for Medicine*,
https://doi.org/10.1007/978-3-030-15923-8_11

are hard or impossible to measure with the available technologies [10]. One of the unknown variables in understanding a musculoskeletal system is the muscle excitation trajectory. Muscle excitations reflect underlying neural control processes; they form a connection between the causal neural activities and the resultant observed motion. Researchers have proposed various techniques, including forward-dynamics tracking simulation, inverse dynamics-based static optimization, and optimal control strategies, to predict muscle excitations and forces [4]. However, the muscle redundancy problem makes the task far more challenging. To address this problem, many approaches have been investigated including minimization of motion tracking errors, squared muscle forces, and combined muscle stress [4]. Unfortunately, the performance errors, high computational costs, and their sensitivity to optimal criteria and extensive regularizations have directed many researchers to seek alternative strategies [7, 12].

Deep reinforcement learning (RL) is a popular area of machine learning that combines RL with deep neural networks to achieve higher levels of performance on decision-making problems including games, robotics, and health care [9]. In these approaches, an agent interacts with the environment and makes intelligent decisions (actions) based on value functions $V(s)$, action-value functions $Q(s, a)$, policies $\pi(s, a)$, or learned dynamics models.

Recent studies in deep RL have pushed the boundaries from discrete to continuous action spaces [5], extending its possibilities for complex biomechanical control applications. Although most researchers encode the locomotion in terms of joint angles for robotics applications, some progress has been made in the muscle-driven RL-based motion synthesis. Izawa et al. introduced an actor-critic RL algorithm with subsequent prioritization of control action space to estimate the motor command of a biological arm model [6]. Broad et al. explored a receding horizon differential dynamic programming algorithm for arm dynamics optimization through muscle control policy to achieve desired trajectories in OpenSim [2]. These approaches require an a priori information such as the relative action preferences or ranking systems which are rarely known in biomechanical systems. Quite recently, in the non-RL domain, deep learning approaches are also explored to predict muscle excitations for point reaching movements, which rely on training data provided by inverse dynamics methods [1, 7].

This work is aimed at developing an improved understanding of the effective coordination of muscle excitations to generate movements in musculoskeletal systems. It borrows ideas from and extends on a continuous variant of the deep Q-network (DQN) algorithm known as normalized advantage function (NAF-DQN). This research introduces three contributions: a *customized reward function*, the *episode-based hard update* of the target model in double Q-learning, and the *dual buffer experience replay*. It also takes advantage of a *reduced-slope logistic function* to estimate muscle excitations. The proposed approach is agnostic to the dynamics of the environment and is tested for systems with up to 24 degrees of freedom. Due to its independence from training data, the trained models work as expected in unseen scenarios.

2 Background

The goal of reinforcement learning is to find a policy $\pi(a|s)$ which maximizes the expected sum of returns based on a reward function $r(s, a)$, where a is the action taken in state s. During training, at each time step t, the agent takes the action a_t and arrives at state s_{t+1} and is rewarded with R_t, formulated as

$$R_t = \sum_{i=t} \gamma^{i-t} r(s_t, a_t), \tag{1}$$

where $\gamma < 1$ is a discount factor that reduces the value of future rewards.

In physical and biomechanical environments, system dynamics are not known and a model of the environment, $p(s_{t+1}|s_t, a_t)$, cannot be directly learned. Therefore, a less direct model-free off-policy learning approach is more beneficial. Q-learning is an off-policy algorithm that learns a greedy deterministic policy based on the action-value function, $Q^{\pi}(s, a)$, referred to as the Q-function. Q-function determines how valuable the (s, a) tuple is under the policy π. Q-learning is originally designed for discrete action spaces and chooses the best action (μ) as

$$\mu(s_t) = \underset{a}{\operatorname{argmax}}\, Q(s_t, a_t). \tag{2}$$

Deep Q-network (DQN) is an extension of Q-learning that uses a parameterized value-action function, θ^Q, determined by a deep neural network. In DQN, the objective is to minimize the Bellman error function

$$\begin{aligned} L(\theta^Q) &= \mathbb{E}[(Q(s_t, a_t|\theta^Q) - y_t)^2] \\ y_t &= r(s_t, a_t) + \gamma Q(s_{t+1}, \mu(s_{t+1})), \end{aligned} \tag{3}$$

where y_t is the observed discounted reward provided by the environment [13].

To enable DQN in continuous action spaces, normalized advantage function (NAF) was introduced by Gu et al. [5], where the Q-function is represented as the sum of two parameterized functions, namely the value function, V, and the advantage function, A, as

$$Q(s, a|\theta^Q) = V(s|\theta^V) + A(s, a). \tag{4}$$

Value function describes a state and is simply the expected total future rewards of a state. The Q-function, on the other hand, describes an action in a state and explains how good it is to choose action a at state s. Therefore, the advantage function, defined as $Q(.) - V(.)$, is a notion of the relative importance of each action. NAF is defined as follows:

$$\begin{aligned} A(s, a) &= -\frac{1}{2}(a - \mu(s|\theta^{\mu}))^T P(s|\theta^P)(a - \mu(s|\theta^{\mu})) \\ P(s|\theta^P) &= L(s|\theta^P)L(s|\theta^P)^T \end{aligned}, \tag{5}$$

where μ is a parametric function determined by the neural network θ^{μ}; and L is a lower-triangular matrix filled by the neural network θ^P with the diagonal terms squared; consequently, P is a positive-definite square matrix [5]. While there are numerous ways to define an advantage function, the restricted parametric formulation of NAF ensures that the action that maximizes Q^{π} is always given by $\mu(s|\theta^{\mu})$.

3 Materials and Method

3.1 Model Architecture

The deep dueling architecture used in this study is depicted in Fig. 1. The θ^V and $\theta^{V'}$ neural networks receive the system state as input and estimate the value functions $V(s)$ and $V'(s)$. This design follows the double Q-learning approach [14] to separate the action selector and evaluator operators. During training, $\theta^{V'}$ receives the next state (s_{t+1}) to calculate the observed discounted total reward (y_t), while θ^V receives the current state (s_t) to predict the reward.

Here, we propose the *episode-based hard update* technique, where the weights of the $\theta^{V'}$ network are only updated at the end of each episode by the weights of θ^V. This technique helps separate the exploration and training processes and mitigates the risk of getting stuck in a positive feedback loop.

The θ^P network receives the current state and generates $(|a|^2 + |a|)/2$ values to fill the lower-triangular matrix of L, which, in turn, is squared to create matrix P (Eq. 5). The θ^{μ} network receives the current state, and estimates the excitations of the $|a|$ muscles as a value between 0 and 1. We deploy a *reduced-slope logistic function*, $f(x) = 1/(1 + e^{-mx})$, in the final layer of the action selector θ^{μ}, where $0 < m < 1$ defines the slope. This reduction in steepness mitigates the variance of muscle activations and results in a smoother muscle control.

3.2 Methods

Training is composed of disjoint episodes. Each episode starts with a target point, T, randomly positioned in the motion space of the point mass, P. Motion space (domain) is defined as the entire area (volume) that the point mass can traverse in the simulated environment with muscle activations. An episode ends either by the agent reaching the terminal state, i.e., the point mass reaching the target or going over a maximum number of steps per episode.

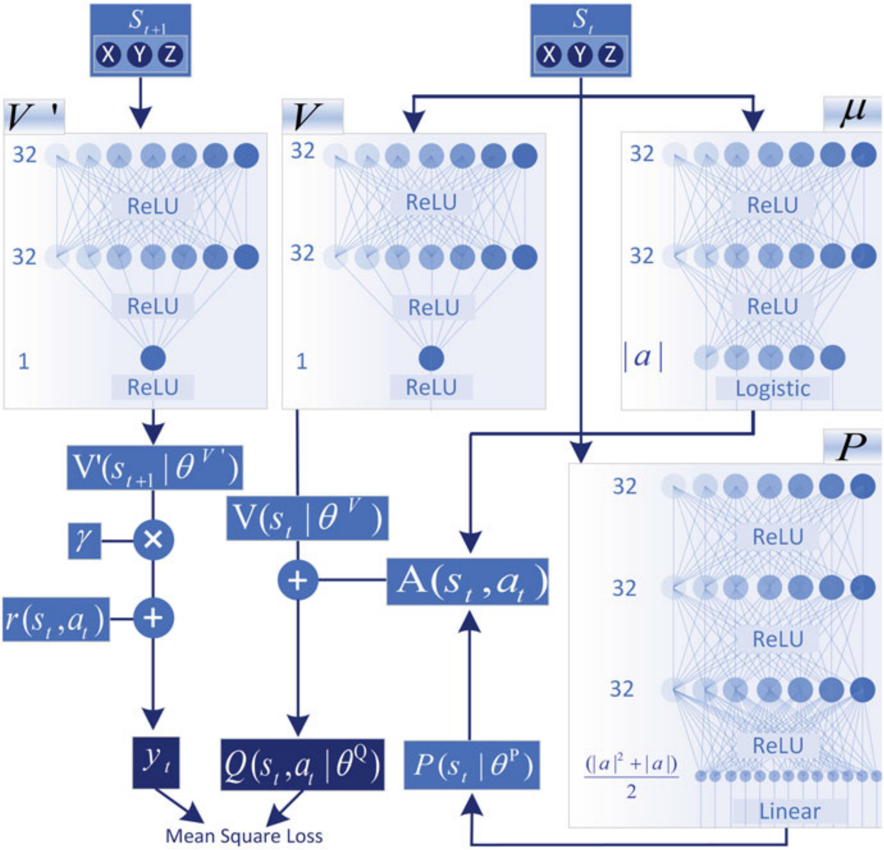

Fig. 1 The normalized advantage function algorithm and architectures of the three neural networks, namely θ^μ, θ^V, and θ^L (Eqs. 3–5). The arrows demonstrate the data flow in the feedforward path

The size of the action space, $|a|$, is equal to the number of muscles. The state space is the spatial position of the target (T_x, T_y, T_z), where T_y is constantly zero in the 2D simulations. The position of the point mass (P) is excluded from the state formulation to imitate a real-world biomechanical system where the exact position of each joint is not known.

Reward Function The goal of the agent is to set the muscle excitations so that P reaches T. To incentivize this, two factors were encoded in the reward function: distance and time,

$$r(s_t, a_t) = \begin{cases} -1 & |P_{t+1} - T| \geq |P_t - T| \\ 1/t & |P_{t+1} - T| < |P_t - T| \\ \omega & |P_{t+1} - T| \leq d_{thres} \end{cases}, \tag{6}$$

where $\omega > 0$ is a constant value rewarded in a successful terminal state, and $|P - T|$ is the Euclidean distance between P and T. Terminal state is defined as a distance of less than d_{thres} between P and T. The agent is penalized if $|P - T|$ is not lessened as a result of the action. Moreover, the rewards for correct decisions are reduced by a time factor to incentivize fast direct reach of the target, as opposed to curved trajectories.

Action Exploration To enable action exploration in the continuous action domain, outputs of the θ^{μ} network, i.e., the muscle excitations, were augmented with a zero-mean stationary Gaussian–Markov stochastic process, known as the Ornstein Uhlenbeck. The stochastic process was initialized with a variance of 0.35, which was annealed as a function of t down to 0.05.

Dual Buffer Experience Replay We borrow the idea of experience replay from the works of Mnih et al. for higher data efficiency and training on non-consecutive samples [9]. In this technique, a replay buffer stores seen samples as (s_t, a_t, r_t, s_{t+1}) tuples. Samples are then randomly selected for training from the buffer. In order to avoid feedback loops during an episode of training, we propose the *dual buffer experience replay* strategy, where the *episode buffer* stores samples of the current episode, while the training samples are chosen from the *back buffer*. At the end of each episode, contents of the *episode buffer* are copied into the *back buffer*. This strategy is mostly important in the beginning of the training when the replay buffer is fairly sparse.

Training Hyper-Parameters If the success threshold radius, d_{thres}, is set too high, the agent is given the success reward too early and effortless, thus will not learn the exact activation patterns. On the contrary, a small d_{thres} value makes it impossible for the point mass to reach the success state which delays training. Based on the above intuition, d_{thres} was set so that less than 1% of the motion domain of the point mass is defined as the success state. The learning rate (α) and the reward discount factor (γ) were set to 0.01 and 0.99, respectively. Each episode of training was constrained to 200 steps at the end of which the episode would restart and the state would reset to a new random position.

4 Experiments and Results

An open-source biomechanical simulator, ArtiSynth, was used to design the simulation environments and run the experiments [8]. The keras-rl library with the TensorFlow backend was used as the basis for the implementations of the methods [3, 11]. A network interface was used to send the target positions from the simulated mechanical environment in ArtiSynth to the deep learning model and receive the new muscle activations from the model. Our implementation, consisting of the ArtiSynth model in Java and the deep RL in Python, has been made available at github.com/amir-abdi/artisynth_rl. The forked keras-rl

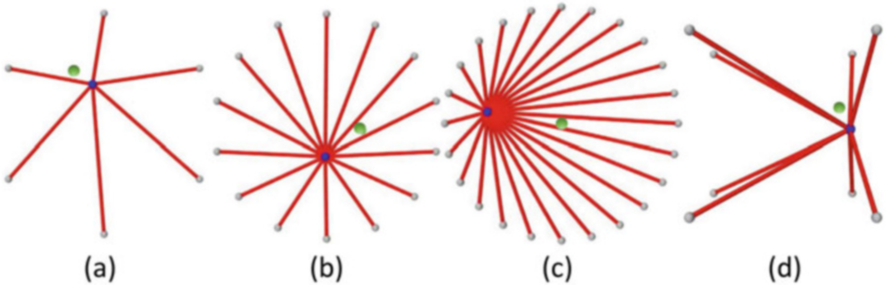

Fig. 2 The four simulation environments: (**a**) 6-muscle 2D, (**b**) 14-muscle 2D, (**c**) 24-muscle 2D, (**d**) 8-muscle 3D. Notice the green and blue particles which visualize the position of the target (T) and the point mass (P)

repository with added functionalities proposed in this paper can be accessed from github.com/amir-abdi/keras-rl.

Four biomechanical environments were designed to test the feasibility and accuracy of the proposed method, including 2D environments with 6, 14, and 24 muscles, and a 3D environment with 8 muscles. Muscles were set to have a maximum active isometric force of 1 N, optimal length of 1 cm, and maximum passive force of 0.1 N, with 50% flexibility for lengthening and shortening of fibers. The damping coefficient was set to 0.1. The hyper-parameters of learning were not altered in between experiments for the results to be comparable.

In 2D environments, one end of each muscle was attached to the point mass, while the other stationary end was positioned on the circumference of a circle of radius 10 cm, as shown in Fig. 2. In the 3D environment, the stationary ends of muscles were positioned at the eight corners of a cuboid of length 20 cm. When the muscle excitations are zero, implying that the axial muscle fibers are at rest, the point mass will move to the very center of the circle. As the muscles get activated, the point mass moves towards the direction of the net force. No other external force was applied to the point mass.

4.1 Results

Figure 3 demonstrates the weighted exponential smoothed curves for the total reward value per episode and the distance between the point mass, P, and the target, T, at the end of each episode as a function of the number of steps. The agents were tested with 500 episodes of random point-to-point reaching tasks, and the Euclidean distance between the final position of the point mass and the target was evaluated. The root mean squared error (RMSE) of the trained agents were 1.8, 1.5, 1.7, and 2.4 mm for the 6-muscle 2D, 14-muscle 2D, 24 muscle 2D, and 8-

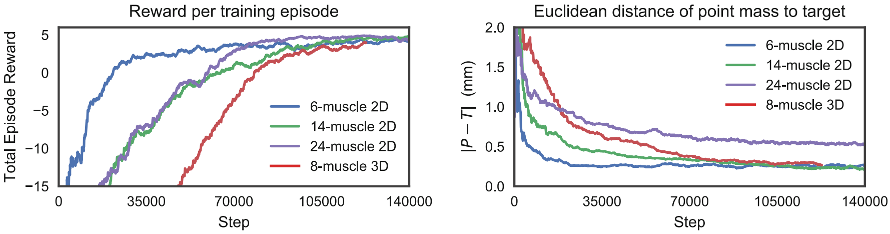

Fig. 3 Training of the RL agent in the four environments depicted in Fig. 2

muscle 3D environments, respectively. The average RMSE across all environments was 1.8 mm.

The learned models were also tested in unseen scenarios where the target point was moved out of the motion domain of the point mass. The surprising result was that the point mass followed the target, to the extent allowed by the model constraints, to minimize the distance between the two.

5 Discussion and Conclusion

In this article, a general reinforcement learning method was introduced to estimate muscle excitations for a given trajectory in a muscle-driven biomechanical simulation. The results assert that the approach is applicable to various degrees of freedom and muscle arrangements. To make the method environment invariant, the agent was kept uninformed of the position of its associated point mass. Moreover, the agent is unaware of the distribution of the muscles, their arrangement, their mechanical properties, and their states. Therefore, it only receives the location of the target point and the rewards in response to its actions.

Deep reinforcement learning models are quite sensitive to hyper-parameters and smaller neural networks have a higher chance of convergence. In our experiments, neural networks with more than two hidden layers for θ^{μ} and θ^{V} did not converge.

As depicted in Fig. 3, the agent learned to reach the target in all environments irrespective of the number of muscles and their configurations. However, a positive correlation was observed between the training time and the degrees of freedom of the biomechanical system, i.e., the number of muscles. The RMSE values indicate that trained agents managed to reach their target locations with a distance of less than half the designated d_{thres}. In other words, the point mass has reached its target with less than 1% distance with respect to its length of the domain of motion. Interestingly, with no further fine tuning of the parameters, the performance of the method remained intact in higher degrees of freedom.

The results show that there exists a positive correlation between the d_{thres} value and the final RMSE of the trained model. However, setting d_{thres} to smaller values increases the chance of unsuccessful episodes which delays convergence. Therefore, the authors suspect that gradually decaying this value, upon network convergence, can reduce the final RMSE of the model.

The proposed reinforcement learning method does not require any labeled data for training, as opposed to other approaches where known optimal control trajectories were used as training data [1, 7]. This highlights another important finding of the current study that the trained models were functional when tested in unseen scenarios where the target point was moved out of the motion domain of the point mass. Since the model had learned the optimal muscle control independent of any training data, it was able to estimate the correct muscle excitations and move the point mass to minimize its distance to the target.

The proposed reinforcement learning approach is different from the conventional inverse dynamics methods in the sense that the muscle controls are derived parametrically from a set of distributed neurons of the neural network, i.e., θ^{μ}. Such approach opens the path for neural activity interpretation of the muscle control.

References

1. Berniker M, Kording KP (2015) Deep networks for motor control functions. Front Comput Neurosci 9:35
2. Broad A (2011) Generating muscle driven arm movements using reinforcement learning. Master's thesis, Washington University in St. Louis
3. Chollet F et al (2015) Keras. https://github.com/keras-team/keras
4. Erdemir A et al (2007) Model-based estimation of muscle forces exerted during movements. Clin Biomech 22(2):131–154
5. Gu S et al (2016) Continuous deep Q-learning with model-based acceleration. Cogn Process 12(4):319–340
6. Izawa J et al (2004) Biological arm motion through reinforcement learning. Biol Cybern 91(1):10–22
7. Khan N, Stavness I (2017) Prediction of muscle activations for reaching movements using deep neural networks. In: 41st Annual meeting of the American Society of Biomechanics, Boulder
8. Lloyd J et al (2012) ArtiSynth: a fast interactive biomechanical modeling toolkit combining multibody and finite element simulation. In: Payan Y (ed) Soft tissue biomechanical modeling for computer assisted surgery, vol 11, chap. 126. Springer, Berlin, pp 355–394
9. Mnih V et al (2013) Playing Atari with deep reinforcement learning. arXiv preprint arXiv:1312.5602
10. Pileicikiene G et al (2007) A three-dimensional model of the human masticatory system, including the mandible, the dentition and the temporomandibular joints. Stomatologija Balt Dent Maxillofac J 9(1):27–32
11. Plappert M (2016) keras-rl. https://github.com/matthiasplappert/keras-rl
12. Ravera EP et al (2016) Estimation of muscle forces in gait using a simulation of the electromyographic activity and numerical optimization. Comput Methods Biomech Biomed Engin 19(1):1–12
13. Sutton RS et al (1998) Reinforcement learning: an introduction. MIT Press, Cambridge
14. Van Hasselt H et al (2016) Deep reinforcement learning with double q-learning. In: Thirtieth AAAI conference on artificial intelligence, vol 16, pp 2094–2100

Index

M. P. Nash et al. (eds.), *Computational Biomechanics for Medicine*,
https://doi.org/10.1007/978-3-030-15923-8